AFRL-AFOSR-VA-TR-2016-0315

Catalyst and Fuel Interactions to Optimize Endothermic Cooling

Scott Anderson
UNIVERSITY OF UTAH SALT LAKE CITY
201 PRESIDENTS CIR RM 408
SALT LAKE CITY, UT 84112-9023

09/09/2016
Final Report

REPORT DOCUMENTATION PAGE

Form Approved
OMB No. 0704-0188

1. REPORT DATE (DD-MM-YYYY)	2. REPORT TYPE	3. DATES COVERED (From - To)
30-08-2016	Final Technical Report	30-09-2012 to 31-05-2016

4. TITLE AND SUBTITLE
Catalyst and Fuel Interactions to Optimize Endothermic Cooling

5a. CONTRACT NUMBER

5b. GRANT NUMBER
FA9550-12-1-0481

5c. PROGRAM ELEMENT NUMBER

6. AUTHOR(S)
Scott L. Anderson, Anastassia N. Alexandrova, James A. Dumesic, Manos Mavrikakis, Shiv N. Khanna, Randall E. Winans, Richard N. Zare

5d. PROJECT NUMBER

5e. TASK NUMBER

5f. WORK UNIT NUMBER

7. PERFORMING ORGANIZATION NAME(S) AND ADDRESS(ES)
University of Utah, Chemistry Dept., 315 S. 1400 E, Salt Lake City, UT 84112
subcontracts to University of California at Los Angeles, Virginia Commonwealth University, University of Wisconsin, Argonne National Laboratory, and Standford University

8. PERFORMING ORGANIZATION REPORT NUMBER

9. SPONSORING/MONITORING AGENCY NAME(S) AND ADDRESS(ES)
Michael R. Berman, Air Force Office of Scientific Research, AFOSR/RTB
875 N. Randolph St.
Suite 325, Rm 3112
Arlington, VA 22203

10. SPONSOR/MONITOR'S ACRONYM(S)
AFOSR/RTB

11. SPONSOR/MONITOR'S REPORT NUMBER(S)

12. DISTRIBUTION/AVAILABILITY STATEMENT
DISTRIBUTION A: Distribution approved for public release.

13. SUPPLEMENTARY NOTES

14. ABSTRACT
This report summarizes the main findings of an AFOSR Basic Research Initiative project in the area of endothermic fuels catalysis. The focus was on developing improved catalysts to enhance and control endothermic fuel reactions, to enhance cooling capacity for aircraft. In addition there was substantial basic mechanistic work, aimed at understanding processes responsible for catalytic activity for the reactions of interest, and for deactivation and coking of the catalysts. Finally, there was significant methods development in the areas of theory, catalyst synthesis and characterization, and methods for catalytic reaction analysis.

15. SUBJECT TERMS
Endothermic fuels, catalysis, DFT, clusters, X-ray spectroscopy, Surface Science, Dehydrogenation, Boron

16. SECURITY CLASSIFICATION OF:			17. LIMITATION OF ABSTRACT	18. NUMBER OF PAGES	19a. NAME OF RESPONSIBLE PERSON
a. REPORT	b. ABSTRACT	c. THIS PAGE			Scott L. Anderson
UU	UU	UU	UU	62	19b. TELEPHONE NUMBER (Include area code) 801 585 7289

Reset

Standard Form 298 (Rev. 8/98)
Prescribed by ANSI Std. Z39.18
Adobe Professional 7.0

INSTRUCTIONS FOR COMPLETING SF 298

1. REPORT DATE. Full publication date, including day, month, if available. Must cite at least the year and be Year 2000 compliant, e.g. 30-06-1998; xx-06-1998; xx-xx-1998.

2. REPORT TYPE. State the type of report, such as final, technical, interim, memorandum, master's thesis, progress, quarterly, research, special, group study, etc.

3. DATES COVERED. Indicate the time during which the work was performed and the report was written, e.g., Jun 1997 - Jun 1998; 1-10 Jun 1996; May - Nov 1998; Nov 1998.

4. TITLE. Enter title and subtitle with volume number and part number, if applicable. On classified documents, enter the title classification in parentheses.

5a. CONTRACT NUMBER. Enter all contract numbers as they appear in the report, e.g. F33615-86-C-5169.

5b. GRANT NUMBER. Enter all grant numbers as they appear in the report, e.g. AFOSR-82-1234.

5c. PROGRAM ELEMENT NUMBER. Enter all program element numbers as they appear in the report, e.g. 61101A.

5d. PROJECT NUMBER. Enter all project numbers as they appear in the report, e.g. 1F665702D1257; ILIR.

5e. TASK NUMBER. Enter all task numbers as they appear in the report, e.g. 05; RF0330201; T4112.

5f. WORK UNIT NUMBER. Enter all work unit numbers as they appear in the report, e.g. 001; AFAPL30480105.

6. AUTHOR(S). Enter name(s) of person(s) responsible for writing the report, performing the research, or credited with the content of the report. The form of entry is the last name, first name, middle initial, and additional qualifiers separated by commas, e.g. Smith, Richard, J, Jr.

7. PERFORMING ORGANIZATION NAME(S) AND ADDRESS(ES). Self-explanatory.

8. PERFORMING ORGANIZATION REPORT NUMBER. Enter all unique alphanumeric report numbers assigned by the performing organization, e.g. BRL-1234; AFWL-TR-85-4017-Vol-21-PT-2.

9. SPONSORING/MONITORING AGENCY NAME(S) AND ADDRESS(ES). Enter the name and address of the organization(s) financially responsible for and monitoring the work.

10. SPONSOR/MONITOR'S ACRONYM(S). Enter, if available, e.g. BRL, ARDEC, NADC.

11. SPONSOR/MONITOR'S REPORT NUMBER(S). Enter report number as assigned by the sponsoring/ monitoring agency, if available, e.g. BRL-TR-829; -215.

12. DISTRIBUTION/AVAILABILITY STATEMENT. Use agency-mandated availability statements to indicate the public availability or distribution limitations of the report. If additional limitations/ restrictions or special markings are indicated, follow agency authorization procedures, e.g. RD/FRD, PROPIN, ITAR, etc. Include copyright information.

13. SUPPLEMENTARY NOTES. Enter information not included elsewhere such as: prepared in cooperation with; translation of; report supersedes; old edition number, etc.

14. ABSTRACT. A brief (approximately 200 words) factual summary of the most significant information.

15. SUBJECT TERMS. Key words or phrases identifying major concepts in the report.

16. SECURITY CLASSIFICATION. Enter security classification in accordance with security classification regulations, e.g. U, C, S, etc. If this form contains classified information, stamp classification level on the top and bottom of this page.

17. LIMITATION OF ABSTRACT. This block must be completed to assign a distribution limitation to the abstract. Enter UU (Unclassified Unlimited) or SAR (Same as Report). An entry in this block is necessary if the abstract is to be limited.

REPORT DOCUMENTATION PAGE

Form Approved
OMB No. 0704-0188

1. REPORT DATE *(DD-MM-YYYY)*	2. REPORT TYPE	3. DATES COVERED *(From - To)*
30-08-2016	Final Technical Report	30-09-2012 to 31-05-2016

4. TITLE AND SUBTITLE
Catalyst and Fuel Interactions to Optimize Endothermic
Cooling

5a. CONTRACT NUMBER

5b. GRANT NUMBER
FA9550-12-1-0481

5c. PROGRAM ELEMENT NUMBER

6. AUTHOR(S)
Scott L. Anderson, Anastassia N. Alexandrova, James A. Dumesic, Manos Mavrikakis, Shiv N. Khanna, Randall E. Winans, Richard N. Zare

5d. PROJECT NUMBER

5e. TASK NUMBER

5f. WORK UNIT NUMBER

7. PERFORMING ORGANIZATION NAME(S) AND ADDRESS(ES)
University of Utah, Chemistry Dept., 315 S. 1400 E, Salt Lake City, UT 84112
subcontracts to University of California at Los Angeles, Virginia Commonwealth University,
University of Wisconsin, Argonne National Laboratory, and Standford University

8. PERFORMING ORGANIZATION REPORT NUMBER

9. SPONSORING/MONITORING AGENCY NAME(S) AND ADDRESS(ES)
Michael R. Berman, Air Force Office of Scientific Research, AFOSR/RTB
875 N. Randolph St.
Suite 325, Rm 3112
Arlington, VA 22203

10. SPONSOR/MONITOR'S ACRONYM(S)
AFOSR/RTB

11. SPONSOR/MONITOR'S REPORT NUMBER(S)

12. DISTRIBUTION/AVAILABILITY STATEMENT
Unclassified, unrestricted

13. SUPPLEMENTARY NOTES

14. ABSTRACT
This report summarizes the main findings of an AFOSR Basic Research Initiative project in the area of endothermic fuels catalysis. The focus was on developing improved catalysts to enhance and control endothermic fuel reactions, to enhance cooling capacity for aircraft. In addition there was substantial basic mechanistic work, aimed at understanding processes responsible for catalytic activity for the reactions of interest, and for deactivation and coking of the catalysts. Finally, there was significant methods development in the areas of theory, catalyst synthesis and characterization, and methods for catalytic reaction analysis.

15. SUBJECT TERMS
Endothermic fuels, catalysis, DFT, clusters, X-ray spectroscopy, Surface Science, Dehydrogenation, Boron

16. SECURITY CLASSIFICATION OF:			17. LIMITATION OF ABSTRACT	18. NUMBER OF PAGES	19a. NAME OF RESPONSIBLE PERSON
a. REPORT	b. ABSTRACT	c. THIS PAGE			Scott L. Anderson
UU	UU	UU	UU	62	19b. TELEPHONE NUMBER *(Include area code)* 801 585 7289

Standard Form 298 (Rev. 8/98)
Prescribed by ANSI Std. Z39.18
Adobe Professional 7.0

Catalyst and Fuel Interactions to Optimize Endothermic Cooling

The Basic Research Initiative Team:
Scott Anderson (PI)   Department of Chemistry, University of Utah
Anastassia N. Alexandrova   Chemistry and Biochemistry Department, UCLA
James A. Dumesic   Chemical and Bio Engineering Department, Univ. Wisconsin, Madison
Manos Mavrikakis   Chemical and Bio Engineering Department, Univ. Wisconsin, Madison
Shiv N. Khanna   Physics Department, Virginia Commonwealth University
Randall E. Winans   X-ray Science Division APS, Argonne National Lab
Richard N. Zare   Chemistry Department, Stanford University

Partner:
Susanne Opalka, United Technologies Research Center (UTRC)
                (Coking/cooling tests of candidate catalyst)

Overall Team Objectives:
    Our work focused on use of Pt-based catalysts to enhance endothermic fuel cooling. Real high surface area powdered catalysts were developed, modeled theoretically, and then tested, both in laboratory catalytic reactors, and in an endothermic cooling test rig at United Technologies Research Center. In addition, planar, size-selected model catalysts were used to provide additional mechanistic insight and probe novel strategies for stabilizing catalyst particles, and minimizing deactivation by coking. Both experimental and theoretical method development was a significant focus of the work.

Report Structure:
    To allow each PI to report on his or her activities and accomplishments, this report is divided into chapters for each institution. These chapters report both results of the individual PIs, and accomplishments in collaboration with other team members. Anderson (Utah), Alexandrova (UCLA), Khanna (VCU), and Winans (Argonne) have worked on experiments and theory on model catalysts, designed to elucidate fundamental mechanistic issues, and this work is presented first. Dumesic (U Wisconsin), Mavrikakis (U Wisconsin), and Winans have carried out complementary experimental and theoretical work on practical catalysts, presented next. Finally, the work of Zare on new methodology for studying reactions on surfaces at atmospheric pressure is presented.

PI Name: Scott L. Anderson (team PI)
Address: Chemistry Department, University of Utah, Salt Lake City, UT 84112

Statement of objectives: Anderson's group had two main tasks.

One focus was on model catalyst studies to examine mechanisms for dehydrogenation reactions and catalyst deactivation for supported, size-selected Pt_n clusters on different support materials. We also studied the effects of boron doping and alumina atomic layer deposition overcoating of the clusters, on activity and cluster binding sites. This work included *in situ* ultra-high vacuum (UHV) studies at Utah of cluster electronic properties, stability, and catalytic activity. In addition, we prepared numerous samples of Pt_n on silica and alumina, with alumina under- and over-coating, for study *ex situ* by Winans at Argonne using X-ray scattering and spectroscopic methods. The cluster work was in close collaboration with Alexandrova and Khanna for theory support.

The second task was to develop efficient milling-based processes for high rate/low cost preparation of energetic nanoparticles of boron and aluminum for use in propulsion, to characterize the particles, and to provide them to partner labs for testing. The primary focus was on particles for use in hypergolic ionic liquid (IL) rocket propellants, and this work was done in collaboration with a number of Air Force Research Lab PIs, and with Robin Rogers (then at U Alabama). At AFRL/Edwards, the collaboration involved Jerry Boatz doing detailed theory on the binding of ionic liquid and other molecules to boron and aluminum surfaces, Stefan Schneider and Tom Hawkins for synthesis of hypergolic ILs for our experiments, and Steve Chambreau and Ghanshyam Vaghjiani for spectroscopic studies of hypergolic ignition. At AFRL/WPAFB, Chris Bunker and Will Lewis did X-ray diffraction, calorimetry, and thermal characterization of the materials. Robin Rogers (Alabama) did high speed photographic studies of hypergolic ignition. We have also provided samples of particles in ILs to other DoD-funded researchers. For example, Ralf Kaiser (Hawaii) is studying IR and Raman spectroscopy of single levitated IL droplets with suspended boron particles.

Methodology developed:

To enable preparation and characterization of samples for synchrotron studies at Argonne, we constructed a new cluster deposition instrument, shown in Fig. A1, and described in detail elsewhere.[1] It was possible to construct this instrument quickly and cheaply because I was fortunate to receive a donated (from Kodak) ESCA spectrometer (most of the hardware in the foreground of the picture), and we had an old gas-phase cluster instrument that provided most of the parts for the cluster source and mass selecting beamline (hardware in the background, in front of Yang Dai). To complete the instrument we only needed to add a couple new vacuum chambers, and fabricate the internals of the deposition beamline. The result is a sophisticated instrument with capability to deposit mass-selected metal clusters on well characterized substrates in UHV, and to characterize them *in situ* by a combination of X-ray and UV photoelectron spectroscopy

Fig. A1. New Utah deposition instrument, with Tim Gorey and Yang Dai.

(XPS, UPS), low energy ion scattering spectroscopy (ISS), and temperature-programmed desorption and reaction (TPD, TPR). The instrument also has *in situ* capabilities for atomic layer deposition, and for substrate preparation and cleaning. This instrument also includes sophisticated hardware allowing facile sample exchanges. Samples for Argonne were prepared in the instrument, and then shipped to Argonne under either air or N_2.

Experiments on the effects of boron doping were carried out using a second size-selected cluster deposition instrument, described previously,[2-3] also equipped for sample preparation, XPS, UPS, ISS, TPD/TPD. This instrument has somewhat better spectroscopic spatial resolution, and can work over a wider temperature range (130 - >2200 K), but is not optimized for sample exchange.

In situ X-ray experiments were performed using a unique setup developed at Sector 12-ID-C at the Advanced Photon Source at Argonne.[4] The experiments were performed in a home built reaction cell sealed with Kapton windows and mounted on a computer-controlled goniometer. For high pressure and high temperature operation, this cell (described in more detail in the Argonne chapter), can be equipped with diamond windows. The X-ray beam was scattered off the surface of the sample at grazing incidence, near the critical angle (α_c= 0.15°) of the substrate. A 1024×1024 pixel two-dimensional CCD detector designed and built at the APS was used for recording grazing-incidence small angle X-ray scattering (GISAXS) images. Grazing incidence X-ray absorption spectra were collected at the Sector 12-BM-B and 12-ID-C stations at the Advanced Photon Source of the Argonne National Laboratory using fluorescence detectors.

The energetic nanoparticle experiments used a Retsch PM 400 planetary ball mill with 250 ml tungsten carbide jars. Replacement lids equipped with valved ports were fabricated to allow the atmosphere inside the jars to be controlled and monitored.[5] The valves can be connected to a gas/vacuum manifold inside an N_2-filled glove box, so that samples can be handled entirely in inert atmospheres. Analysis of the particles was done using scanning transmission and scanning electron microscopy (STEM and SEM), dynamic light scattering (DLS), mass spectrometry, and thermogravimetric analysis with mass spectral detection (TGA-MS) at the U of Utah. Additional details can be found in the papers listed at the end of this report chapter.

Accomplishments:
Model catalyst Studies:

Thermal sintering and deactivation by coking are two major issues in catalysis for endothermic fuel cooling reactions. We reported (archival publications 1, 7, 10, 11, additional publication 1) several studies of the effects of heating and adsorbate exposure on catalytic activity and cluster stability under UHV conditions, where the degradation mechanism was primarily thermal sintering, which tends to reduce the number of available catalytic sites. For these studies, we studied Pt and Pd clusters deposited on SiO_2, alumina, and TiO_2, using ion scattering and X-ray scattering to probe cluster sintering, X-ray and UV spectroscopies to probe the effects on electronic properties. CO binding and CO oxidation were used to probe the effects of boron doping, alumina overcoating, and coking on binding site densities and activity of the catalysts. Ethylene binding and dehydrogenation was used as a model for alkene chemistry on the clusters.

In the process, we collaborated with Khanna to develop a new theoretical understanding of electron binding energies, needed for interpretation of the X-ray and UV spectroscopic results (archival publications 3 and 6). We provided experimental data for core and valence electron binding energies as a function of cluster size, and the effects of CO and O_2 binding on both core and valence levels. The Khanna group developed a new theoretical approach to understanding final state effects, and also revealed the importance of adsorbate-induced rehybridization of metal valence electrons for both valence and core electron binding energies. In addition, we collaborated with the Alexandrova group to understand the origins of the effects of boronation on Pt cluster catalytic activity and stability (additional publications 15, 16). The work, discussed below, on X-ray scattering and spectroscopy was done in collaboration with Winans at Argonne.

This Model Catalyst section of the report chapter focuses on two aspects of our work which have not yet appeared in press. We showed in archival publication 1 that there are large cluster size effects on X-ray absorption near-edge spectroscopy (XANES) which can mimic the effects of oxidation or reduction of the metal in the clusters. XANES is a method very commonly used to probe the oxidation state of metal-containing nanostructures, such as catalysts, under operating conditions, thus this discovery should have substantial impact well outside the "catalysis for propulsion" area. The work was a collaboration between the Utah and Argonne groups.

Next, the results of an on-going collaboration with Alexandrova are briefly summarized. The focus is on the effects of boron doping on binding sites and activity of small Pt clusters for alkene binding and dehydrogenation. This work will be submitted as additional publications 15 and 16, both of which are in the process of being written.

A. Cluster size effects on XANES:

Fig. A2 shows XANES results for Pt foil, and for three samples prepared by depositing 0.1 monolayer-equivalent of Pt on SiO_2 in the form of different size mass-selected clusters, i.e., Pt_2, Pt_{13}, and Pt_{24}. The spectral region studied is the Pt L3 edge, which corresponds to excitation of an electron from a 2p core level on a Pt atom, to empty states of the sample, just above the Fermi level (E_F). The relevant features are the energy of the absorption edge (rise in absorption starting around 11560 eV), and the energy and intensity of the "white line" feature, which is the peak that appears just above the absorption edge. The problem for interpretation of XANES for complex materials like catalysts, is that to predict how the spectrum should change with metal oxidation state, particle size, or catalyst support, it is necessary to know the core and valence electronic structure of the material in some detail, and also how the electronic energy levels relax in response to the core hole created in the X-ray absorption process. This information is typically unavailable, and extremely challenging to calculate quantum mechanically for complex materials such as typical catalysts.

Therefore, in the vast majority of XANES studies, spectra are interpreted by comparison to reference materials, such as the bulk metal or metal oxide or salt compounds. That is a perfectly reasonable approach for materials with large bulk-like particles. For materials with particle sizes in the few nanometer range or smaller, however, there are strong size effects on electronic structure that must be considered in XANES interpretation. Nonetheless it is common to interpret XANES by reference to bulk standards, even for materials with sub-nanometer particles, where there is no reason to expect this approach to be valid. The problem is that there are no standard samples for comparison, where both the size and oxidation state of the particles are known. This is the problem we have attacked, by preparing and characterizing in

Fig. A2. XANES for Pt_n/SiO_2 (n = 2, 13, 24) samples compared to that for Pt foil
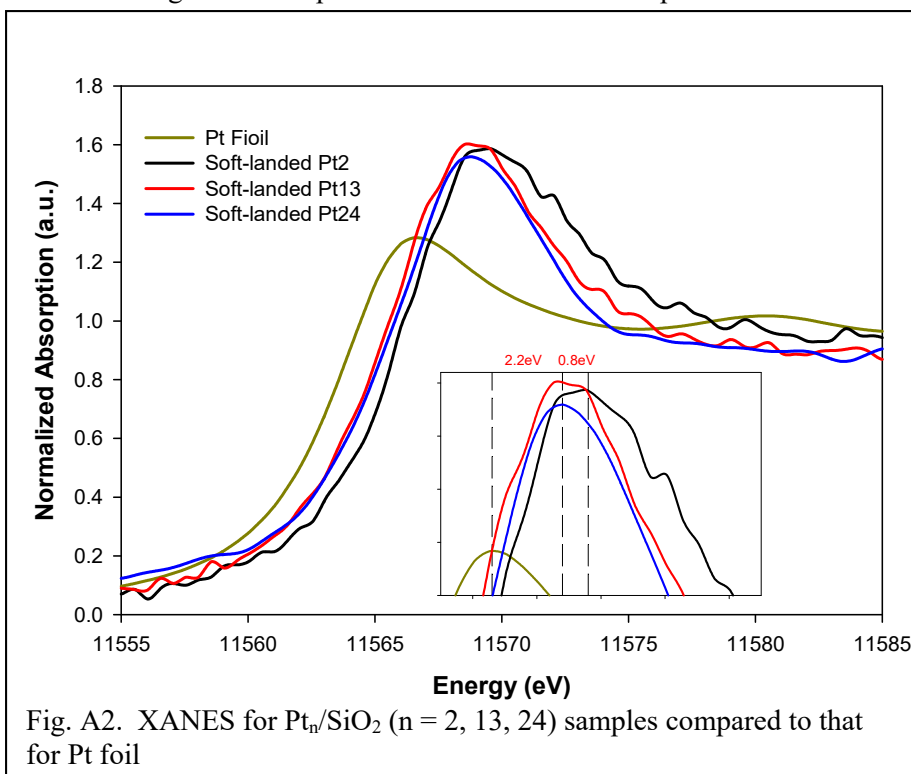
detail, samples of supported Pt clusters, where both size and oxidation state are measured along with XANES.

It can be seen that the edge for the cluster samples is shifted to higher energy, compared to that for Pt foil, and the white line intensity is higher. If these changes were interpreted by reference to XANES for bulk Pt and Pt oxides, we would conclude that the small clusters are oxidized. In this case, however, we have evidence (Fig. A3) that the clusters are in the Pt^0 oxidation state, and are actually quite oxidation resistant.

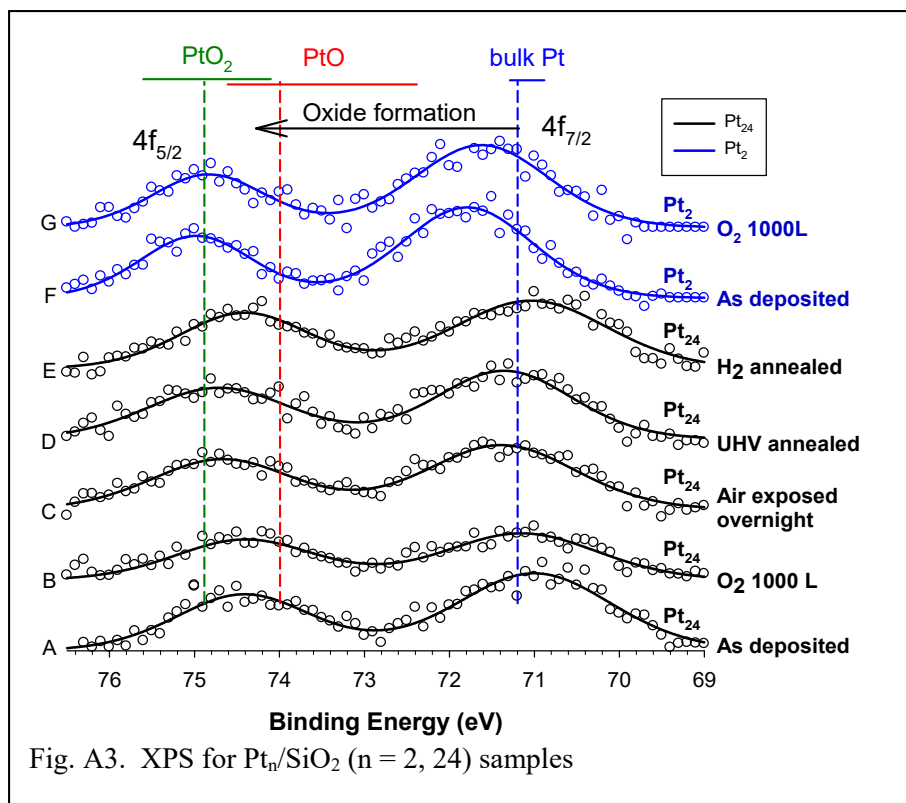Fig. A3. XPS for Pt_n/SiO_2 (n = 2, 24) samples

Fig. A3 compares X-ray photoelectron spectra (XPS) for Pt_2/SiO_2 and Pt_{24}/SiO_2 – the smallest and largest clusters studied. There are two fine structure components to each spectrum – the peaks labeled Pt $4f_{7/2}$ and $4f_{5/2}$. Since the two peaks always have the same spacing and relative intensity, we follow the usual convention of giving binding energy numbers only for the larger $4f_{7/2}$ peak. For comparison, the figure also gives both the range (horizontal bars) and mean values (vertical dashed lines) reported for the $4f_{7/2}$ binding energy for bulk Pt, PtO, and PtO_2. Note that the binding energy shifts three to four electron volts when Pt is oxidized to form PtO or PtO_2.

First consider the "as-deposited" spectra, which are for samples prepared in UHV, and never exposed to any oxidizer or other species and thus expected to be in the Pt^0 oxidation state. It can be seen that for Pt_2, the binding energy is significantly above the bulk Pt value, while the binding energy for Pt_{24} is slightly below. We expect that the binding energies for small clusters should be higher than that for the bulk, due to effects of size on screening of the final state core hole. The fact that the binding energy is slightly below the bulk value for Pt_{24} tells us that there is net electron transfer from the SiO_2 support to the Pt clusters, i.e., the clusters are actually in a slightly "over-reduced" state.

The question is whether the clusters oxidize during air exposure, because the samples in Fig. A2 had been exposed to air during transfer to Argonne. (Experiments were also done on samples transferred under N_2, with similar results). As shown in Fig. A3, exposure to 1000 L of O_2 results in no significant shift in the Pt_{24} spectrum, and a slight shift to *lower* binding energy for Pt_2. If the clusters were oxidizing, we would expect a large 3 – 4 eV shift to higher binding energy. For Pt_{24} we also exposed a sample to ambient air overnight, and then re-measured the XPS. In this case, there is a slight shift to higher binding energy, but nothing like the shift that would occur if an oxide like PtO or PtO_2 were forming.

As summarized in Fig. A4, we also probed the effects of O_2 and CO exposures, and of annealing in both UHV and H_2, using ISS. Inset a) shows a raw ISS spectrum. The main point of interest is how the intensity of the Pt peak changes for different sample treatments, and as a function of exposure to the He^+ beam, as it slowly sputters material from the sample surface. ISS intensities probe the fraction of each type of atom that appears in the top-most layer of the sample. Therefore, the Pt ISS intensity is

sensitive to processes such as sintering of small clusters into large 3D particles, or to binding of adsorbates on the cluster surface.

Frame b) of the figure compares the Pt intensity vs. He$^+$ exposure for soft- and hard-landed Pt$_{24}$ (clusters deposited at higher impact energies, to create defects in the SiO$_2$ support). Note that the Pt intensity for hard landing is initially lower, but decays more slowly than that for soft landing. This tells us that the hard-landed Pt$_{24}$ is partially embedded in the SiO$_2$ support, which is of interest as a possible strategy for stabilizing clusters against thermal sintering at high temperatures.

Frame c) compares Pt intensities for soft-landed Pt$_{24}$, both as-prepared and after exposure to 10 L of CO or 1000 L of O$_2$. CO is of interest because we know from previous work that it binds on top of the Pt clusters, and as expected, this results in low initial Pt ISS intensity, because CO attenuates He$^+$ scattering from the underlying Pt. Another signature of adsorbed molecules is that the Pt ISS intensity initially increases with He$^+$ exposure, as the CO adsorbates are sputtered off, exposing Pt. The same thing occurs after O$_2$ exposure, thus these measurements tell us that oxygen is binding to the cluster surface in
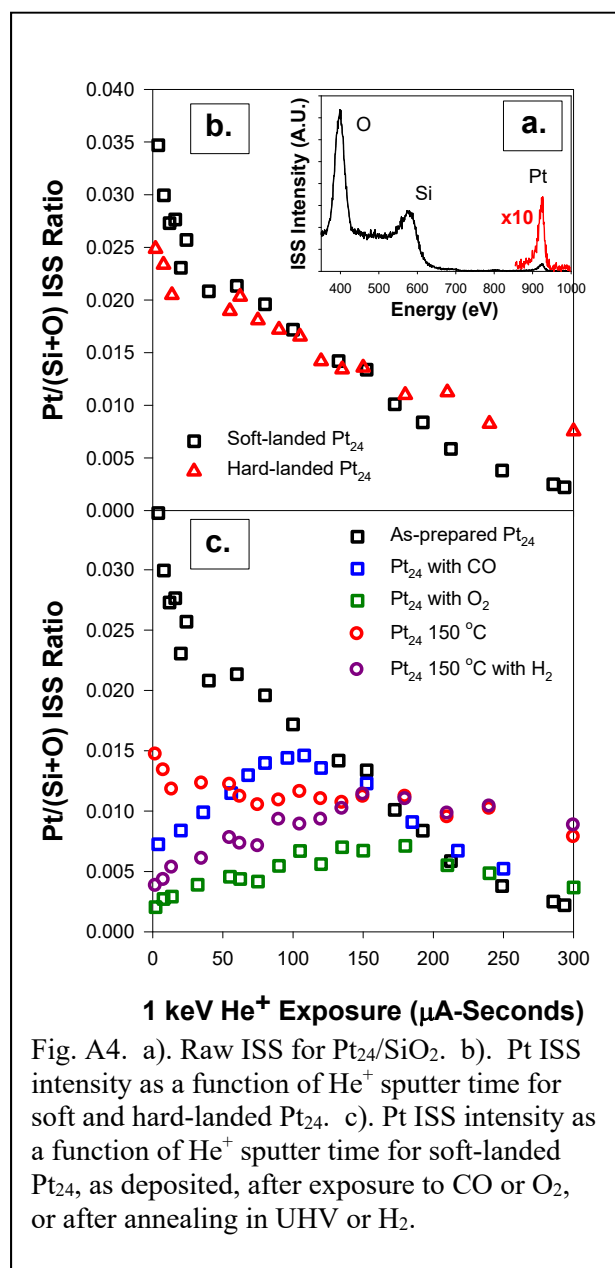
Fig. A4. a). Raw ISS for Pt$_{24}$/SiO$_2$. b). Pt ISS intensity as a function of He$^+$ sputter time for soft and hard-landed Pt$_{24}$. c). Pt ISS intensity as a function of He$^+$ sputter time for soft-landed Pt$_{24}$, as deposited, after exposure to CO or O$_2$, or after annealing in UHV or H$_2$.
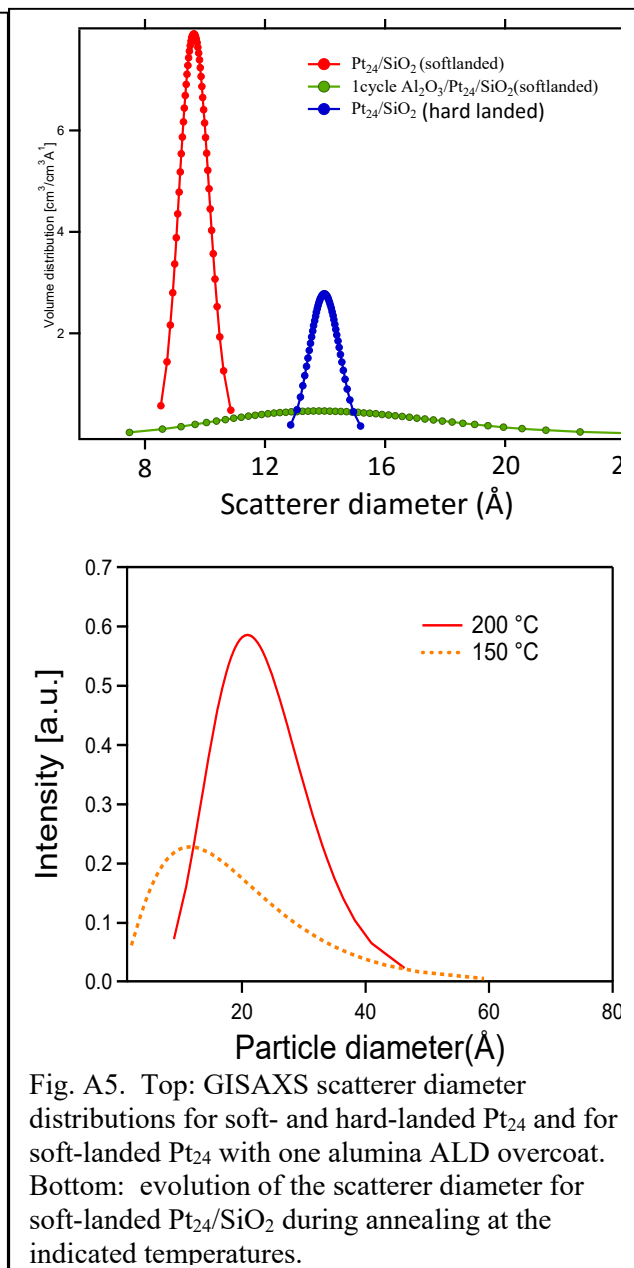
Fig. A5. Top: GISAXS scatterer diameter distributions for soft- and hard-landed Pt$_{24}$ and for soft-landed Pt$_{24}$ with one alumina ALD overcoat. Bottom: evolution of the scatterer diameter for soft-landed Pt$_{24}$/SiO$_2$ during annealing at the indicated temperatures.

some fashion. Note however, that the XPS results in Fig. A3 clearly show that this oxygen does not result in formation of anything resembling a true Pt oxide. The difference is that true oxides are a network of alternating Pt and O atoms, with no Pt-Pt bonding, whereas the clusters retain their Pt-Pt bonding network, and simply have a few O atoms bound on the surface.

The sample annealed in UHV has lower initial Pt intensity than the as-prepared sample, and because the signal simply decreases slowly with He^+ exposure, we can say that the effect is entirely due to formation of larger 3D structures, where the fraction of Pt in the top-most layer is reduced. The sample annealed in H_2 shows signs of both sintering to 3D structure, and adsorption of H on the surface.

The Argonne group also used grazing-incidence small angle X-ray scattering (GISAXS) to study the samples, and how they evolve with temperature. The top frame of Fig. A5 shows that soft-landed Pt_{24} appears as a narrow distribution of scatterer diameters, peaking at 0.96 nm, which is what would be expected if Pt_{24} remained intact upon deposition and during transport in air to Argonne. The hard-landed Pt_{24} appears bigger, but this reflects the disorder created during embedding the cluster in the SiO_2 support, rather than sintering into larger particles. The ALD-overcoated Pt_{24} shows a broad scatterer distribution, again reflecting disorder caused by deposition of alumina on and around the clusters. It was found that if the cluster samples were annealed in an H_2/He atmosphere, the size distribution was stable up to ~100 °C,

but for 150 or 200 °C, the distribution began to broaden and shift to larger diameter, as shown in the lower frame of the figure. This indicates that the clusters were stable to 100 °C, but sintered to larger nanoparticles with hundreds of atoms at higher temperatures.

The main point of the work is that XANES for small clusters shows shifted absorption edges and high white line intensities (Fig. A2), similar to what is seen for Pt oxides, even though the clusters are not oxidized (Fig. A3). The question, thus, is why? The shift in edge energy is easy to understand. It is well known from UPS, that particles develop increasing band gaps as size decreases. Band gaps are reflected by stabilization of the highest occupied energy levels or orbitals for small clusters, and these energies are shown in Fig. 6, as measured for Pt_n/SiO_2 by Eberhardt *et al.*[6] and for a wider size range of Pt_n/alumina by my group.[3]   If the Fermi level is in the middle of the band gap, then as the band gap increases, the energy of the lowest unoccupied level should increase, which will result in a shift of the L3 edge to higher energy with decreasing size, as is observed.

Fig. A6. Comparison of the shift in XANES L3 edge and the HOMO energies, as measured by UPS.

The white line intensity depends on both the density of unoccupied states and the transition probabilities to those states. There may be density of states factors that contribute to the enhanced intensity, however, it is clear that there should be enhancement in the transition probability. For bulk metal, the initial state is an electron in a core orbital on one Pt atom, but the final state is a delocalized conduction band state, which has poor overlap with the initial state. For small clusters, the final state is much more localized, and this should increase the transition probability.

B. Boron-doping effects:

The goals of this work were to explore ways of selectively doping small, size-selected Pt clusters with boron, and then to examine the effects of boron on the coking tendency of supported Pt_n/alumina model catalysts. The work was motivated by recent studies showing that boron doping reduced coking on Fischer-Tropsch catalysts – another environment where metal catalysts are exposed to high temperatures
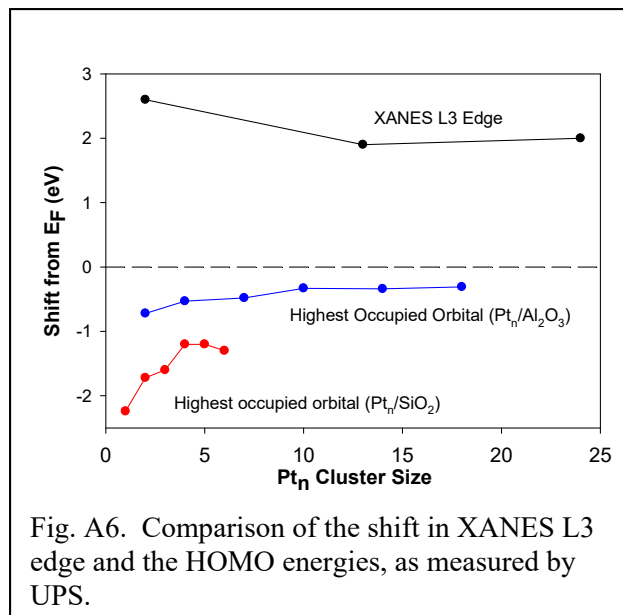
in hydrocarbon-rich, coking environments. The experimental work at Utah was carried out in parallel with theory at UCLA, discussed in the next chapter of the report.

To selectively dope supported Pt_n, without doping the support, required some reactant that would bind strongly to the Pt clusters and decompose to deposit boron, while being inert with respect to the support. Diborane turns out to work well, as shown by Fig. A7, which shows ISS data for a Pt_7/alumina model catalyst as deposited, and after 3 Langmuir (3 L) exposure to diborane done at 130 K. The three post-diborane spectra are for the as-exposed sample at 130 K, and for samples that were flashed to 300 K or 700 K after the 130 K exposure. The peaks are proportional to the concentrations of O ($E/E_0 \approx 0.39$), Al (0.55), and Pt (0.88) atoms in the top-most sample layer.

Fig. A7. ISS for Pt_7/alumina as deposited, and after 130 K diborane exposure with, and without flashing to higher surface temperatures.

As deposited, the Pt intensity is high, because all the Pt atoms are exposed in the surface layer. After the 130 K diborane exposure, the Pt intensity is attenuated by ~65%, indicating that the Pt clusters have adsorbed diborane that attenuates scattering from underlying Pt. There is also ~20% attenuation of the Al signal, but little attenuation of O, suggesting that there is a small amount of diborane adsorbed on the alumina support, mostly on Al sites. Flashing to 300 K leads to complete recovery of the Al and O signals, indicating that diborane adsorbed on the support simply desorbs when heated. After the 300 K flash, the Pt signal recovers to ~55% of its as-deposited value, reflecting some combination of desorption and decomposition of diborane that left only ~half the Pt atoms covered. The theory results show that diborane does decompose on small Pt clusters on alumina.

After the 700 K flash the Pt signal is also recovered to the as-deposited value. One might think that this indicates that diborane initially adsorbed on the Pt clusters had simply desorbed, however, the chemistry of the clusters is very different after diborane adsorption and 700 K heating, indicating that boron is still around, but no longer on the surface of the clusters. The theory provides an explanation. It shows that diborane initially adsorbs and decomposes on the cluster surface (where it affects ISS), but that the most stable boron binding sites are *under* the Pt clusters, anchoring the Pt to oxygen sites on the alumina. In this geometry, we not expect boron to have any effect on the Pt ISS signals.

One chemical effect of this "hidden" boron can be seen in Fig. A8, which shows experiments using CO to study the number and

Fig. A8. CO TPD from Pt_7/alumina, and a clean alumina film, showing the effects of boronation.

energy of CO binding sites on the samples. CO binds strongly to Pt, but does not react, and is thus a good probe molecule. The temperature-programmed desorption (TPD) experiment was done on separate samples of each type, and consists of exposing the sample to CO at 180K, cooling to ~130 K, and then heating at 3 K/sec while monitoring CO desorption. It can be seen that very little CO binds to the Pt-free alumina film, but that all the samples with Pt_7 show strong desorption. The main point to be gotten is that
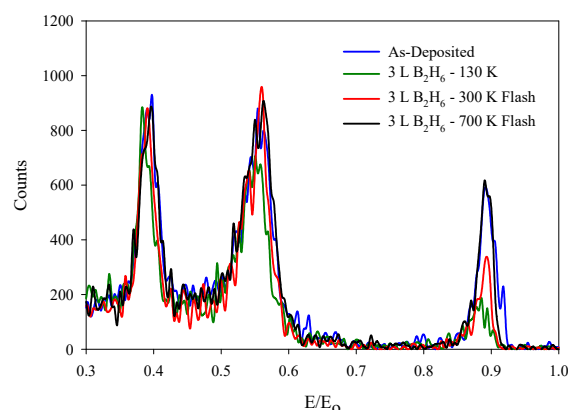
the number of CO molecules desorbing from Pt_7/alumina without boronation is ~0.4 CO/Pt atom, and that the desorption is at high temperatures, indicating strong CO binding. After boronation (with flashing to either 300 or 700K), the amount of CO desorbing is reduced by ~30%, and the desorption temperatures are all substantially lower, indicating that the Pt-CO binding is weakened.

Fig. A9 shows a set of similar TPD results for ethylene on Pt_n/alumina, for n = 4, 7, and 8 (sizes also studied in the theory). Note that the goal here is to lower the desorption temperature of ethylene, and to reduce the amount of dehydrogenation. In the endothermic fuel application, we want to dehydrogenate alkanes to alkenes, but we do not want to go further to produce alkynes, because these are coke precursors. As shown in the figure, ethylene sticks to the alumina support at low temperatures, but simply desorbes intact. For Pt_n/alumina without boron, there is a new desorption feature for intact ethylene at ~300K, but also a substantial feature for D_2 at high temperatures, indicating that about half the adsorbed ethylene undergoes dehydrogenation, producing D_2 and coking the catalyst.

For the samples with diborane exposure (and a 300 K flash), the amount of intact ethylene desorption is reduced and the desorption temperature is substantially lowered, indicating that boronation has weakened the ethylene-Pt bond strength (desireable). In addition, the amount of D_2 desorption is greatly reduced, indicating that almost all the ethylene desorbs without dehydrogenating to form coke (highly desireable). The effect of boronation, which includes a 300 K flash, is much larger than the effect of just a temperature flash alone.

These results are promising, indicating that boronation may be a practical strategy for reducing coking. The theory results are consistent, showing reduced affinity for carbon after boronation. In addition, it appears that boronation enhances the Pt-substrate binding, which should help stabilize the catalytic clusters against thermal sintering.
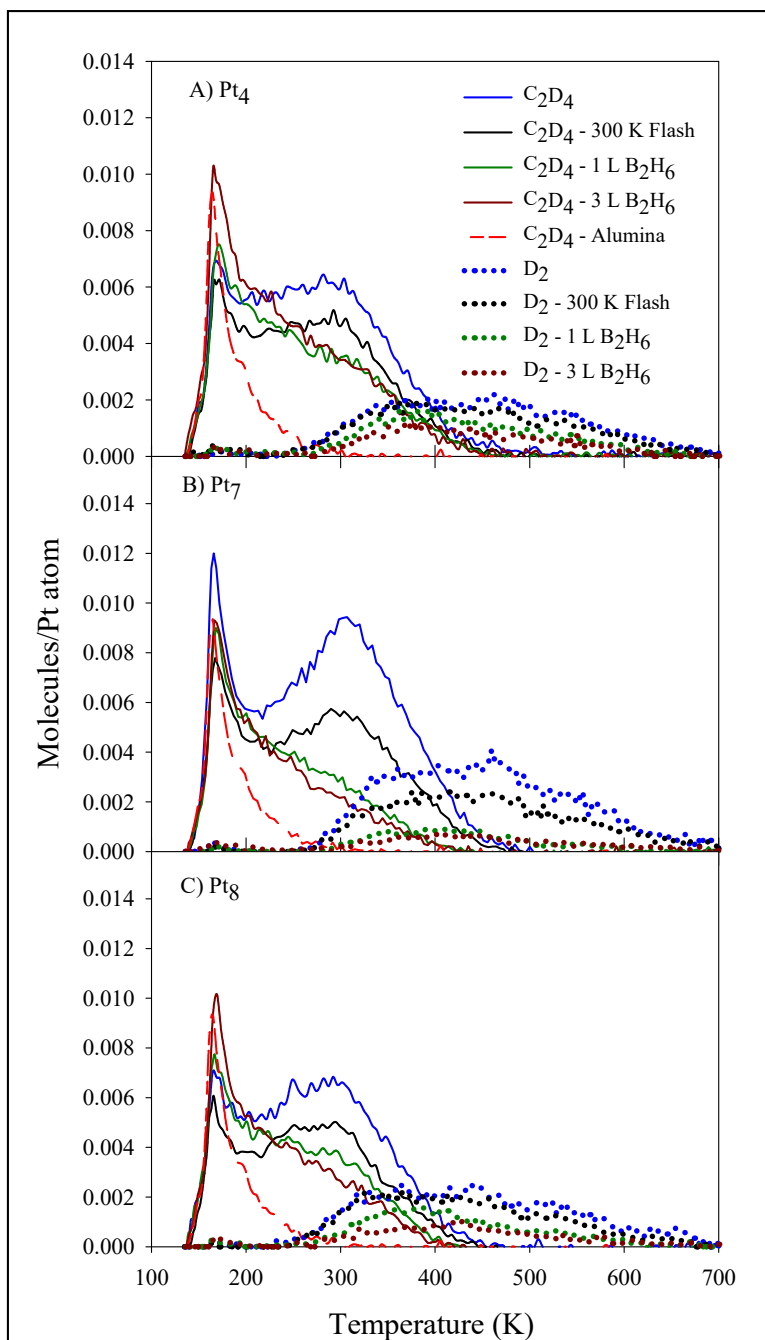
Fig. A9. C_2D_4 TPD from Pt_n/alumina (n = 4, 7, 8). The data labeled "C_2D_4" are for desorption of intact, unreacted ethylene. The data labeled "D_2" show the dehydrogenation product. Data for as-prepared Pt_n/alumina samples are simply labeled C_2D_4 and D_2. The other data series show the effects of flashing the samples to 300K, or exposing to either 1L or 3L of diborane and then flashing to 300 K. The data labeled "Alumina" are for a blank Pt-free alumina surface.

Energetic Nanoparticle Studies:

Archival publications 2, 4, 5, 8, and 9 have reported our work this area, and we are writing additional publications on our use of boranes to produce aluminum nanoparticles, and their effects on hypergolic ignition of candidate IL propellants (additional publications 13, 14). The major findings in this area were:

1. Mechanical attrition from aluminum (and other metal) balls produces nanoparticles very efficiently, if done in the presence of appropriate milling agents such as acetonitrile or oleic acid. The particles produced are capped with an organic layer that partially passivates them. Contamination levels are substantially lower than in conventional milling of powders.

2. Nanoparticle production is more efficient, and produces a narrower size distribution if it is done using *gaseous* milling agents, such as diborane, pentaborane, acetonitrile vapor, ammonia, or methylamine. These particles, particularly those generated with acetonitrile vapor or boranes, are highly reactive (Fig. A10), but can be passivated for handling in air by further functionalization with ligands like oleic acid.

3. Hypergolic ignition delay times for ILs such as 1-methyl-4-amino-1,2,4-triazolium dicyanamide ([MAT][DCA]) and 1-Allyl-3-methylimidazolium dicyanamide ([AMIM][DCA]) are only very slightly affected by loadings of up to 25 wt% of aluminum nanoparticles. This highly desirable behavior suggests that the particles must participate in the ignition process.

Because most of this work is in print, I will use the borane-capped aluminum work, which is in the process of being written up, to illustrate our results. The work involves particle synthesis and physical/surface chemistry characterization at Utah, detailed quantum chemistry theory at Edwards AFB (Boatz), additional thermal characterization at Wright Patterson AFB (Bunker and Lewis), and hypergolic ignition studies at both Edwards AFB (Chambreau, Vaghjiani) and Alabama (Rogers). I will focus on the Utah part of the work, since that is what was funded by the grant.

Aluminum is challenging to mill, because it is so malleable and ductile. As a result, milling powdered aluminum feedstock without an appropriate milling agent actually leads to formation of 2 – 3 mm diameter spheroids, by cold welding of the powder. With an appropriate milling agent, it is possible to mill Al powder into the nanoscale, however, because powdered feedstocks have an oxidized surface layer, the nano-product also has considerable oxygen contamination. We developed the approach of

attriting nanoparticles from the surface of aluminum and other malleable metal balls as a way to minimize contamination (publication 8). The balls are cleaned by attriting and discarding the surface layer, and then are stored and handled under N_2 or Ar to prevent re-oxidation.

The idea of using boranes as milling agents for aluminum nanoparticle production came from a pair of previous studies, in which we showed that milling boron in an H_2 atmosphere resulted in rapid production of B-H terminated boron nanoparticles,[7] and that these particles could be capped with either alkenes or alkene-functionalized ILs,[8] providing air-stable un-oxided boron particles with good solubility in hydrocarbons and ILs, respectively. We found that H_2 does not work as a milling agent for aluminum – resulting in no nanoparticle formation. We also examined use of NH_3 and monomethylamine as milling agents, finding that they did give substantial nanoparticle production, but resulted in particles passivated by a thick nitride-like layer (publication 4). We also recently compared nanoparticle production in gaseous and liquid acetonitrile, finding much more efficient product of
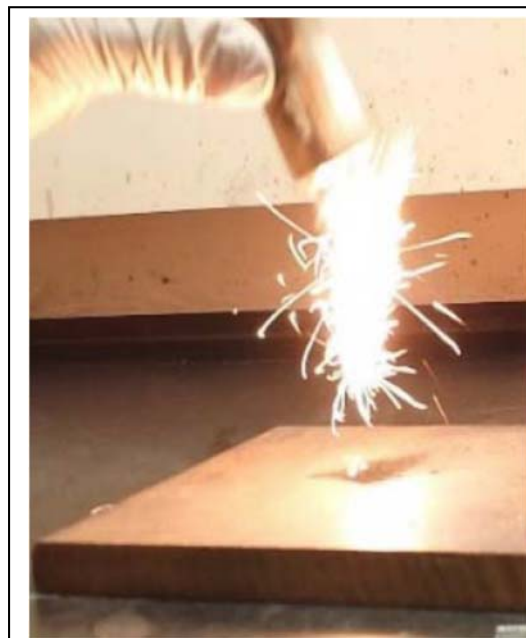

Fig. A10. Pyrophoric ignition of Al nanopowder produced by attrition from Al balls under acetonitrile vapor.

nanopowder, and a narrower size range, for vapor-phase milling (publication 2). These particles are highly active, as shown in Fig. A10.

Milling Al balls in either diborane or pentaborane vapor results in rapid nanoparticle production, and consumption of the borane, with production of H_2 as the only gaseous product, as determined by sampling the milling jar headspace for mass spectral analysis. The diborane-milled particles were found to be pyrophoric, but somewhat less reactive than the particles shown in Fig. A10. The pentaborane-milled product is explosively pyrophoric, cracking the glass vial used to bring the particles out of the glove box for the ignition test. The particles were passivated for handling by either slow air oxidation, or by reacting with octene, or by capping the surface with oleic acid. As shown in Fig. A11, the mass-weighted size distribution is dominated by particles with hydrodynamic size in the 30 – 50 nm range. The component near 1000 nm results from aggregates, because these particles did not form very stable suspensions in the acetonitrile used as a DLS solvent.

Fig. A11. Volume-weighted size distribution determined by DLS for Al nanoparticles produced by milling in diborane vapor.

Fig. A12 shows a small aggregate of pentaborane-capped particles, stabilized by oleic acid capping, as imaged in our STEM, after passivation by slow air exposure. The secondary electron image (upper left) shows the flake-like particle shapes, and it can be seen that the elemental maps for boron and aluminum are essentially coincident. The carbon map reflects the oleic acid capping, and the carbon fiber supporting the particles. The STEM results show that the boron content averaged over the thickness of the particles, is about 2 – 3 percent. The question is whether the boron is primarily on the particle surfaces, or if it is distributed throughout the bulk. We used X-ray photoelectron spectroscopy (XPS) to look at the top few nanometers of the particle surfaces, and find a B:Al intensity ratio of ~20%, i.e., the particle surface is strongly enriched in boron, as would be expected if the boranes are binding to the aluminum surface. The calculations of our collaborator Jerry Boatz (AFRL/Edwards AFB) support this analysis – showing that boranes bind and decompose on aluminum surfaces.

Fig. A13 shows the XPS results for the B 1s and Al 2p spectral regions, in the top and bottom frames, respectively. The higher energy of the two peaks in each spectrum is for oxidized boron or aluminum, and the lower energy peak is for zero oxidation state B^0 or Al^0. To enable transfer of the pyrophoric samples to the XPS instrument, it was necessary to passivate the material. For the as-
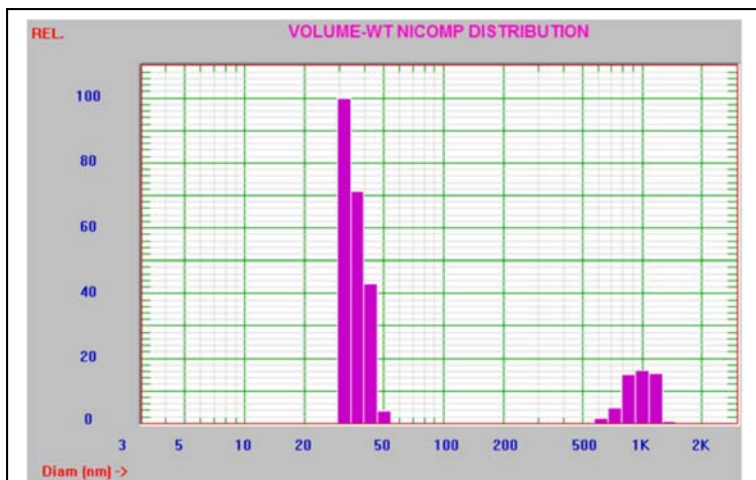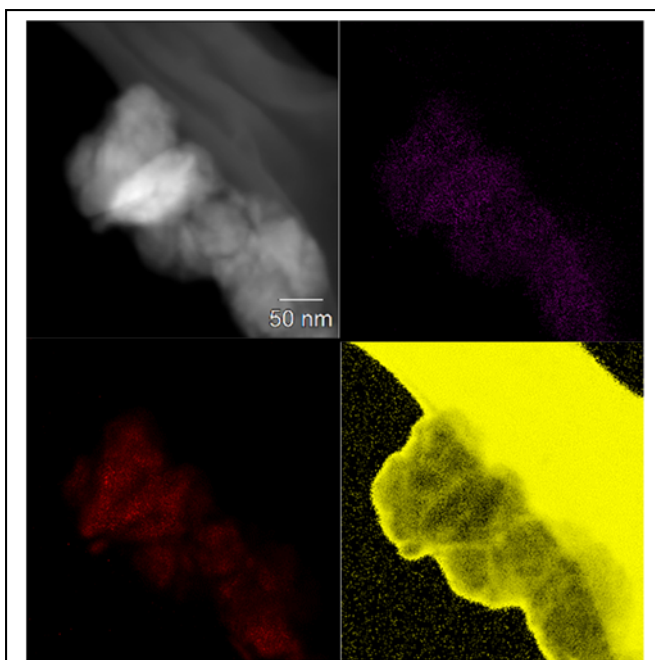

Fig. A12. Upper left: STEM image of a small aggregate of pentaborane-capped aluminum particles. Upper right: Boron map. Lower left: Aluminum map. Lower right: Carbon map.

milled materials (which are highly pyrophoric) this was done by slowly exposing them to a few Torr of air, to allow slow oxidation. Not surprisingly, both the boron and aluminum in these as-milled particles are substantially oxidized. Indeed, it is surprising that any un-oxidized boron is present at all, since the boron is primarily in the surface layer. The substantial B^0 peak (188 eV) for pentaborane-milled aluminum suggests that there must be some boron incorporated below the surface layer. The aluminum spectra for all samples shows both oxidized aluminum (74 eV) and unoxidized aluminum (71.5 eV).

An exciting result for these particles was obtained in collaboration with Steve Chambreau and Gammy Vaghjiani (Edwards AFB) who used their step-scan FTIR spectrometer to look at ignition delay times for hypergolic ILs loaded with both boron, aluminum, and boron-capped aluminum nanoparticles. Ignition was initiated by mixing with fuming nitric acid, and monitored by the growth in CO_2 IR spectral lines. The results are shown in Fig. A14. If ignition were purely a reaction between the IL and nitric acid, we would expect that loading the IL with particles should slow ignition, due to the extra mass of particles that act as a heat sink. This behavior is, indeed, observed for [MAT][DCA] loaded with boron

Fig. A13. XPS for borane-milled aluminum. Top: Boron 1s spectral region. Bottom: Al 2p

nanoparticles (triangles), where the ignition delay increases by a factor of five, as particle loading increases from 0 to ~25%. Note, however, that for the experiments with aluminum or boron-capped aluminum nanoparticles, the slopes of the ignition delay vs. loading best-fit lines are much lower.

For [MAT][DCA] loaded with Al, there is almost no effect of loading. These Al particles are those prepared by milling Al balls in acetonitrile vapor (Fig. A10). Similarly, there is almost no effect of loading [MAT][DCA] with Al particles prepared by milling in diborane. We also prepared samples of boron-capped aluminum, and hydrogen-capped boron, both suspended in [AMIM][DCA], and these also show weak dependence on particle loading.

The weak dependence on loading is interesting from a mechanistic perspective. Although the details of the complex hypergolic ignition process are not at all clear for these particle-loaded samples, it is clear that some combination of the following effects must be occurring, in order to offset the particle heat sink effect: 1. There may be significant heat release from reaction of the nitric acid with the
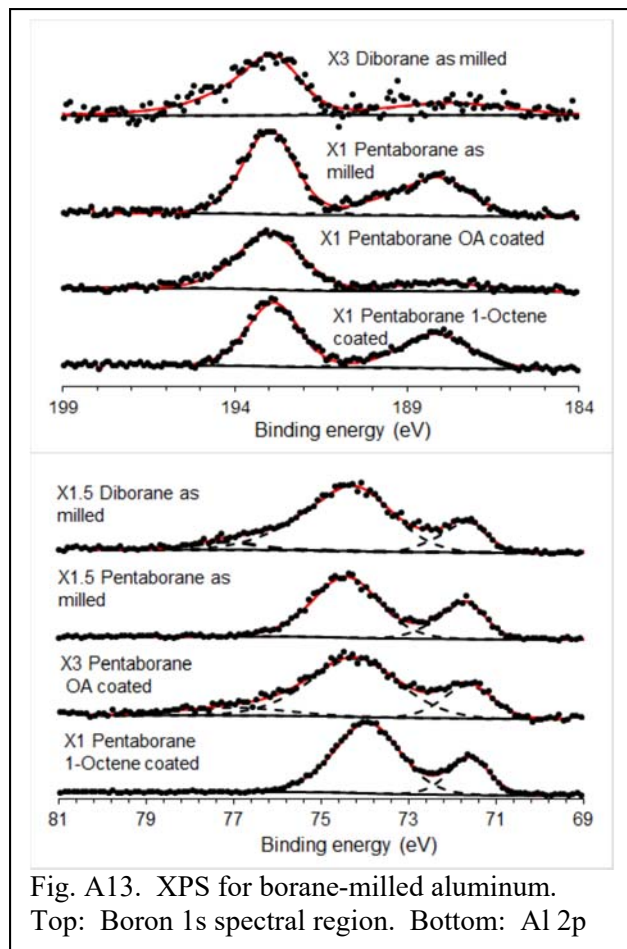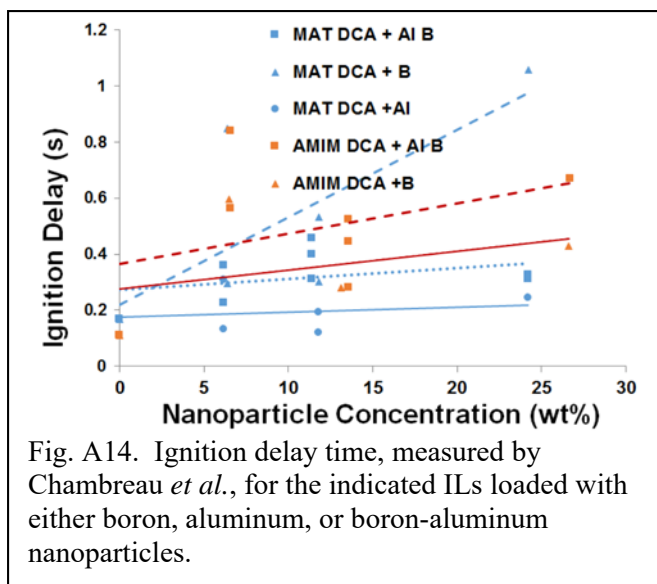

Fig. A14. Ignition delay time, measured by Chambreau et al., for the indicated ILs loaded with either boron, aluminum, or boron-aluminum nanoparticles.

particles, 2. The particle surfaces may act as catalysts that accelerate the nitric acid-IL reaction, and/or 3. The particles may act as blackbodies, enhancing radiative feedback from the reaction front to the bulk of the mixture.   Regardless of the mechanism, this behavior is quite important. To achieve substantial enhancements in propellant energy density, it will be necessary to add energetic particles to high loadings. These results show that at least for some IL-particle combinations, high loadings do not significantly degrade ignition.

References cited in this section

1.   Dai, Y.; Gorey, T. J.; Anderson, S. L.; Lee, S.; Lee, S.; Seifert, S.; Winans, R. E., Inherent Size Effects on XANES of Nanometer Metal Clusters: Size-Selected Platinum Clusters on Silica. *J. Am. Chem. Soc.* **2016**, *(submitted)*.

2.   Kane, M. D.; Roberts, F. S.; Anderson, S. L., Effects of Alumina Thickness on CO Oxidation Activity over Pd_{20}/Alumina/Re(0001): Correlated Effects of Alumina Electronic Properties and Pd_{20} Geometry on Activity. *J. Phys. Chem. C* **2015**, *119*, 1359–1375.

3.   Roberts, F. S.; Kane, M. D.; Baxter, E. T.; Anderson, S. L., Oxygen activation and CO oxidation over size-selected Ptn/alumina/Re(0001) model catalysts: correlations with valence electronic structure, physical structure, and binding sites. *Phys. Chem. Chem. Phys.* **2014**, *16*, 26443 – 26457.

4.   Lee, S.; Lee, B.; Seifert, S.; Vajda, S.; Winans, R. E., Simultaneous measurement of X-ray small angle scattering, absorption and reactivity: A continuous flow catalysis reactor. *Nucl. Instrum. Methods Phys. Res., Sect. A* **2011**, *649*, 200-203.

5.   McMahon, B. W.; Perez, J. P. L.; Yu, J.; Boatz, J. A.; Anderson, S. L., Synthesis of Nanoparticles from Malleable and Ductile Metals Using Powder-Free, Reactant-Assisted Mechanical Attrition. *ACS Appl. Mater. Interfaces* **2014**, *6*, 19579−19591.

6.   Eberhardt, W.; Fayet, P.; Cox, D.; Fu, Z.; Kaldor, A.; Sherwood, R.; Sondericker, D., Core level photoemission from monosize mass selected platinum clusters deposited on silica and amorphous carbon. *Phys. Scr.* **1990**, *41*, 892-5.

7.   Perez, J. P. L.; McMahon, B. W.; Yu, J.; Schneider, S.; Boatz, J. A.; Hawkins, T. W.; McCrary, P. D.; Flores, L. A.; Rogers, R. D.; Anderson, S. L., Boron Nanoparticles with High Hydrogen Loading: Mechanism for B−H Binding and Potential for Improved Combustibility and Specific Impulse. *ACS Appl. Mater. Interfaces* **2014**, *6*, 8513-8525.

8.   Perez, J. P. L.; Yu, J.; Sheppard, A. J.; Chambreau, S. D.; Vaghjiani, G. L.; Anderson, S. L., Binding of Alkenes and Ionic Liquids to B-H Functionalized Boron Nanoparticles: Creation of Particles with Controlled Dispersibility and Minimal Surface Oxidation. *ACS Appl. Mater. Interfaces* **2015**, *7*, 9991-10003.

Archival publications, in print, in press, and submitted.

1. "Inherent Size Effects on XANES of Nanometer Metal Clusters: Size-Selected Platinum Clusters on Silica", Yang Dai, Timothy J. Gorey, Scott L. Anderson, Sungsik Lee, Sungwon Lee, Soenke Seifert and Randall E. Winans, J. Am. Chem. Soc. (submitted 8 2016)

2. "Aluminum Nanoparticle Production by Acetonitrile-Assisted Milling: The Effects of Liquid vs. Vapor Phase Milling, and of Milling Method on Particle Size and Surface Chemistry." Jiang Yu, Brandon McMahon, Jerry Boatz, and Scott Anderson, J. Phys. Chem. C (published online Aug. 11, 2016) DOI: 10.1021/acs.jpcc.6b04054

3. "The Effect of O_2 and CO Exposure on the Photoelectron Spectroscopy of Size-selected Pd_n Clusters Supported on TiO_2(110)", Arthur C. Reber, Shiv N. Khanna, F. Sloan Roberts, Scott L. Anderson. J. Phys. Chem. C 120 (2016) 2126-2138. DOI: 10.1021/acs.jpcc.5b08611

4. "Rapid Aluminum Nanoparticle Production by Milling in NH_3 and CH_3NH_2 Atmospheres: An Experimental and Theoretical Study", Brandon W. McMahon, Jiang Yu, Jerry A. Boatz, and Scott L. Anderson, ACS Appl. Materials Interfaces, 7 (2015) 16101–16116, DOI: 10.1021/acsami.5b04806.

5. "Binding of Alkenes and Ionic Liquids to B-H Functionalized Boron Nanoparticles: Creation of Particles with Controlled Dispersibility and Minimal Surface Oxidation", Jesus Paulo L. Perez,

Jiang Yu, Anna J. Sheppard, Steven D. Chambreau, Ghanshyam L. Vaghjiani, Scott L. Anderson, ACS Appl. Mater. Interfaces, 7 (2015) 9991–10003, DOI: 10.1021/acsami.5b02366

6. "Initial and Final State Effects in the Ultraviolet and X-Ray Photoelectron Spectroscopy (UPS and XPS) of Size-Selected Pd_n clusters Supported on TiO2(110)", F. Sloan Roberts, Scott L. Anderson, Arthur C. Reber, and Shiv N. Khanna, J. Phys. Chem. C 119 (2015) 6033-6046. DOI: 10.1021/jp512263w

7. "Effects of Alumina Thickness on CO Oxidation Activity over Pd_{20}/alumina/Re(0001): Correlated Effects of Alumina Electronic Properties and Pd_{20} Geometry on Activity", Matthew D. Kane, F. Sloan Roberts, and Scott L. Anderson, J. Phys. Chem. C 119 (2015), 1359–1375, DOI:10.1021/jp5093543.

8. "The Synthesis of Nanoparticles from Malleable and Ductile Metals using Powder-Free, Reactant-Assisted Mechanical Attrition", Brandon W. McMahon, Jesus Paulo L. Perez, Jiang Yu, Jerry A. Boatz and Scott L. Anderson, ACS Applied Materials and Interfaces 6 (2104) 19579-19591, DOI: 10.1021/am503845s.

9. "Boron Nanoparticles with High Hydrogen Loading: Mechanism for B−H Binding, Size Reduction, and Potential for Improved Combustibility and Specific Impulse", Jesus Paulo L. Perez, Brandon W. McMahon, Jiang Yu, Stefan Schneider, Jerry A. Boatz, Tom W. Hawkins, Parker D. McCrary, Luis A. Flores, Robin D. Rogers, and Scott L. Anderson, ACS Applied Materials and Interfaces 6 (2014) 8513-8525, DOI: 10.1021/am501384m

10. "Oxygen activation and CO oxidation over size-selected Pt_n/Alumina/Re(0001) model catalysts: correlations with valence electronic structure, physical structure, and binding sites", F. Sloan Roberts, Matthew D. Kane, Eric T. Baxter, Scott L. Anderson, Phys. Chem. Chem. Phys. 16 (2014) 26443 – 26457, DOI: 10.1039/c4cp02083a

11. "Thermal and Adsorbate Effects on the Activity and Morphology of Size-Selected Pd_n/TiO_2 Model Catalysts", William E. Kaden, William A. Kunkel, F. Sloan Roberts, Matthew Kane and Scott L. Anderson, Surface Science, 621 (2014) 40-50, DOI:10.1016/j.susc.2013.11.002

Additional publication in preparation

12. "Effects of Alumina Atomic Layer Deposition on Thermal Stability and Availability of Binding Sites for Pt_{24} on Silica and Alumina", Yang Dai, Timothy J. Gorey, Scott L. Anderson, Sungsik Lee, Sungwon Lee, Soenke Seifert and Randall E. Winans, J. Phys. Chem. C (to be submitted, Sept, 2016)

13. "Production and Characterization of Borane-Capped Aluminum Nanoparticles", Jiang Yu, Scott L. Anderson,[*] Jerry A. Boatz, Christopher E. Bunker, William K. Lewis, Elena A. Guliants, (in preparation for J. Mater. Res.)

14. "Effects of Aluminum, Boron, and Boron-Capped Aluminum Nanoparticle Addition on Ignition of Hypergolic Ionic Liquids", Steven Chambreau, Jerry Boatz, Stefan Schneider, Ghanshyam Vaghjiani, Robin Rogers, Jiang Yu, Scott L. Anderson, (in preparation of ACS Applied Materials and Interfaces).

15. "Binding Site Distributions, Electronic Properties, and Activity for Ethylene Dehydrogenation for Size-Selected Pt_n Clusters on Alumina", Eric T. Baxter, Ashley Cass, Scott L. Anderson, Mai-Anh Ha, and Anastassia Alexandrova, (in preparation for J. Phys. Chem. C).

16. "The Effects of Boronation on Binding Sites and Activity for Ethylene Dehydrogenation at Size-Selected Pt_n/alumina", Mai-Anh Ha, Anastassia Alexandrova, Eric T. Baxter, Ashley Cass, Scott L. Anderson, (in preparation for J. Phys. Chem. C).

People supported by the grant.
Graduate students: Eric Baxter, Yang Dai, Timothy Gorey, Brandon McMahon, Jiang Yu, Matthew Kane, R. Sloan Roberts.

Discoveries, inventions, and patent disclosures
"Production Of Particles Using Homogeneous Milling and Associated Products" Scott Anderson, Brandon McMahon, J. Paulo Perez, US patent 9,321700 B2, issued April 26, 2016

PI Name: Anastassia N. Alexandrova
Address: 607 Charles E. Young Drive East, Los Angeles, CA 90095-1569, USA

Statement of objectives: to perform calculations related to the structure, stability, catalytic activity toward dehydrogenation and cracking, coke resistance, and other properties of small size-selected clusters on supporting surfaces of oxides; to develop codes for multi-scale realistic modeling for such catalysts; to elucidate electronic effects governing the particular behavior of the systems, in order to provide the ground for physically-meaningful approaches for catalyst design. All calculations are to be done in close connection with the model experiments by Anderson, and in collaboration and complementing the theory and experiment by Mavrikakis and Dumesic.

Methodology developed: We developed two methods: (1) a Metropolis Monte Carlo method to simulate cluster sintering on the support, assuming the mechanism of Ostwlad ripening. The algorithm predicts the particles of the size and composition that are most likely to survive the longest at high temperatures of catalysis, and predictions agree with the experiment. The simulation includes the monomer migration, dissociation, evaporation, and redeposition, subject to energy changes precomputed with Density Functional Teory (DFT). Applications of the method are described in the sections below. (2) AFFCK (Fig AA1, JCTC 2015) – a global optimization method for clusters in the gas phase, and on supporting surfaces

Fig. AA1. AFFCK algorithm, employing a system-specific classical force field for a portion of geometry optimization at every step. The algorithm consists of simply putting atoms in a box and coalescing them, and then optimizing the species to the nearest stationary point. Redundant optimizations are recognized and terminated. Symmetry point groups are implemented. The graph at right shows how FF brings the population energies closer to DFT ones, at a small fraction of a cost.

(the latter currently available in the beta-version). It is arguably the fastest available algorithm, highly parallel and taking advantage of a classical force field developed on-the-fly for a given system, for a portion of every geometry optimization. Both methods are available upon request.

Accomplishments: In this section we will highlight only the most important accomplishments.
1. For the reduction of cluster **sintering** on the support, several projects have been accomplished, where the understanding of this process has been gained, and electronic structure specifics leading to greater or smaller sintering have been elucidated.
Using our sintering simulation method, we provided a viable hypothesis for the long-standing mystery of the stability of PtPd clusters of 50:50 ratio against sintering (ACS Catal 2014, Fig. AA2). Our simulations reproduced the unique stability at 50:50 (see the build-up of the population along the diagonals in Fig. AA2). We note that the simulation takes advantage of the prior global optimization for these clusters, in the gas phase and on the support, done with our AFFCK method. AFFCK yields the global and local minima, whose population at elevated temperature is evaluated, and energies and other properties are then averaged over the thermally accessible ensemble. Thus, temperature goes into the simulation via these cluster populations, and via the metropolis criterion in MC responsible fro the acceptance or rejection of attempted moves. We found that no electronic or chemical bonding reason make the 50:50 clusters more
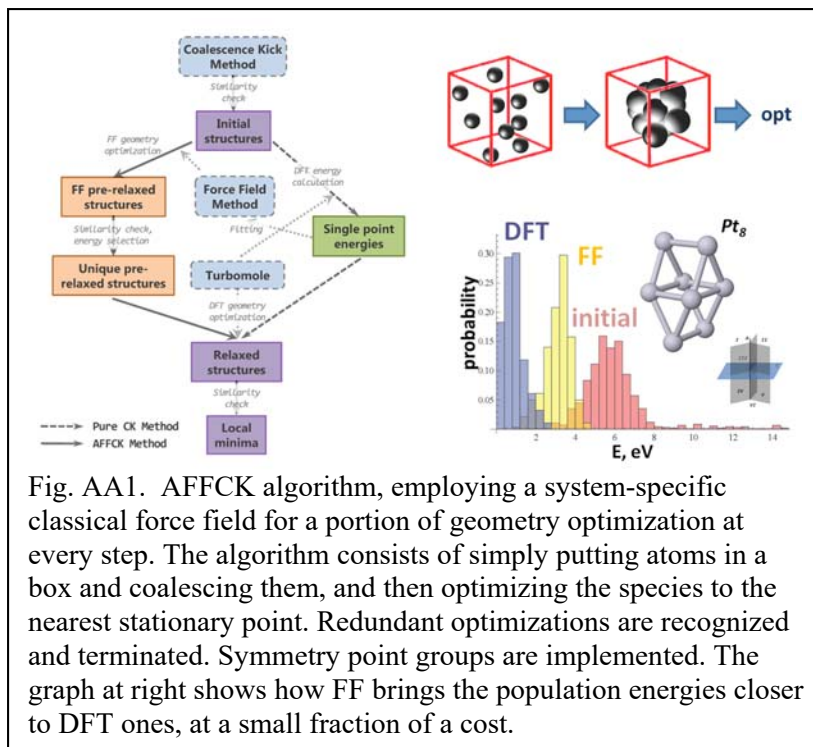
stable, but there is an entropic stabilization, due to the existence of many more thermally-accessible isomers on the potential energy surface at elevated T than for clusters of other compositions.

We also learned that, at least in small clusters, the addition of Zn (a promising additive to Pt for selective dehydrogenation) is not beneficial; this is because the system either looses Zn via evaporation or Pt and Zn undergo phase-separation, creating clusters formed primarily of Pt and of Zn (JPC C 2015, Fig. AA3). The reason was found to be in the very weak adsorption of Zn on MgO, and the preference of Zn to bind to Ti rather than O in titania. It is also an important result because it shows that our sintering simulations can reproduce various sintering behaviors,
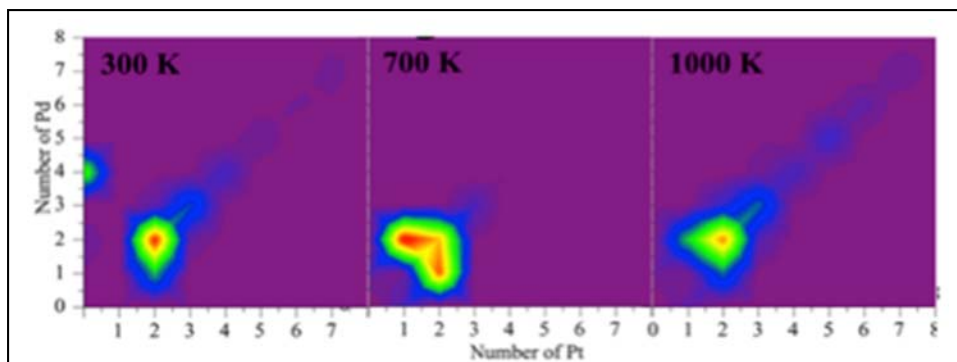

Fig. AA2. Sintering behavior of mixed PtPd clusters at varying temperatures: the simulation reproduces the higher stability of the equimolar PtPd clusters
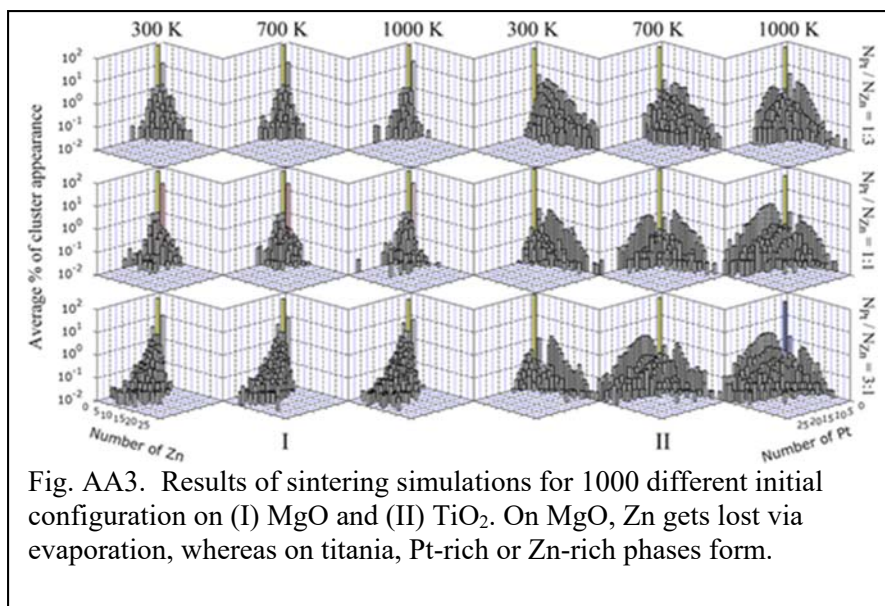

Fig. AA3. Results of sintering simulations for 1000 different initial configuration on (I) MgO and (II) TiO_2. On MgO, Zn gets lost via evaporation, whereas on titania, Pt-rich or Zn-rich phases form.

and do not always favor clusters of specific compositions.

Mixed PtZn clusters were investigated also for their interesting structural properties on MgO. It turns out that at the small size of 5 toms, these cluster are flat and upright on the support, due a combination of strong charge transfer from the support, onset of partial covalency (or second order Jahn-Teller effect), and matching the position of surface O atoms (PCCP 2014, Cover Article).

2. For the reduction of **coking** (and also sintering), it was suggested by our team in UCLA that addition of B to deposited Pt clusters should help catalyst resistance and increase the life-time. Initially, a purely theoretical work was done (ACS Catal 2015, Fig. AA4), were this prediction was made for clusters of several sizes ($Pt_{2,3,4,5,12,13}$) deposited on MgO. For all considered cluster sizes, the affinity to C is reduced upon boration, suggesting the reduced propensity to the initiation of coke growth. At smaller sizes, B tends to form a B-O anchor to the support, also stabilizing these clusters against sintering. From the electronic structure standpoint, B reduces the amount of charge transfer from the support to the cluster, presumably depleting the population of the valence c- and p-AOs on Pt to be used for binding C. Based on this finding, we expect that on any surface that dopes Pt with electrons the effect of boration could have beneficial anticoking properties.

Fig. AA4. Structures of pure Pt and Pt doped with B, deposited on MgO, and decorated with a single C atom, as a coke initiator. These are identified global minima. $\Delta E_{stick}(C)$ indicate the difference in the affinity of clusters to carbon after and before boration. The negative numbers indicate that the affinity to C is reduced when B is added.

This proposal was further tested on a more relevant system: $Pt_{4,7,8}$ on a-Al_2O_3, experimentally (by Scott Anderson), and theoretically (by us). We found that in these systems it is also true that B reduces the affinity to coke, and thus enhances the selectivity of endothermic dehydrogenation processes. In the experiment, B is delivered to the surface-deposited clusters from the gas phase, in the form of B_2H_6. We found computationally that B_2H_6 spontaneously (without a barrier) losses some or most of H atoms and also undergoes the B-B bond cleavage on some isomers. We concluded that B gets incorporated into the clusters. The manuscript is now in progress. The role of B is in the reduction of charge transfer from the support to the clusters, which in turn affects the affinity of these clusters to C. The paper on this subject is currently in preparation, in collaboration with Scott Anderson.

In this latter study we also further emphasized a concept of a fundamental importance. Clusters have many low-energy isomers, and many of them become accessible at elevated temperatures of catalysis. Thus, it is no longer valid to think of the reactivity and properties of clusters in terms of a single cluster structure (the global minimum). Instead there is a statistical mechanical ensemble of accessible structures, with all kinds of available binding sites. In fact, not the global but one of the less stable local minima can be responsible for the catalytic behavior, and this must be taken into account in computational modeling. In our work on borated clusters, we found that when temperature is increased, and more and more isomers becomes accessible, pure Pt clusters on alumina coke more, whereas borated clusters coke less. If we would consider only the global minimum, we would completely miss this property, and coking propensities would be essentially identical. Currently, we are investigating the need for ensemble representation, trying to see if it can explain the unusual size-specific catalytic activities of clusters of certain sizes.

3. Several fundamental studies on hydride clusters in the gas phase have been accomplished, allowing us to better understand reasons for their stability (JPC Letter 2014, JCP 2014, JCP 2015, Fig. AA5). Hydrides of transition metals potentially could be reaction intermediates in dehydrogenation. The most exciting finding in this area is that when hydrogen binds to Pt in small clusters, it rarely stays as activated H_2 molecules. Instead, however, H atoms engage in nearly-covalent bonding with the metal, and together with its d-AOs organize delocalized MOs, which can classify these systems as σ-aromatic. Aromaticity is a stabilizing effect, with known implications for the reactivity, such as preferential reactions of substitution rather than addition. Thus, if at the given chemical potential of hydrogen, such species form in the course of a reaction, the intermediates can be expected to have such unusual properties.

Fig. AA5. σ-aromaticity explains the unusual shape and stability of $PtZnH_5^-$.
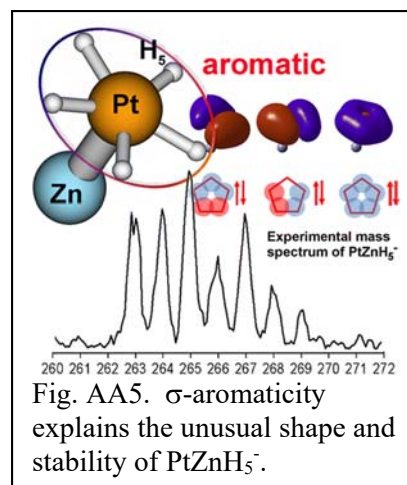
4. We additionally thoroughly investigated oxide supports, which act like ligands for small clusters, and can perturb them in a dramatic way. We particularly investigated their ability to form O vacancies on the surface and sub-surface, as well as the ability of these vacancies to bind small molecules and facilitate chemical reactions through electron transfer. In some cases the predicted location of the most stable Ov is critically dependent on the chosen theoretical method, which is troublesome. This is particularly true for anatase (Fig. AA6, JCTC 2016). The most stable Ov can be on the surface, sub-surface, and in several different location; additionally, Ov formally located in the same place may have different electronic configurations with slightly different geometries. Depending on the setting in DFT (magnitude of the Hubbard U, presence of exchange, spin polarization, and choice for the functional), the most stable Ov is changing. Most usually, it is found to be on the surface. Spanning

Fig. AA6. The many possible positions of Ov in the anatase 101 surface – the result is entirely method-dependent.

from these fundamental findings, we assisted Steve Cronin in two of his projects related to photocatalytic CO_2 reduction (Chem Mater 2015, Nano Lett 2015). These studies showed that the supporting oxide itself may easily bind small electrophilic molecules, filling the Ov hole on the oxide surface. When studying and designing surface-deposited cluster catalysts, it is thus important to take into account the possible co-reactivities of the support, and cluster-support interface. The implications of these findings remain to be seen in our future works.
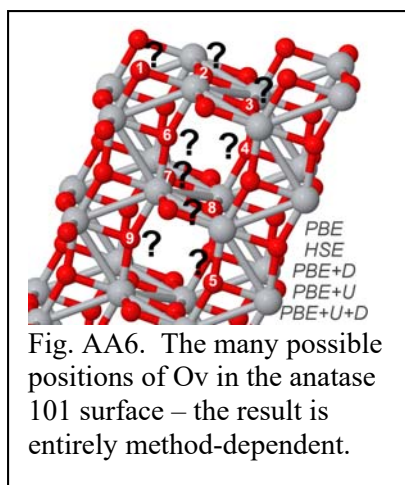
Archival publications, in print, in press, and submitted:

13. Ha, M.-A.; Alexandrova, A. N. *Oxygen Vacancies of Anatase 101: Extreme Sensitivity to the Density Functional Theory Method. J. Chem. Theor. Comput.* **2016**, *12*, 2889–2895.

12. Qiu, J.; Zeng, G.; Ha, M.-A.; Hou, B.; Mechlenburg, M.; Shi, H.; Alexandrova, A. N.; Cronin, S. B. *Microscopic Study of Atomic Layer Deposition of TiO_2 on GaAs and its Photocatalytic Application. Chem. Mater.* **2015**, *27*, 7977–7981.

11. Jimenez-Izal, E.; Alexandrova, A. N. *σ-Aromaticity in Polyhydride Complexes of Ir, Os, and Pt.Phys. Chem. Chem. Phys*., **Invited article for the special issue on aromaticity**, **2016**, *18*, 11644 –11652,

10. Qiu, J.; Zheng, G.; Ha, M.-A.; Ge, M.; Lin, Y.; Hettick, M.; Alexandrova, A. N.; Javey, A.; Cronin, S. B.* *Artificial Photosynthesis on TiO_2-Passivated InP Nanopillars. Nano Lett.* **2015***, 15*, 6177–6181.

9. Zhang, X.; Robinson, P. J.; Gantefoer, G.; Alexandrova, A. N.; Bowen, K. H. *Ph otoelectron Spectroscopic and Theoretical Study of the $[HPd(\eta^2-H_2]^-$ Cluster Anion. J. Chem. Phys.* **2015***, 143*, 094307.

8. Dadras, J.; Jimenez-Izal, E.; Alexandrova, A. N. *Alloying Pt Sub-Nano-Clusters with Boron: Sintering Preventative and Coke Antagonist? ACS Catal.* **2015**, *5*, 5719-5727.

7. Zhai, H.; Ha, M.-A.; Alexandrova, A. N. *AFFCK: Adaptive Force Field-Assisted ab initio Coalescent Kick Method for Global Minimum Search. J. Chem. Theor. Comput.* **2015**, *11*, 2385-2393.

6. Dadras, J.; Shen, L.; Alexandrova, A. N. *Computational Study of Pt-Zn Clusters on Stoichiometric MgO(100) and TiO_2(110): Dramatically Different Sintering Behavior. J. Phys. Chem. C* **2015**, *119*, 6047-6055.

5. Ha, M.-A.; Dadras, J.; Alexandrova, A. N. *Rutile-deposited PtPd clusters: a hypothesis about the special stability at 50/50 ratio. ACS Catal.* **2014**, *4*, 3570-3580. **Invited article for the special virtual issue on computational catalysis.**

4. Alexandrova, A. N.; Bouchard, L.-S. *Sub-Nano Clusters: the Last Frontier of Inorganic Chemistry. Adv. Chem. Phys.* **2015**, *156*, pp. 73-100. Eds.: S. A. Rice, A. R. Dinner, John Wiley & Sons Inc. Hoboken, NJ. ISBN: 978-1-118-94969-6. **Invited article.**

3. Shen, L.; Dadras, J.; Alexandrova, A. N. *Pure and Zn-Doped Pt Clusters Go Flat and Upright on MgO(100). Phys. Chem. Chem. Phys.* **2014**, *16*, 264366-26442. **Invited article. Journal Cover.**

2. Zhang, X.; Bowen, K. H.; Alexandrova, A. N. *The PtAl⁻ and PtAl₂⁻ Ions: Theoretical and Photoelectron Spectroscopic Characterization. J. Chem. Phys.* **2014**, *140*, 164316.

1. Zhang, X.; Liu, G.; Gantefoer, G.; Bowen, K. H.; Alexandrova, A. N. *PtZnH₅⁻, a σ-aromatic cluster. J. Phys. Chem. Lett.* **2014**, *5*, 1596-1601. **Highlighted in *Chemistry World*, UK.**

Discoveries, inventions, and patent disclosures: we discovered that B is a good dopant for surface-deposited Pt catalysts to prevent deactivation via coking and make dehydrogenation selective. This prediction was then texted experimentally and confirmed. No patent has been filed.

PI: Shiv N. Khanna

Address: Department of Physics, Virginia Commonwealth University, Richmond, VA 23284-2000.

Objectives: The overall goal of the BRI was to offer a microscopic understanding of the factors that control the activity of the catalysts for endothermic cooling of the hypersonic space vehicles with the ultimate objective of finding an optimal catalyst that could enhance the endothermic cracking of fuels along with minimizing the coking and poisoning of the catalysts. The theoretical work in Khanna group provided insight into some of the key issues and suggested new directions on how to reduce coking and the cost associated with catalysts. Our investigations proceeded in four directions following some earlier experimental findings and the work being conducted by the experimental colleagues in the present BRI. 1) We investigated the effect of embedding Pt_n clusters in alumina on the coking following earlier experiments that coating Pt surfaces with alumina could reduce coking and sintering. Our results showed that apart from coating, a proper embedding can substantially reduce the cocking and identified the physical mechanism behind this reduction. This important and novel finding may lead to an alternate approach to reduce coking that does not block active sites. 2) Experimental studies on catalysis usually proceed by XPS and UPS but there is no systematic approach to extract useful information from the experimental measurements. In close collaboration with experimental group of Anderson, we completed theoretical studies on the effect of O_2 and CO exposure on the Photoelectron Spectroscopy of size-selected Pd_n clusters supported on $TiO_2(110)$ to provide the microscopic insight into their experiments. This fundamental development will be useful beyond the current BRI. 3) Following experiments (Science 2014, 344 (6184), 616–619) that reported that a catalyst consisting of Fe sites embedded in a silica matrix can activate C–H bond in CH_4 without any coke formation for 60 hours, we carried out studies on how the catalytic properties of 3d transition metal atoms can be modified by linking them to Si or O sites on SiO_2 clusters. These studies offer strategy for identifying candidates with optimal electronic structure for maximizing C-H bond activation. 4) We completed studies of C-C bond activation in ethane by transition metal atoms and carbide molecules to open the pathway towards designing catalytic mimics for bond cracking. In the following we briefly outline our accomplishments in each of these areas.

Summary of Accomplishments:

1. **Embedding Pt_n Clusters in Alumina to Reduce Coking and Sintering:**

A strategy for dramatically increasing the stability of supported nanoparticles and to reduce coking is to overcoat the catalysts with alumina. Previous studies indicate that such an overcoating of metal nanoparticles reduced deactivation by coking and sintering at high temperatures (SCIENCE 335, (2012). However, overcoating may quench the active sites reducing activity, so we investigated an alternative strategy namely if embedding the clusters could also reduce coking while maintain activity. Towards this end, we investigated structure and activity of Pt_n clusters supported and embedded in α-alumina. Fig. 1 shows the geometry of the embedded clusters, the energy required to remove a Pt atom from the cluster, and the binding energy of the cluster for the case of supported and for embedded clusters. The energy to remove a single Pt atom is important for sintering mechanisms where single atoms migrate. Note that there is a significant increase in the removal energies of the cluster in going from supported to embedded clusters. This dramatic increase in the cluster binding energy demonstrates that the clusters will be much less likely to sinter, and are more likely to survive active catalyst conditions at high temperatures.
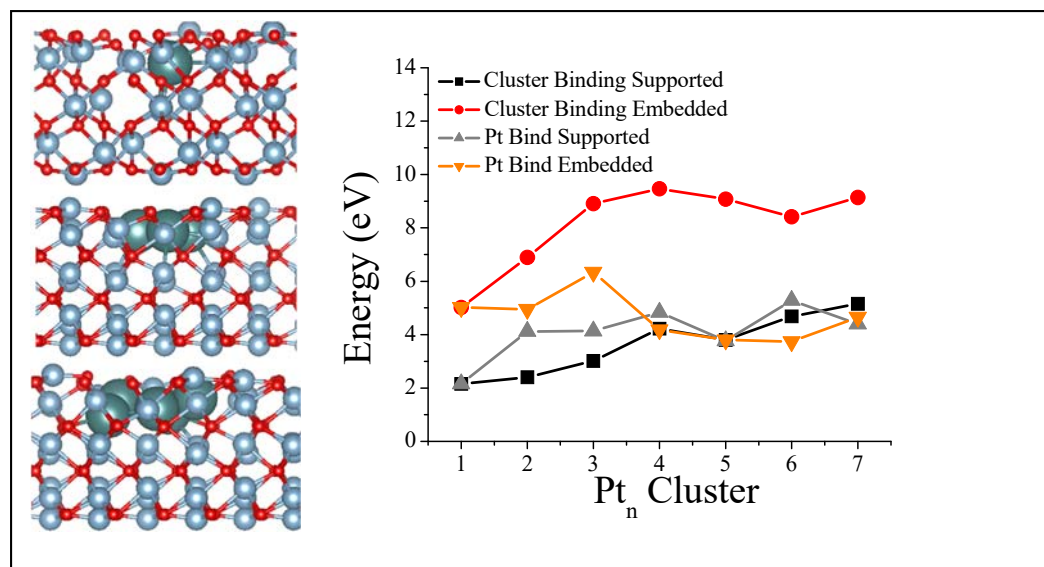
Figure 1. Left Panel. Model of embedded clusters. Right Panel. Binding of a Pt atom and clusters when supported on an Al_2O_3 surface and when embedded in the surface.

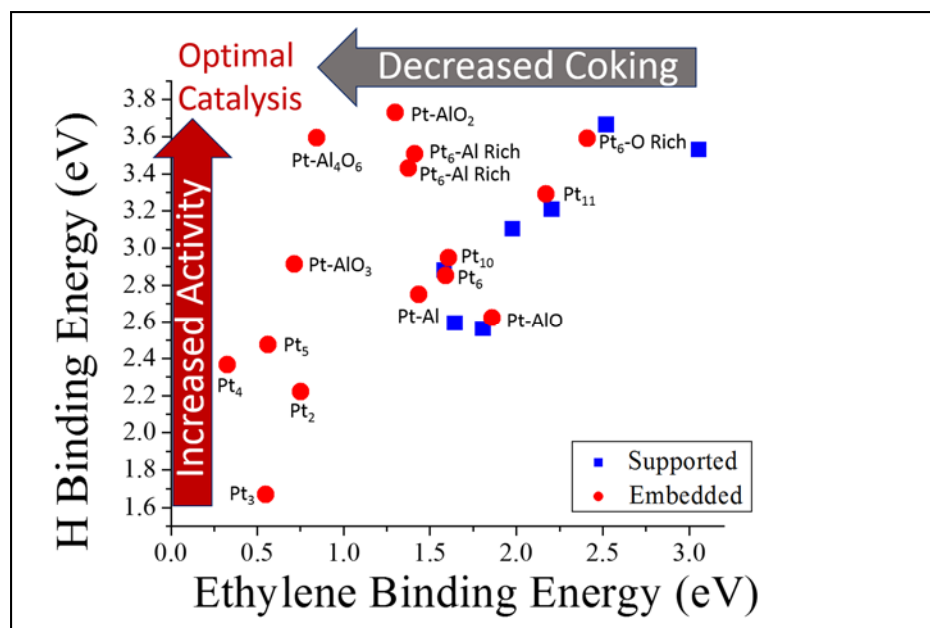

Figure 2. A comparison of the activity and coking parameters of Pt_n clusters supported on pristine Alumina(Blue Squares), and clusters embedded in alumina (red circles).

To understand the change in coking, we investigated the effects of charging on embedded clusters and determined its effect on the oxidation state of the coking and binding. Mechanistic studies on the coking process by Mavrikakis and co-workers show that the over-binding of ethylene to the catalyst is a strong indicator of whether coking will proceed or be inhibited. We have found that the oxidation state of the embedded species has a large effect on both the ethylene binding energies and the Hydrogen binding energies. The optimal catalysts should strongly bind Hydrogen for high activity, and bind ethylene weakly

2

to inhibit coking. Figure 2 shows a scattergram of these parameters for a number of clusters, and we find that the H binding energy and ethylene binding energies are strongly correlated for supported clusters; by changing the size of the cluster we can reduce activity and coking, or increase activity and coking, but are unable to identify more optimal catalysts that are coking resistant and active. For embedded clusters, we find that supported clusters that are partially reduced, with a smaller number of O atoms lining the vacancy, the cluster becomes negatively charged enough to reduce coking, while still having high activity. The least effective of the embedded clusters are just as effective as the platinum clusters on pristine alumina, while still exhibiting drastically reduced sintering. We find that partially embedding clusters not only reduces sintering, but may also enhance activity and reduce coking.

2. **Effect of O_2 and CO exposure on the Photoelectron Spectroscopy of Size-selected Pd_n Clusters Supported on $TiO_2(110)$.**

X-ray and Ultraviolet Photoelectron Spectroscopy, XPS and UPS, are powerful tools for determining the oxidation state of atoms and the valence electronic structure of a sample. The sample of interest is exposed to ionizing radiation and electron binding energies are determined from the kinetic energy distribution of the ejected photoelectrons. Experimental energies are the differences between the energies of the *N* electron initial state of the system and the *N-1* electron final state. If the goal is to relate experimental measurements such as adsorbate-induced shifts in binding energies to theoretical results for adsorbate effects on orbital energies, and thus learn about adsorbate bonding, it is necessary to differentiate between initial state and final state effects on the binding energies. We have collaborated with Anderson group to demonstrate that these effects can be important for interpreting the experimental data.

The joint studies focused on an investigation of the ultraviolet and X-ray photoelectron spectra of Pd_n clusters with adsorbed O_2 and CO. UPS of size-selected Pd_n clusters supported on TiO_2 shows a decrease in density of states in the TiO_2 gap after the absorption of CO, while O_2 does not result in a decrease in density. Oxygen is more electron withdrawing than CO, so the Pd_n clusters should become more positively charged when exposed to O_2 than CO. More positively charged clusters are expected to have
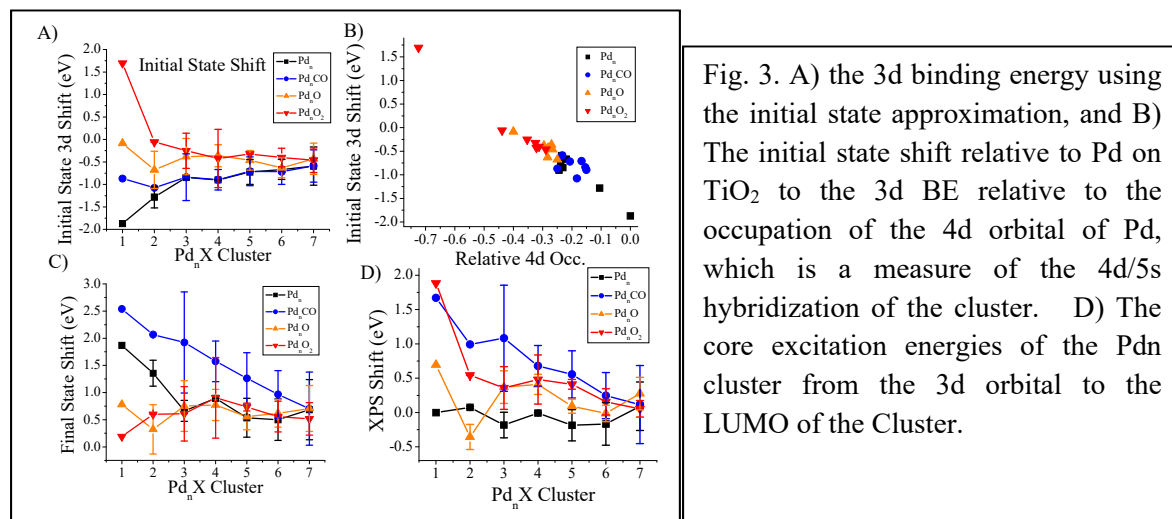

Fig. 3. A) the 3d binding energy using the initial state approximation, and B) The initial state shift relative to Pd on TiO_2 to the 3d BE relative to the occupation of the 4d orbital of Pd, which is a measure of the 4d/5s hybridization of the cluster. D) The core excitation energies of the Pdn cluster from the 3d orbital to the LUMO of the Cluster.

larger electron binding energies, thus the observed shifts in the UPS spectra are at **odds with conventional wisdom**. Our theoretical studies reveal that the bonding of both CO molecules and O atoms to the Pd

3

clusters results in a decrease in the density of states in the TiO_2 gap, however, O atom binding on top of the clusters also results in significant final state stabilization, restoring the density of states in the TiO_2 gap in the UPS spectrum. We also find that *4d-5s* hybridization plays a critical role in the initial state energies in X-ray photoelectron spectroscopy, and evaluate two methods for determining the final state shift via periodic calculations.

Fig. 3 shows our studies that relate to XPS measurements in Anderson's group. Fig. 3A) shows the initial state shift and how it correlates with the occupation of the 4d orbitals. Fig. 3C) shows the final state shift and Fig. 3 D) shows how the observed XPS shift depends on a combination of the initial and final state shifts. We have found the initial state XPS shift does not depends on the oxidation state of the Pd cluster, but almost exclusively on the occupation of the 4d orbitals of Pd. This means that the initial state shift provides information about the 4d-5s hybridization of the Pd cluster which plays a role in the activity of a given cluster. This relationship is shown in Figure 3. The 4d orbital controls the XPS shift because the 4d orbitals are much more localized than the 5s orbitals so the 4d orbital screens the core electrons much more effectively than the delocalized 5s orbital. Similar results are found for the XPS shift in Pt on alumina. A similar microscopic viewpoint is needed to understand the observed UPS spectra. Fig. 4 shows the density of electronic states when a Pd_4 cluster is covered with successive CO
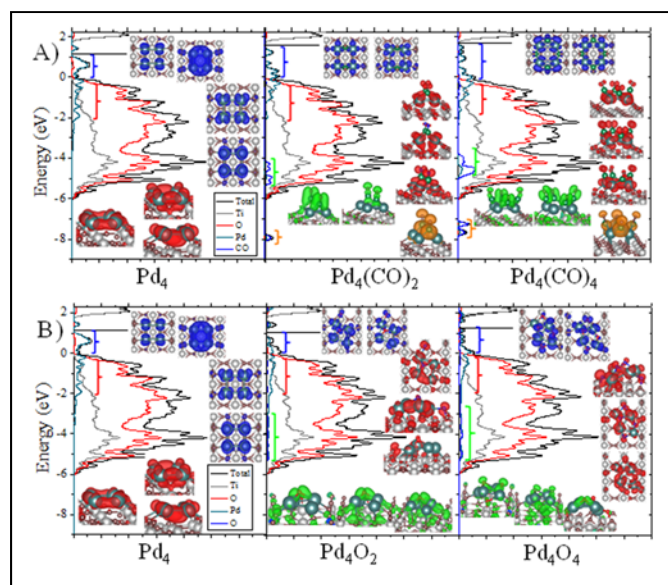

Fig. 4 A) The density of states for Pd_4, $Pd_4(CO)_2$, and $Pd_4(CO)_4$. Representative molecular orbitals in the blue range which lies in the band gap of TiO_2, the Red range which lies just below the valence band, the green range which lies deep in the valence band, and the orange range which is a C-O bonding orbital. B) The density of states for Pd_4, Pd_4O_2, and Pd_4O_4. Representative molecular orbitals in the blue range which lies in the band gap of TiO_2, the Red range which lies just below the valence band, the green range which are deep bonding orbitals.

and O_2 molecules and how the various orbitals lie in the band gap of the TiO_2. In this case, the final state shifts along with the Vacuum level shifts are needed to understand the experimental data. This is shown in Fig. 5 that displays the two contributions. We have found that the initial state shifts are driven by the dipole moment on the surface of the cluster which shifts the work function of the surface. We also developed a method to correct for the coverage of the cluster in order to determine the shift in the work function as a function of size.
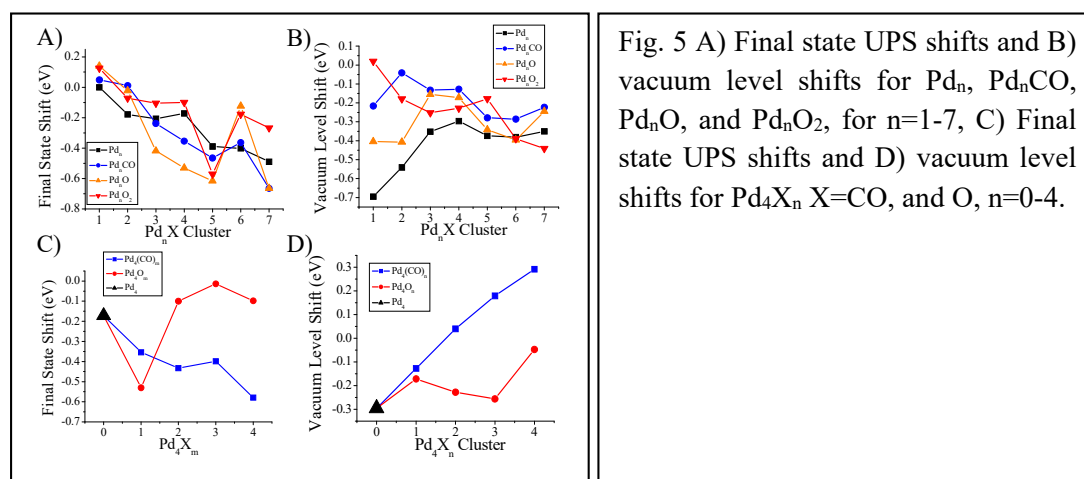
Fig. 5 A) Final state UPS shifts and B) vacuum level shifts for Pd_n, Pd_nCO, Pd_nO, and Pd_nO_2, for n=1-7, C) Final state UPS shifts and D) vacuum level shifts for Pd_4X_n X=CO, and O, n=0-4.

It is important to highlight that these are the first studies that show how the observed UPS and XPS relate to the electronic structure and how a microscopic understanding of various factors is needed to understand the observed shifts.

3. **Methane Activation by Controlling s- and d-states in Iron-based Single Site Catalysts**

In a recent experimental finding Guo et al. (Science 2014, 344 (6184), 616–619)) synthesized a catalyst consisting of Fe sites embedded in a silica matrix. They found that such sites activate C–H bond in CH_4, even in the absence of oxidants, generating methyl radicals that desorb from the surface to generate ethylene, benzene etc. The absence of neighboring Fe sites prevents formation of coke and the catalyst showed a methane conversation efficiency of 48% and a total hydrocarbon efficiency of 99%. Furthermore, the catalyst is stable and showed no deactivation even after 60 hours. These are remarkable findings and we undertook theoretical investigations to uncover how, by combining group–IV elements such as C or Si
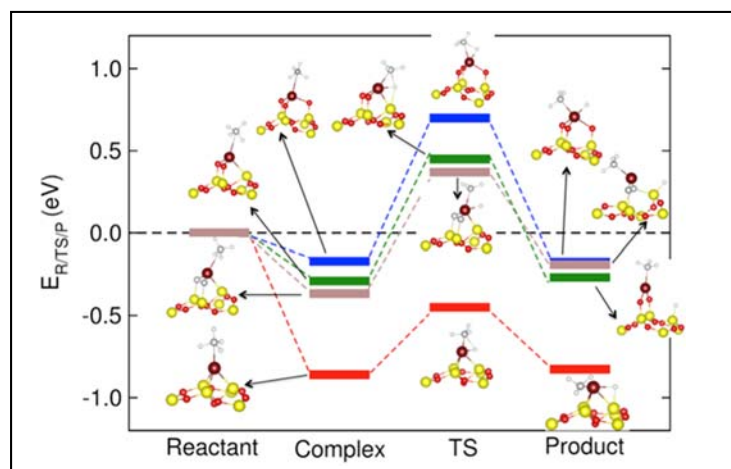
Figure 6. Minimum energy reaction pathways for methane activation for 3O, 2C, 2O and 3Si cases on silica clusters, shown as blue, brown, green and red lines, respectively. $E_{R/TS/P}$ is the energy difference of reaction state with respect to their reactants .

to Fe, one can lower the transition state energy for C–H bond cleavage in methane. To develop a microscopic understanding of the factors governing the reactivity we investigated how the reactivity of a Fe site changes as it is linked to different atoms on a cluster model of the SiO_2 surface. The reaction of

5

choice was the cleavage of the first C-H bond in methane. Our objective was to investigate how the microscopic parameters such as the position and filling of the d- and s-states and location of selected electronic levels affect the reaction barriers. To this end, we carried out a detailed examination of the molecular orbitals involved in the stabilization of the transition state (TS) and how the linking of the Fe sites to supports may allow for easier C-H bond activation. We deposited an Iron atom on a Si_7O_7 and Si_7O_{10} model cluster. The Fe atom can be linked to the substrate in several ways; it can be directly linked to 3 Si sites (3Si), two of the oxygen atoms can be replaced by carbon atoms while one oxygen atom is removed to form a 2 C and a Si site (2C) as suggested by Guo et al., to a Si and 2O sites (2O), or to three O sites (3O). A detailed investigation of the electronic structure indicated that the reactivity is mainly governed by the position of 3d-states while the s-states remain empty for supported Fe. In contrast to supported cases, for free atoms, both 3d-states the position of filling of 4s-states play a key role for exhibiting different trends in reactivity. A molecular orbital analysis revealed that the 4s orbital plays a key role in the transition state energy because an occupied 4s orbital at the transition state forms an antibonding orbital with the highest occupied molecular orbital of methane with a stretched C–H bond, thereby increasing the transition state energy. The 4s orbital occupation also reduces the methane binding energy. Two 3d orbitals stabilize the transition state, one that is hybridized with the Fe 4s orbital and interacts with the highest occupied molecular orbital of the activated methane, and a second that stabilizes the lowest unoccupied molecular orbital of methane. Through these interactions the d band also plays a role in affecting the binding of methane and in determining the reaction barrier that reveals an optimal location of the center of the d-states. Such a molecular orbital view of methane activation offers a strategy for identifying candidates with the optimal 4s and 3d orbital energies for affecting C–H bond activation using ligated non–precious metals.

4. Microscopic Insight into C-C Bond Activation in Ethane by Transition Metal atoms and Carbide molecules:

It was almost four decades ago that Levy and Boudart suggested that the addition of carbon to transition elements Mo or W can impart those with catalytic properties typical of noble elements Pt or Pd. Later works by other researchers also confirmed that tungsten and molybdenum carbides exhibit enhanced catalytic activity for reactions such as benzene hydrogenation, ammonia synthesis, hydrodehalogenation and desulfurization. In fact, molybdenum carbide is extensively used for hydrogenation of aromatics instead of Pt in petroleum industry. Following these earlier studies, Castleman and co-workers undertook experimental studies on the reactivity and negative ion photodetachment spectra that can probe the energy levels. Their studies on the reactivity of Pd^+ and ZrO^+ with ethane and propane indeed led to similar reaction products with breaking of the C-C bond as the primary reaction pathway. In another experiment, Castleman and co-workers used negative ion photodetachment spectra and velocity map imaging to probe the electronic stares for WC^- and Pt^- and found that both pairs have similar photo-detachment spectra indicating similar electronic valence spectrum. These studies have suggested that the addition of Carbon to Mo and W can offer them catalytic properties typical of noble metals Pd and Pt where C sp-electrons modify the effective valence of Mo and W. These are important findings that could offer ways to replace expensive catalysts by cheaper mimics.

To investigate these analogies, we undertook first principles theoretical studies on the C-C bond activation of ethane by bare 4d transition metal (TM) atoms and TMC molecules. Our objective was to develop a conceptual model underlying such changes. Our findings suggest that addition of carbon to transition metal atoms leads to a reduction/increase in the activation barrier depending on the metal and that there is indeed

6

a pronounced reduction for Mo as previously observed in experiments. A critical examination of molecular orbitals, however, shows that the changes in reactivity cannot be linked to filling of d-states implicit in the
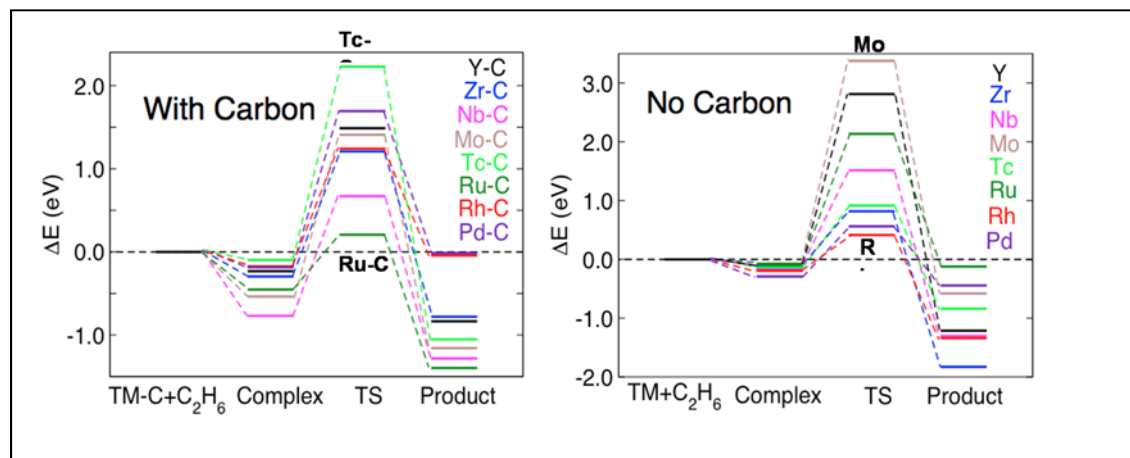

Fig. 7. The minimum energy reaction pathways for C-C bond cracking of TM and TM-C+ethane complexes. The reference energy is the energy of the separated species (TM-C and ethane) with minimum energy

effective valence model. The reactivity is governed by the location and filling of the s- and d- orbitals with each controlling different facets of reactivity. While the s-state control the initial binding of ethane, needed to stabilize the molecule at the reaction site, the location of dz^2 orbital controls the reaction barrier that along with initial binding controls the reaction activation energy. These findings not only offer an understanding of how the catalysis at the microscopic scale is different from bulk but also on how the catalytic properties can be modified by controlling s- and d-states.

In addition to the directions outlined above, we have also participated in applications of some of the findings into other areas. For example, Palladium-catalyzed Suzuki-Miyaura cross-coupling reactions are important in pharmaceutical applications due to its mild reaction conditions and broad application across a wide range of functionalized substituents. In a collaborative effort with experimental groups we recently demonstrated that a catalyst consisting of palladium clusters supported on reduced graphene not only minimizes leaching but also offers superior catalytic activity with extremely high turnover frequencies and remarkable recyclability. Theoretical investigations reveal that while the vacancy/void sites strongly bind the clusters thereby reducing leaching, the support also serves as a reservoir of charge that causes the reaction barriers to be even lower than those for homogeneous catalysts, explaining why such catalysts are active enough for continuous flow processes. Through state of art experiments involving a three-phase test, we unambiguously demonstrate that the catalyst operates in a heterogeneous mode. These findings are being reported in a manuscript that is under consideration in ACS-catalysis.

List of Publications:

1.   "Effect of N- and P-Type Doping on the Oxygen-Binding Energy and Oxygen Spillover of Supported Palladium Clusters". Reber, A. C. and Khanna, S. N.. *J. Phys. Chem. C* **118** 20306-20313 (2014).

2.   "Reactivity of Silver Clusters Anions with Ethanethiol".   Luo, Z.; Gamboa, G. U.; Jia, M.; Reber, A. C.; Khanna, S. N.; and Castleman, Jr., A. W.. *J. Phys. Chem A* **118,** 8345–8350 (2014).

3.   "Initial and Final State Effects in the Ultraviolet and X-Ray Photoelectron Spectroscopy (UPS and XPS) of Size-Selected Pd_n Clusters Supported on $TiO_2(110)$". Roberts, F.S.; Anderson, S. L.; Reber, A. C.; and Khanna, S. N. *J. Phys. Chem. C* **119**, 6033-6046 (2015).

4.   "Conceptual Basis for Understanding C-C Bond Activation in Ethane by Transition Metal Carbides". Sahoo, S.; Reber, A. C.; and Khanna, S. N., *J. Phys. Chem. A* **119**, 12855-12861 (2015).

5.   "The Effect of O_2 and CO Exposure on the Photoelectron Spectroscopy of Size-selected Pd_n Clusters Supported on $TiO_2(110)$". Reber, A. C.; Khanna, S.N.; Roberts,F. S.; and Anderson, S. L., *J. Phys. Chem. C* **120**, pp 2126–2138 (2016)

6.   "Effect of location and filling of d-states on methane activation in single site Fe-Based Catalysts". Sahoo, S.; Reber, A. C.; and Khanna, S. N., *Chemical Physics Letters*, (in press).

7.   "Charge Exchange Enhances Heterogeneous Cross-Coupling Catalysis in Small Palladium Clusters on Reduced Graphene". Y. Yang, Y.; Castanoa, C. E.; Gupton, B. F.; Reber, A. C.; and Khanna, S. N. (under consideration, ACS Catalysis).

8.   "Structure and Activity of Pt_n clusters supported on and embedded in α-Al_2O_3", Reber, A. C. and Khanna, S. N., (under preparation).

Personnel Supported:

S. N. Khanna	**(PI)**
A. C. Reber	**(Post-Doc)**
S. Sahoo	**(Post- Doc)**
C. J. Grover	**(M.S. graduate student)**
W. H. Blades	**(M.S. Graduate Student)**
M. D. Ference	**(Undergraduate Student)**
Thibault V. Robert	**(Undergraduate Student)**

Final Report of AFOSR Project Grant No. FA9550-12-1-0481

Manos Mavrikakis and James A. Dumesic

University of Wisconsin-Madison

(August 2016)

Objective: To identify improved catalysts for endothermic cooling with minimized coke formation in jet fuel with a combined theoretical and experimental approach.

Methodology Developed: Density functional theory (DFT) calculations, catalyst synthesis and characterization, reaction kinetics experiments, microkinetic modeling
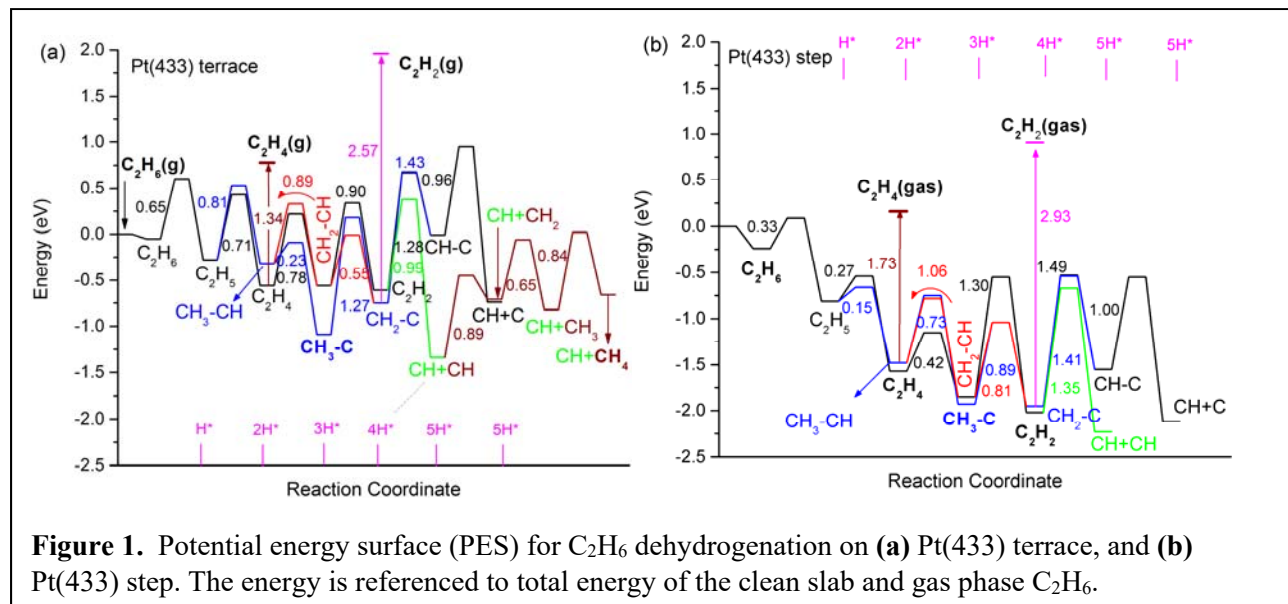
Accomplishments: In the scope of this project, we

- Conducted DFT calculations for C_2H_6 dehydrogenation energetics and reaction network over pristine and alumina decorated Pt catalysts. In parallel, catalytic activity and coke formation patterns of $Pt/\gamma\text{-}Al_2O_3$ and ALD overcoated $Pt/\gamma\text{-}Al_2O_3$ catalysts were investigated experimentally.

- Performed DFT calculations on terrace and stepped Pt_3Sn alloy surfaces to derive energetics of ethane dehydrogenation reaction network.

- Identified key parameters that can be calculated by DFT to point towards promising bimetallic Pt-X alloys that catalyze C_2H_6 dehydrogenation with minimized coke formation.

- Examined the promotional effect of Sn for enhanced C_2H_4 formation from C_2H_6 on Pt and Pt-Sn catalysts supported on SiO_2, $\gamma\text{-}Al_2O_3$ and H-ZSM-5 with reaction kinetic studies.

- Combined DFT calculated parameters and experimental data to develop a comprehensive microkinetic model elucidating the role of surface coverage under reaction conditions.

- Studied the effects of catalyst composition, support structure, feed composition and reaction time on coke formation and deposition on Pt-based catalysts.

- Calculated C_2H_6 dehydrogenation energetics over terrace and stepped surfaces of Pt_3Pb and Pt_3Zn alloys and performed the relevant reaction kinetics experiments.

- Performed preliminary gas phase i-C_4 species energy calculations to start investigating the effect of fuel structure on the reactivity of the catalyst.

- Collaborated with UTRC and ANL with preparing Pt-based catalyst samples and Heat Exchanger Rig test and XAS experiments.

- In the following sections, we provide additional information on the outcomes of those main research directions.
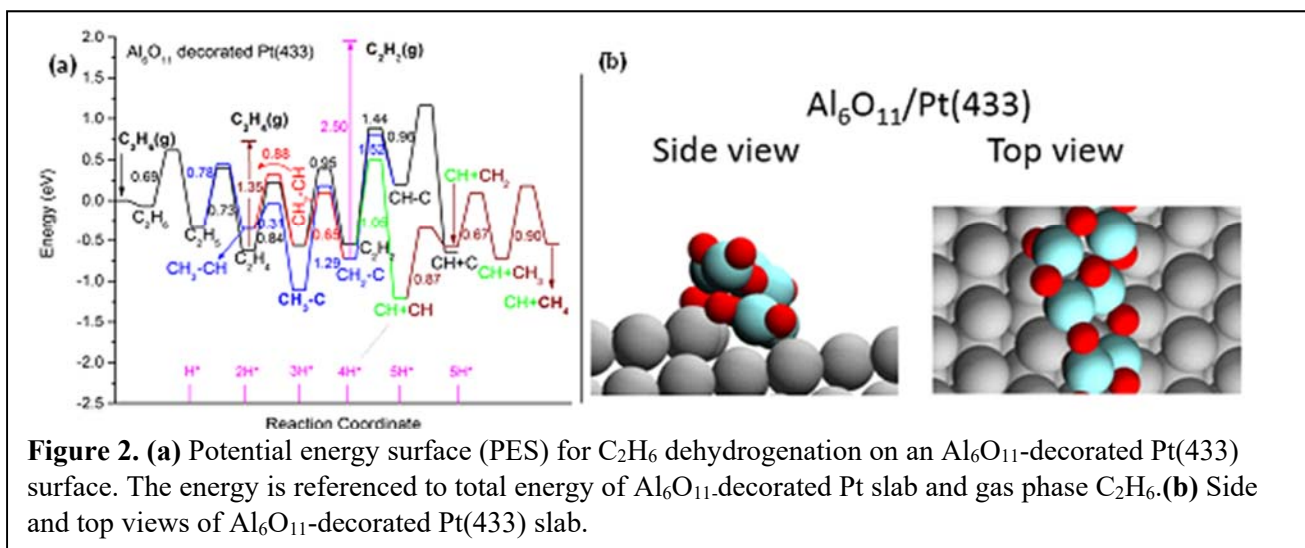
A. Ethane dehydrogenation on pristine and alumina over-coated Pt

Using planewave DFT methods, we calculated the detailed energetics (thermochemistry and activation energy barriers) of the reaction network for C_2H_6 dehydrogenation on pristine and alumina-decorated Pt(433) stepped surfaces. Shown in **Figure 1** are the calculated potential energy surfaces (PES) for C_2H_6 dehydrogenation on the terrace and step of Pt(433). As seen in **Figure 1(a)**, on the Pt(433) terrace, C_2H_6 can be dehydrogenated to C_2H_4, whereas further deep dehydrogenation reactions to C_2H_2 and CH_x fragments are difficult. In contrast to this result, on the step itself **Figure 1(b)**, the dehydrogenation is significantly accelerated due to the availability of under-coordinated step sites. The facile deep dehydrogenation on the step leads to accumulation of coke precursors, thereby poisoning/de-activation of the catalysts.

Figure 1. Potential energy surface (PES) for C_2H_6 dehydrogenation on **(a)** Pt(433) terrace, and **(b)** Pt(433) step. The energy is referenced to total energy of the clean slab and gas phase C_2H_6.

One strategy for minimizing coke formation might be to block the highly reactive step sites prior to exposing the catalyst to reactants. Recent studies have demonstrated that alumina is an excellent over-coating material. We thus studied C_2H_6 dehydrogenation on an alumina-decorated Pt stepped surface, where the highly reactive steps sites are covered by a thin alumina film. Shown in **Figure 2a** is the calculated potential energy surface for C_2H_6 dehydrogenation on Pt(433) terrace with an Al_6O_{11} decoration at the step edge, together with the modelled slab (**Figure 2b**). By comparing Figure 2a with Figure 1(a), we conclude that the presence of alumina decoration on the step renders the stepped Pt surface essentially identical to the flat Pt terrace surface suggesting that AlO_x-overcoated Pt might be a promising catalyst for the endothermic cooling application.

2

Figure 2. (a) Potential energy surface (PES) for C_2H_6 dehydrogenation on an Al_6O_{11}-decorated Pt(433) surface. The energy is referenced to total energy of Al_6O_{11} decorated Pt slab and gas phase C_2H_6. **(b)** Side and top views of Al_6O_{11}-decorated Pt(433) slab.

In parallel to our DFT work, we performed reaction kinetics experiments for C_2H_6 dehydrogenation on different Pt based catalysts. Catalytic dehydrogenation of C_2H_6 was carried out at 600°C for 2 hrs under atmospheric pressure on non-overcoated and alumina-overcoated Pt/γ-Al_2O_3 catalysts with 1 wt% Pt loading. The atomic layer deposition (ALD) technique, which gives highly conformal coatings, was used to deposit 2, 5, and 10 cycles of alumina overcoat on the parent Pt/γ-Al_2O_3 catalyst. CO chemisorption on these samples confirmed the reduction in the number of accessible Pt sites with the deposition of successive alumina-cycles/layers. For the dehydrogenation experiments, the total gas flow rate was maintained at 200 cm^3(STP)/min with 12.5 Torr C_2H_6 partial pressure, and He was used as the balance carrier gas. For the subsequent catalyst-regenerability study, the catalyst bed was calcined under air at 400°C for 1 hr and then reduced at 500°C in flowing H_2 before starting the subsequent dehydrogenation experiments. This reduction-reaction-regeneration cycle was repeated three times, and it was observed that both the non-overcoated and the overcoated catalysts are regenerable, i.e., there was no irreversible deactivation. This behavior is an important aspect for the application of endothermic cooling as it greatly reduces catalyst operating cost. The initial and long-term turnover frequency (TOF) for C_2H_4 on the 10cALD/Pt/γ-Al_2O_3 were higher than those on the non-overcoated Pt/γ-Al_2O_3. This enhancement substantiated the insights derived from our theoretical calculations for the effect of alumina decoration of pristine Pt surfaces. Thermogravimetric analysis was performed on post-reaction catalysts collected prior to the calcination step to quantify the amount of coke deposited. The number of accessible Pt sites of the fresh catalysts determined by CO chemisorption and the amount of coke deposited per gram of the spent catalysts are listed in **Table 1**; Catalysts overcoated with higher number of alumina-cycles exhibited less amount of carbon deposition, in accordance with its experimentally observed enhanced activity and stability.

3

Table 1: CO saturation uptakes of the fresh catalysts and carbon deposition amounts on spent catalysts
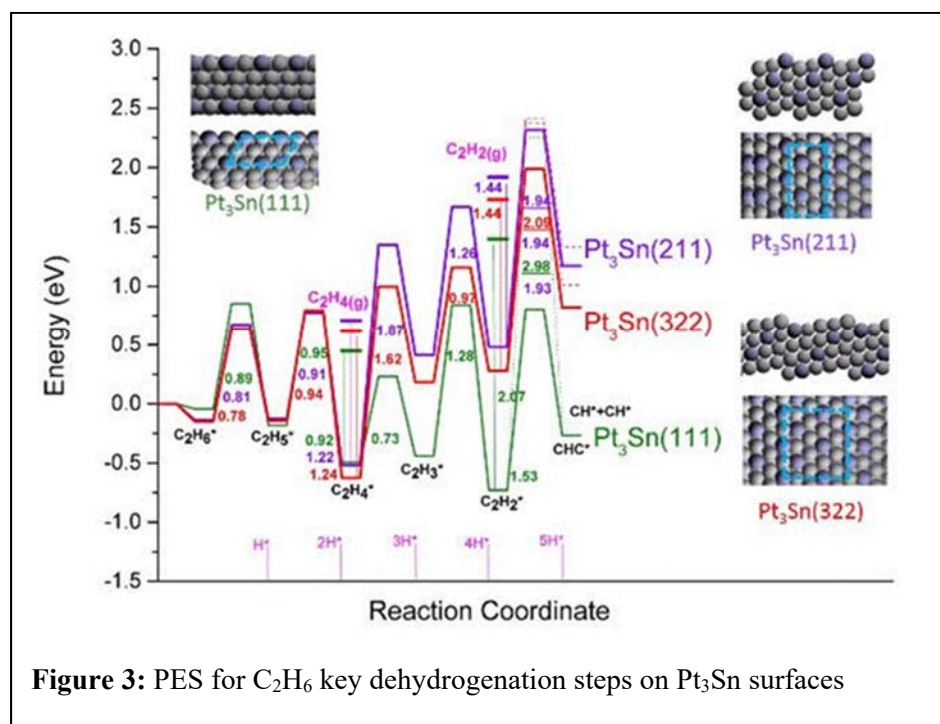
Catalyst	Pt Sites (μmol sites/gcat)	Carbon Deposition (mmol C/gcat)
Non-overcoated Pt/γ-Al$_2$O$_3$	29	3.36
2cALD/Pt/γ-Al$_2$O$_3$	19	1.75
5cALD/Pt/γ-Al$_2$O$_3$	10	1.92
10cALD/Pt/γ-Al$_2$O$_3$	3	0.87

B. Ethane dehydrogenation on Pt-Sn alloys

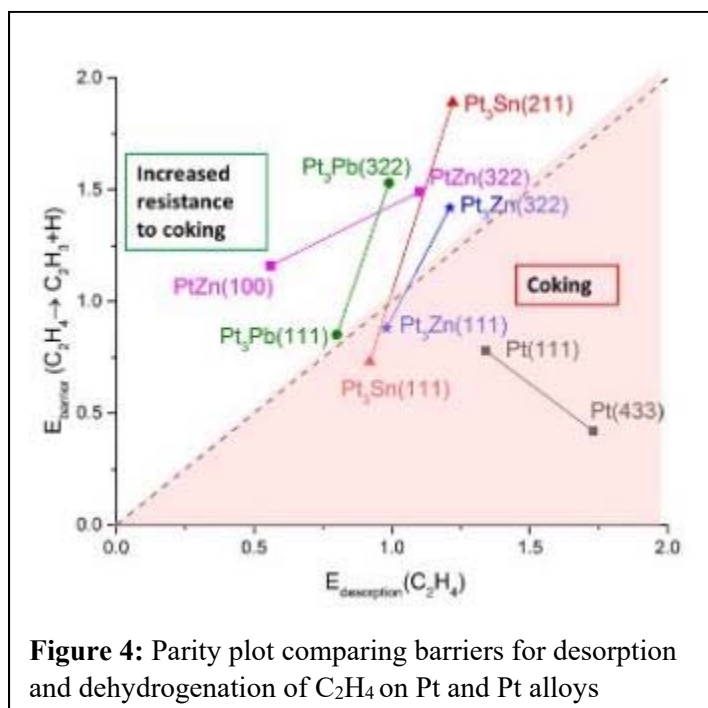Another approach to mitigate coke formation is to use bimetallic catalysts which can catalyze C$_2$H$_6$ dehydrogenation to C$_2$H$_4$ but *not* catalyze deep dehydrogenation, thereby reducing coke formation. As we will discuss in the next section, oxophilic metals that can lower the d-band center of Pt are good candidates for alloying, therefore, we chose PtSn alloy as our model system. The reaction network of C$_2$H$_6$ dehydrogenation on a Pt$_3$Sn(111) terrace and a stepped Pt$_3$Sn(211) surface was analyzed with DFT, similarly to the analysis of pristine Pt surfaces presented above. Our results show that on both terrace and step sites, Sn alloying weakens the binding of intermediate species and facilitates C$_2$H$_4$ desorption. It was observed that, desorption of C$_2$H$_4$ was easier on the terrace of Pt$_3$Sn than on the terrace of pristine Pt. In addition, compared to the step sites of pristine Pt, step sites of Pt$_3$Sn were less reactive, particularly for deep dehydrogenation, consequently, reducing formation of coke precursors and coke deposition on the catalyst surface. To gain more insight on the activity of this type of site, a second stepped Pt$_3$Sn surface, namely (322), was also modeled and the energetics of C$_2$H$_6$ dehydrogenation on that surface was calculated. This stepped surface with a wider terrace length and lower coverage yielded similar energetics and posed higher energy barriers for dehydrogenation of C$_2$H$_4$ compared to the Pt$_3$Sn terrace sites and steps of pristine Pt. A comparison of the energetics of key dehydrogenation steps on three Pt$_3$Sn surfaces is shown in **Figure 3**.

C. Identifying improved bimetallic catalysts for ethane dehydrogenation

To identify improved catalysts for C$_2$H$_6$ dehydrogenation, we considered a number of Pt-X bimetallic alloys, using DFT and selecting criteria such as: (1) modest binding of C$_2$H$_4$, (2) difficult C—C cleavage (to suppress hydrogenolysis), and (3) the existence of stable alloy phases at operating conditions. An effective catalyst is expected to bind C$_2$H$_4$ modestly, because a weak binding of C$_2$H$_4$ would mean that C$_2$H$_6$ is difficult to activate on that catalyst, whereas a strong C$_2$H$_4$ binding would indicate a tendency of

4

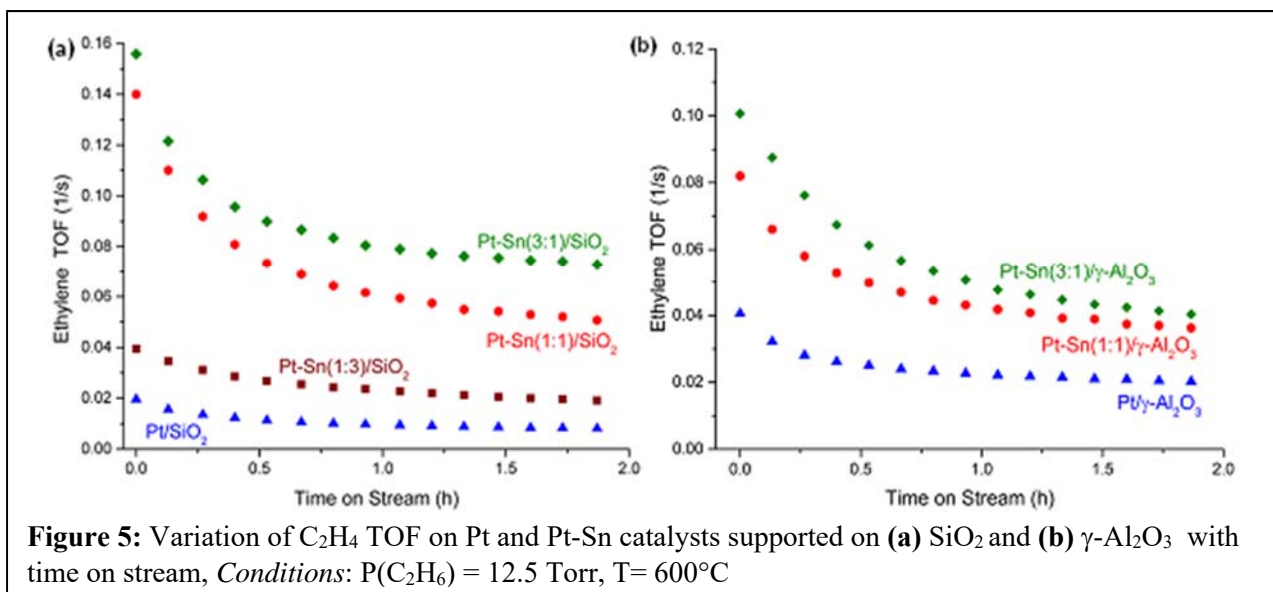**Figure 3:** PES for C_2H_6 key dehydrogenation steps on Pt_3Sn surfaces

that catalyst to form coke. Calculating the energetics of the entire reaction network for C_2H_6 dehydrogenation on these bimetallic surfaces of interest requires an enormous amount of work. Instead, we selectively calculated the energetics of three early dehydrogenation steps (i.e., from C_2H_6 to C_2H_5, from C_2H_5 to C_2H_4, and from C_2H_4 to vinyl (C_2H_3)), to identify the catalysts which can catalyze the hydrogenation from C_2H_6 to C_2H_4, but not catalyze further dehydrogenation of C_2H_4 to C_2H_3 (toward coke precursors). We suggested that the barrier of a promising catalyst for C_2H_4 desorption should be less than the barrier for its dehydrogenation to C_2H_3. To visualize the comparison of the selected bimetallic systems based on these criteria, a parity plot is shown in **Figure 4.** Points above the diagonal line correspond to bimetallic surfaces with increased resistance to coking, and include Pt_3Sn step sites, as discussed above. Therefore, the application of this set of criteria based on C_2H_4 energetics strongly suggested that bimetallic alloys Pt_3Zn and $PtZn$ (and possibly Pt_3Pb) are promising, potentially improved catalysts for C_2H_6 dehydrogenation with minimized coke formation.
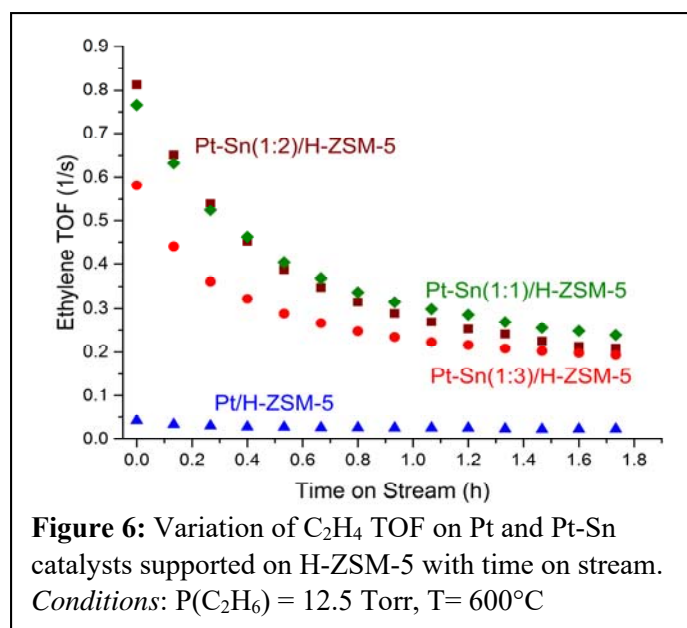

Figure 4: Parity plot comparing barriers for desorption and dehydrogenation of C_2H_4 on Pt and Pt alloys

5

D. Kinetic studies and characterization on Pt and Pt-Sn catalysts with different supports

To probe the promotional effect of Sn on the activity of Pt based catalysts, Pt-Sn catalysts were synthesized with varying Pt-Sn ratios on SiO_2, γ-Al_2O_3 and H-ZSM-5 (SiO_2:Al_2O_3 = 280) supports. 3 wt% Pt/SiO_2 and 6 wt% Pt/γ-Al_2O_3 catalysts were prepared by ion exchange and incipient wetness impregnation methods respectively. Sn was added to the monometallic catalysts by evaporative impregnation at Pt:Sn atomic ratios of 3:1, 1:1, and 1:3. Reaction kinetics experiments were carried out at 600°C, 1 atm with 200 cm^3 (STP)/min total gas flowrate. The feed was composed of 12.5 Torr C_2H_6/balance He. C_2H_4 TOF, normalized to total exposed Pt sites, as determined by CO chemisorption at 25°C, was tracked for 2 hrs. Variation of C_2H_4 TOF with respect to time on stream (TOS) on SiO_2 and γ-Al_2O_3 supported catalysts is shown in **Figure 5** . For both supports, addition of Sn provided higher initial and steady-state activity for C_2H_6 dehydrogenation. Following, Pt and Pt-Sn catalysts were prepared using a zeolite support, H-ZSM-5
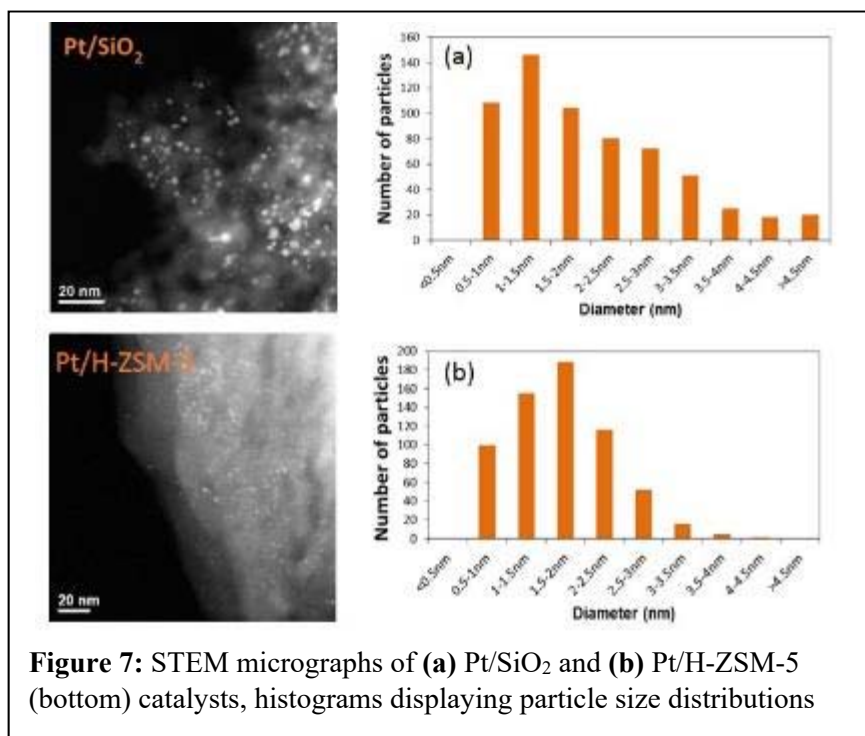

Figure 5: Variation of C_2H_4 TOF on Pt and Pt-Sn catalysts supported on **(a)** SiO_2 and **(b)** γ-Al_2O_3 with time on stream, *Conditions*: P(C_2H_6) = 12.5 Torr, T= 600°C

with SiO_2:Al_2O_3 ratio of 280. Pt loading of these catalysts were 0.58 wt% Pt. Similar to the SiO_2 and γ-Al_2O_3 supported catalysts, Sn addition to the Pt-only catalyst led to a significant promotion in C_2H_4 TOF values. **Figure 6** displays the variation of C_2H_4 TOF with TOS for the Pt, Pt-Sn(1:1), Pt-Sn(1:2), and Pt-Sn(1:3) catalysts supported on H-ZSM-5. The steady-state activity of the catalysts was not significantly dependent on the composition, however, it was visible that the Pt-Sn(1:1)/H-ZSM-5 and Pt-Sn(1:2)/H-ZSM-5 governed the highest initial activities for C_2H_6 dehydrogenation reaction. Compared to SiO_2 and γ-Al_2O_3 supported catalysts, C_2H_4 TOF values were enhanced by approximately 5 times on the PtSn/H-ZSM-5 catalysts, particularly in the earlier stages of the reaction. Considering the DFT calculations that predicted

6

Figure 6: Variation of C_2H_4 TOF on Pt and Pt-Sn catalysts supported on H-ZSM-5 with time on stream. *Conditions*: $P(C_2H_6)$ = 12.5 Torr, T= 600°C

higher activity for stepped facets of Pt_3Sn surfaces, which would represent small nanoparticles, highly active H-ZSM-5 supported catalysts were hypothesized to have particles with smaller size. Scanning transmission electron microscopy (STEM) was employed to improve our understanding of dispersion and particle size distribution of SiO_2 and H-ZSM-5 supported catalysts. STEM micrographs of fresh Pt/SiO_2 and Pt/H-ZSM-5 catalysts are shown in **Figure 7**. The Pt/SiO_2 catalyst with 3 wt% Pt loading had an average particle size of 1.96 nm and the particle size distribution histogram showed that a significant number of the 625 analyzed particles were larger than 3 nm in size. The Pt/H-ZSM-5 catalyst with 0.58 wt% Pt loading had an average particle size of 1.80 nm. The histogram for particle size distribution revealed that this catalyst has much less number of the

Figure 7: STEM micrographs of **(a)** Pt/SiO_2 and **(b)** Pt/H-ZSM-5 (bottom) catalysts, histograms displaying particle size distributions
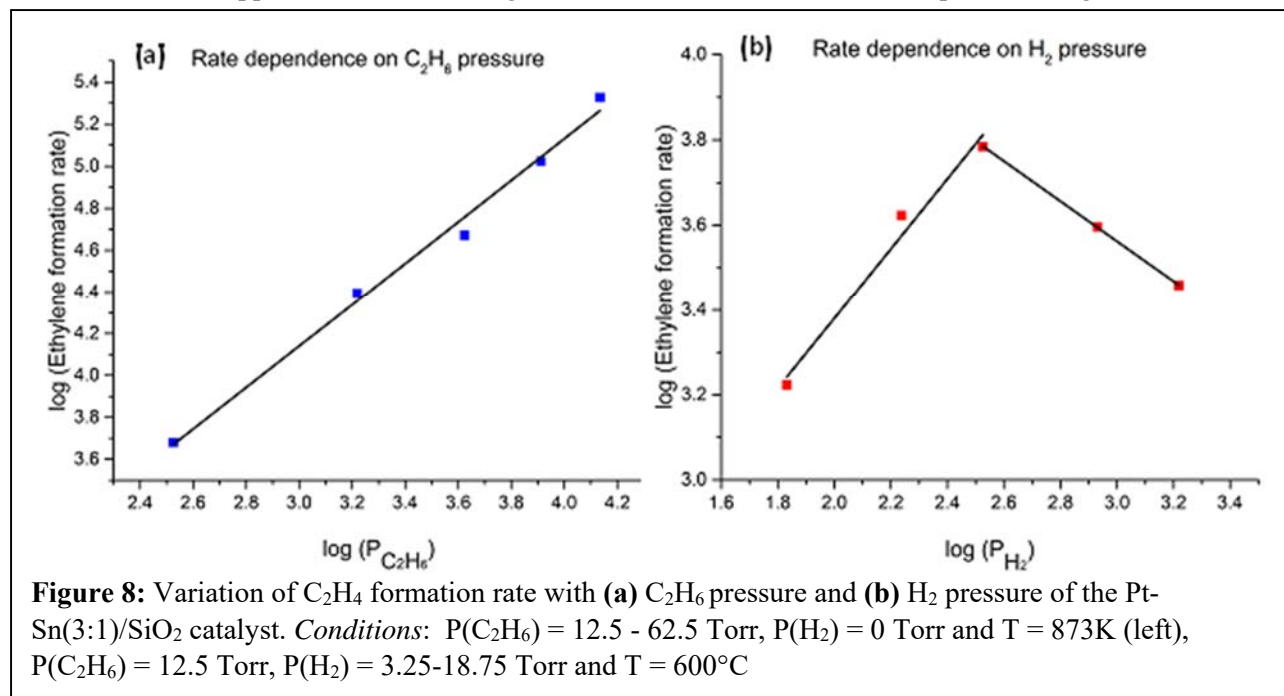
particles that were larger than 3 nm. Even though the average particle size of the two catalysts was quite close, the absence of slightly larger particles on H-ZSM-5 supported catalysts could be responsible for the higher activity of this catalyst.

To obtain more insight on the kinetics of C_2H_6 dehydrogenation on SiO_2 supported catalysts, further experiments were performed with Pt/SiO_2 and Pt-Sn(3:1)/SiO_2 to determine rate

orders of the reaction with respect to C_2H_6 and H_2 and apparent activation energies. For the Pt/SiO_2 catalyst, C_2H_4 formation rate increased monotonically with increasing partial pressure of C_2H_6 or H_2 and reaction rate orders with respect to C_2H_6 and H_2 were 1.04 and 0.34, respectively. Pt-Sn(3:1)/SiO_2 catalyst also

7

exhibited a monotonic increase in C_2H_4 formation rate with increasing C_2H_6 pressure. However, increasing the pressure of H_2 above 12.5 Torr caused an inversion in the reaction order from positive to negative. Both sets of results are illustrated in **Figure 8**. The reaction order with respect to C_2H_6 was 0.99, the reaction order with respect to H_2 is 0.82 for H_2 pressures up to 12.5 Torr and -0.47 for H_2 pressures between 12.5 and 25 Torr. The apparent activation energies were then measured over the temperature range of 500-600°C
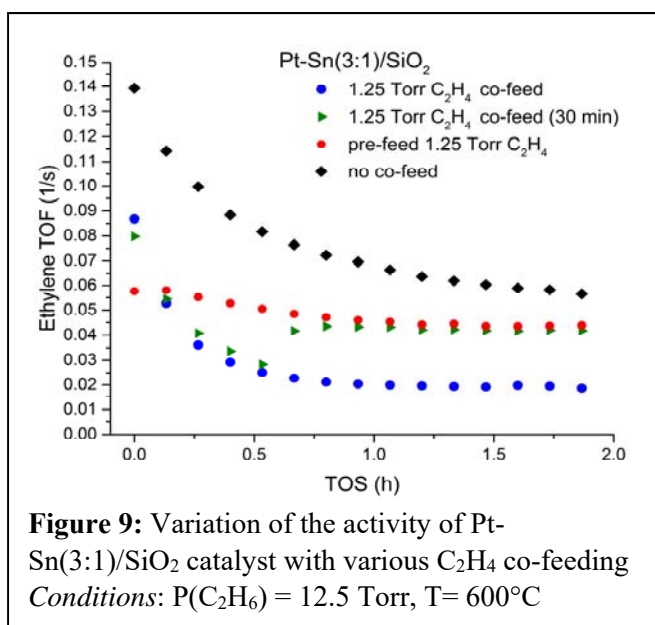

Figure 8: Variation of C_2H_4 formation rate with **(a)** C_2H_6 pressure and **(b)** H_2 pressure of the Pt-Sn(3:1)/SiO$_2$ catalyst. *Conditions*: P(C_2H_6) = 12.5 - 62.5 Torr, P(H_2) = 0 Torr and T = 873K (left), P(C_2H_6) = 12.5 Torr, P(H_2) = 3.25-18.75 Torr and T = 600°C

using standard conditions of 12.5 Torr C_2H_6/He balance and without co-feeding H_2. The apparent activation energies for the Pt/SiO$_2$ and Pt-Sn(3:1)/SiO$_2$ catalysts were 36 and 24 kJ/mole, respectively, in accordance with the enhanced C_2H_6 dehydrogenation activity of the Pt-Sn(3:1)/SiO$_2$ catalyst.

After documenting the beneficial effect of H_2 co-feeding on the formation of C_2H_4, the effect of the other product species on the reaction rate was investigated by co-feeding C_2H_4. To obtain extensive insight about the effect of C_2H_4 co-feeding, 3 different experiments were performed on Pt and Pt-Sn catalysts supported on SiO$_2$ and γ-Al$_2$O$_3$. In the first experiment, C_2H_4 was co-fed with 12.5 Torr C_2H_6 with a C_2H_4:C_2H_6 molar ratio of 1:10 corresponding to the partial pressure of 1.25 Torr C_2H_4. Co-feeding lasted for the entire course of the reaction (2 hrs). In the second experiment, 12.5 Torr C_2H_6 and 1.25 Torr C_2H_4 were co-fed only for 30 minutes, after which C_2H_4 flow was stopped and only 12.5 Torr C_2H_6 in balance helium was flown through the reactor. In the third experiment, following the *in situ* reduction, catalyst was exposed to 1.25 Torr C_2H_4 in helium flow for 30 mins, after which, C_2H_4 flow was stopped and C_2H_6 dehydrogenation was carried out without co-feeding for 2 hours. All the catalysts suffered an activity loss with 1.25 Torr C_2H_4 co-feeding. This result was the exact opposite of what we observed in the case of H_2 co-feeding. When the catalyst was pre-fed with 1.25 Torr C_2H_4 prior to the C_2H_6 dehydrogenation without

8

co-feeding, Pt-Sn(3:1)/γ-Al$_2$O$_3$ catalyst maintained a visibly better activity than 1.25 Torr C$_2$H$_4$ co-feeding condition. Its monometallic counter-part, on the other hand, had a steadied activity much closer to the no co-feed case. The same trend was also observed on SiO$_2$ supported catalysts with the additional feature that, the deactivation profile of those catalysts was less steep than γ-Al$_2$O$_3$ supported catalysts. In the experiments with only 30 minutes of C$_2$H$_4$ co-feeding, the activity showed a step change increase as soon as the C$_2$H$_4$ flow ceased. Except the Pt/γ-Al$_2$O$_3$ catalyst on which the increased activity slightly exceeded that of no co-feed experiment, increased activity converged to that of pre-feed C$_2$H$_4$ run for the other catalysts. The step change in the activity resulted from switching off C$_2$H$_4$, can be attributed to the surface species that established a rapid equilibrium with C$_2$H$_4$. We suggest that these species or C$_2$H$_4$ itself could be site-blocking agents. As a representative, variation of C$_2$H$_4$ TOF values with TOS for Pt-Sn(3:1)/SiO$_2$ catalyst during those four experiments are shown in **Figure 9**.

E. Development of a microkinetic model

Figure 9: Variation of the activity of Pt-Sn(3:1)/SiO$_2$ catalyst with various C$_2$H$_4$ co-feeding *Conditions*: P(C$_2$H$_6$) = 12.5 Torr, T= 600°C
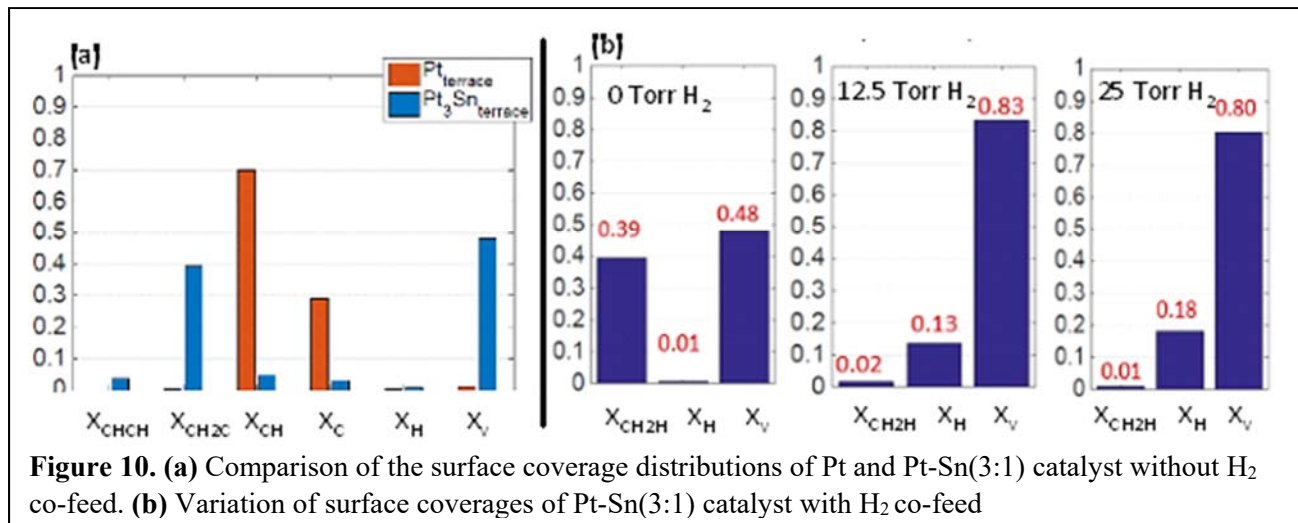
To gain a better understanding of the catalyst behavior and role of surface coverage during the reaction, a microkinetic model was built using the DFT-derived parameters on Pt and Pt$_3$Sn surfaces. The full reaction network, consisting of 33 elementary steps, 4 gas phase species, and 16 surface intermediates was included in the model

For the monometallic Pt catalyst, the microkinetic model predicted a surface coverage of 70% CH and 29% C at the standard feed conditions of 12.5 Torr C$_2$H$_6$ flow and balance helium. When H$_2$ was co-fed at 25 Torr, the number of vacant sites increased by a factor of 3, resulting in a positive reaction rate order with respect to H$_2$, which was in agreement with the experimental trend. For Pt-Sn(3:1) surfaces, the microkinetic model predicted significantly more number of vacant sites compared to the case of pure Pt surfaces – even in the absence of H$_2$. The most abundant surface intermediate (MASI) was identified to be CH$_2$C. The comparison of surface coverage distributions in the absence of H$_2$ co-feeding is shown in **Figure 10**. When H$_2$ co-feeding was introduced, the fraction of vacant sites increased and passed through a maximum at 12.5 Torr H$_2$ – consistent with the experimental measurements of reaction rate versus H$_2$ feed partial pressure. The MASI shifted from CH$_2$C to H before the maximum rate was reached (**Figure 10**).

9

With adjustments between 0.1-0.3 eV on sensitive parameters, our microkinetic model predicted reaction rate orders of 0.87 and 0.97 for C_2H_6 on Pt and Pt-Sn (3:1), respectively. For rate orders with respect to H_2, 0.23 was computed for Pt. On Pt-Sn(3:1), the volcano type trend in H_2-reaction order was captured, however, the values were lower, 0.16 and -0.14, compared to experimental values of 0.82 and -0.47. Consequently, it can be argued that the microkinetic model highlighted the effect of surface coverages and vacant site distribution on C_2H_6 dehydrogenation activity of Pt and Pt-Sn(3:1) catalysts at varying reaction conditions.

Figure 10. (a) Comparison of the surface coverage distributions of Pt and Pt-Sn(3:1) catalyst without H_2 co-feed. **(b)** Variation of surface coverages of Pt-Sn(3:1) catalyst with H_2 co-feed
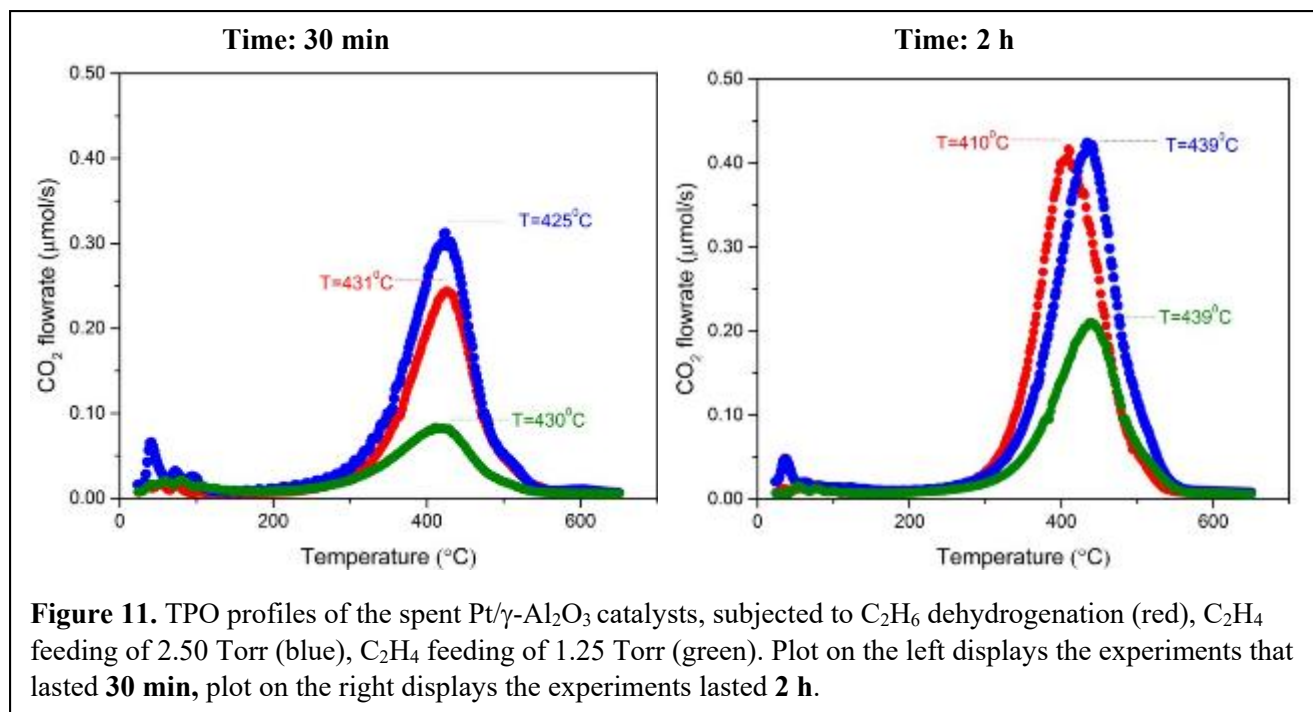
F. Temperature programmed studies of coke formation on Pt-based catalysts

Temperature Programmed Oxidation (TPO) and Temperature Programmed Reduction (TPR) techniques were used to identify and quantify coke deposition on Pt-based catalysts during C_2H_6 dehydrogenation. A series of experiments were performed to assess the influence of: reaction time, C_2H_4 pressure along the bed during the reaction, and catalyst composition on the amount of carbon deposition on the catalyst. For the TPO experiments, 150 mg of spent catalyst sample was heated to 680°C under O_2 flow while evolution of CO_2 was monitored. For the TPR experiments, fresh sample of catalysts were reduced *in situ* at 500°C, cooled down to room temperature, dosed C_2H_4 for 15 min (in a total amount approximately corresponding to 1 monolayer of Pt on the catalyst), purged and heated under H_2 flow to 680°C, while evolution of CH_4 was monitored.

To begin with, clean γ-Al_2O_3 support was fed with C_2H_4 at 600°C with an average pressure of 1.25 Torr and TPO analysis revealed no coke formation showing that bare support did not contribute to coking. Following, samples of Pt/γ-Al_2O_3 catalyst with 25 μmol/g site density was subjected to three different experiments. In the first one, C_2H_6 dehydrogenation without co-feeding was carried out for 2 hrs, while the average C_2H_4 pressure during the experiment was recorded as 1.62 Torr. Subsequently, two successive

10

experiments were performed on the fresh catalysts samples in which catalysts were exposed to only C_2H_4 feeding with pressures of 2.50 and 1.25 Torr respectively. Samples of spent catalysts were collected and TPO analysis was performed. In the second set of experiments, same methods were implemented, but the reaction time was limited to 30 min to investigate its effect on the rate of coke deposition. TPO profiles of the spent catalysts in both sets of the experiments are shown in **Figure 11.** In all the runs, after the release of a small quantity of trapped water vapor and volatile organics residues on the sample at the temperatures
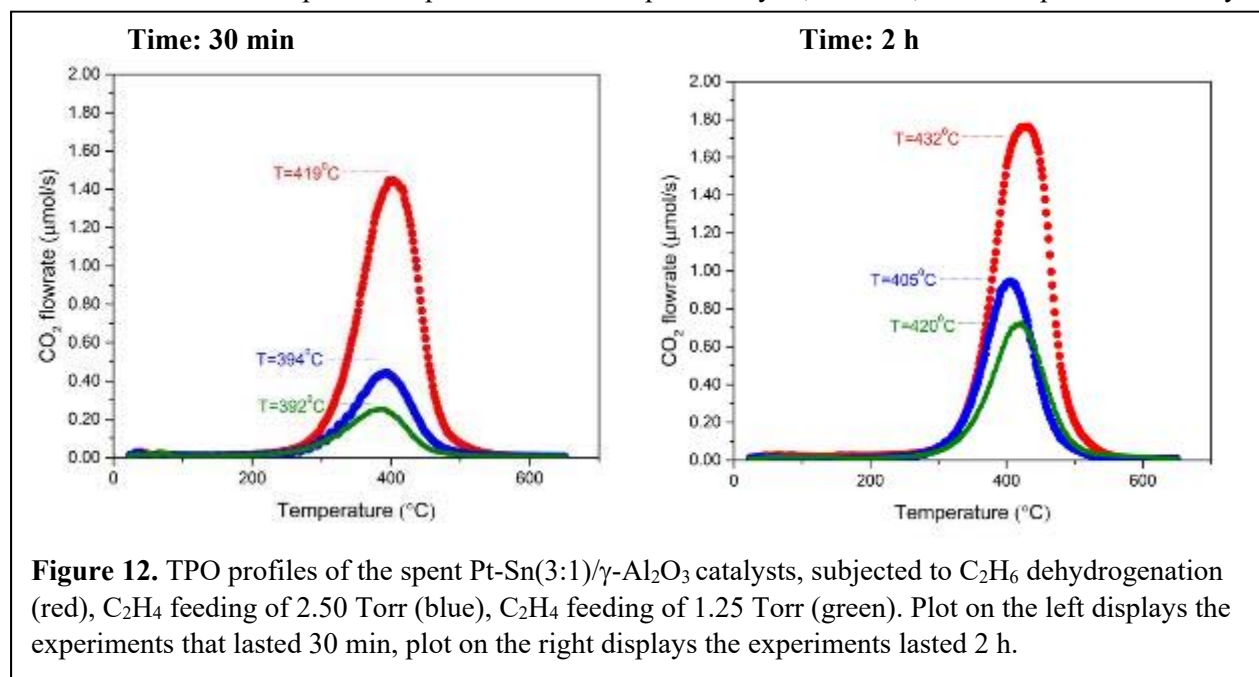

Figure 11. TPO profiles of the spent Pt/γ-Al$_2$O$_3$ catalysts, subjected to C_2H_6 dehydrogenation (red), C_2H_4 feeding of 2.50 Torr (blue), C_2H_4 feeding of 1.25 Torr (green). Plot on the left displays the experiments that lasted **30 min,** plot on the right displays the experiments lasted **2 h**.

lower than 100°C, only one large peak of CO_2 release was observed at higher temperatures. This phenomenon could be attributed to the deposition of a single type of carbonaceous species on the catalyst. Integration of the peak enabled us to quantify the amount of coke deposited on the catalysts during the reaction. In the 30 min experiments, C_2H_6 dehydrogenation (with an average 1.91 Torr of C_2H_4 pressure during the reaction) yielded 1.86 mmol C/gcat, while feeding the catalysts with 2.50 Torr C_2H_4 and 1.25 Torr C_2H_4 for 30 mins, yielded 2.34 and 0.83 mmol C/gcat, respectively. In the second set of the experiments that lasted for 2 hrs, C_2H_6 dehydrogenation (with an average 1.65 Torr of C_2H_4 pressure during the reaction) deposited 2.97 mmol C/gcat, while feeding the catalyst with 2.50 Torr C_2H_4 and 1.25 Torr C_2H_4 for 2 hrs, resulted in 3.09 and 1.65 mmol C/gcat coke deposition, respectively. We conclude that coke deposition on the catalyst is not linear with respect to reaction time, suggesting that in the initial period of the reaction (30 min) coke deposition rate, and thus catalyst deactivation, was much faster than it was at the end of 2 hrs. We also observed that, while given that C_2H_4 feeding by itself leads to coke formation on the catalyst, in varying amounts depending on the C_2H_4 feeding pressure, in the actual C_2H_6 dehydrogenation conditions, carbon deposition might originate from additional sources. This finding was suggested by the 2

11

hr C_2H_6 dehydrogenation experiment having average C_2H_4 pressure of 1.62 Torr, and deposited almost the equal amount of coke with the 2.50 Torr C_2H_4 feeding run.

To probe the effect of catalyst composition on the coke deposition on catalysts, similar experiments were performed on the samples of Pt-Sn(3:1)/γ-Al_2O_3 catalyst with the site density of 81 μmol Pt/gcat. As shown with the TPO profiles in **Figure 12,** qualitatively they were similar to those from Pt/γ-Al_2O_3 samples. Each showed a single peak for CO_2 desorption which was centered in the temperature range of 390-435°C. In terms of carbon deposition quantity, during the 30 min experiments, C_2H_6 dehydrogenation (with an average 3.26 Torr of C_2H_4 pressure during the reaction) deposited 10.33 mmol C/gcat, while feeding the catalysts with 2.50 Torr C_2H_4 and 1.25 Torr C_2H_4 for 30 mins, resulted in 3.31 and 2.01 mmol C/gcat deposition, respectively. During the 2 hrs experiments, C_2H_6 dehydrogenation (with average 2.94 Torr C_2H_4 pressure during the reaction) yielded 12.15 mmol C/gcat, while feeding the catalysts with 2.50 Torr C_2H_4 and 1.25 Torr C_2H_4 for 2 hrs, resulted in 6.05 and 5.12 mmol C/gcat respectively. Overall, these are trends similar to what it was found onPt/γ-Al_2O_3, suggesting that coke formation rate during the initial period of C_2H_6 dehydrogenation was higher than later times and that the amount of coke deposited during C_2H_6 dehydrogenation was highly probable to be more than coke formed by C_2H_4 itself.

In another attempt to distinguish the effect of Sn addition on the binding strength of the monometallic Pt catalyst, TPR studies were performed with Pt/SiO_2 and Pt-Sn(3:1)/SiO_2 catalysts. In contrast with the TPO experiments performed on the spent catalysts, for TPR, fresh samples of the catalyst

Figure 12. TPO profiles of the spent Pt-Sn(3:1)/γ-Al_2O_3 catalysts, subjected to C_2H_6 dehydrogenation (red), C_2H_4 feeding of 2.50 Torr (blue), C_2H_4 feeding of 1.25 Torr (green). Plot on the left displays the experiments that lasted 30 min, plot on the right displays the experiments lasted 2 h.

were reduced *in-situ* and cooled following by C_2H_4 feeding for 15 mins at room temperature. The concentration of the C_2H_4 gas in the feed was 0.4% so that the quantity of C_2H_4 molecules sent to the catalyst was approximately equal to the number of Pt sites available on the catalyst. Following the purging with He

12

for 15 min, catalysts were heated under H_2 flow to 680 and CH_4 evolution were monitored. As shown in **Figure 13**, on the Pt/SiO_2 catalyst, CH_4 showed a small peak around 390°C, which corresponded to the release of 48 µmol of CH_4/ gcat. On the other hand, TPR profile of the Pt-Sn(3:1)/SiO_2 catalyst was dominated by a smaller and wider peak which was integrated to 22 µmol of CH_4/ gcat. Those results could
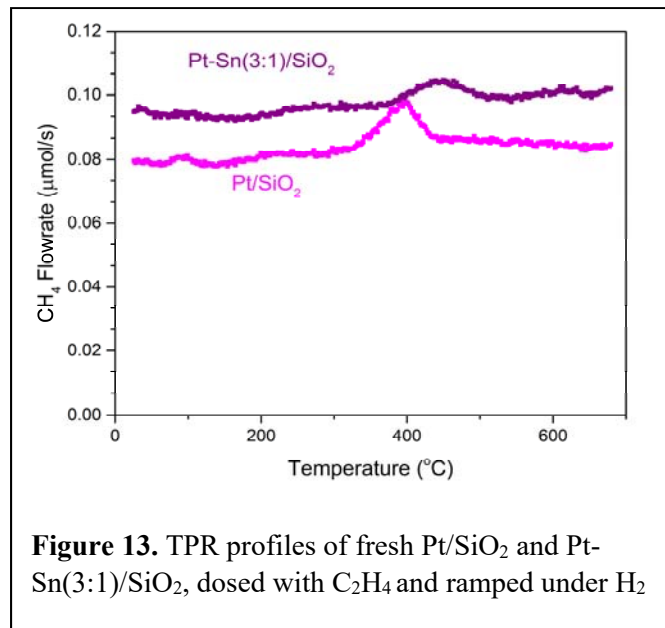
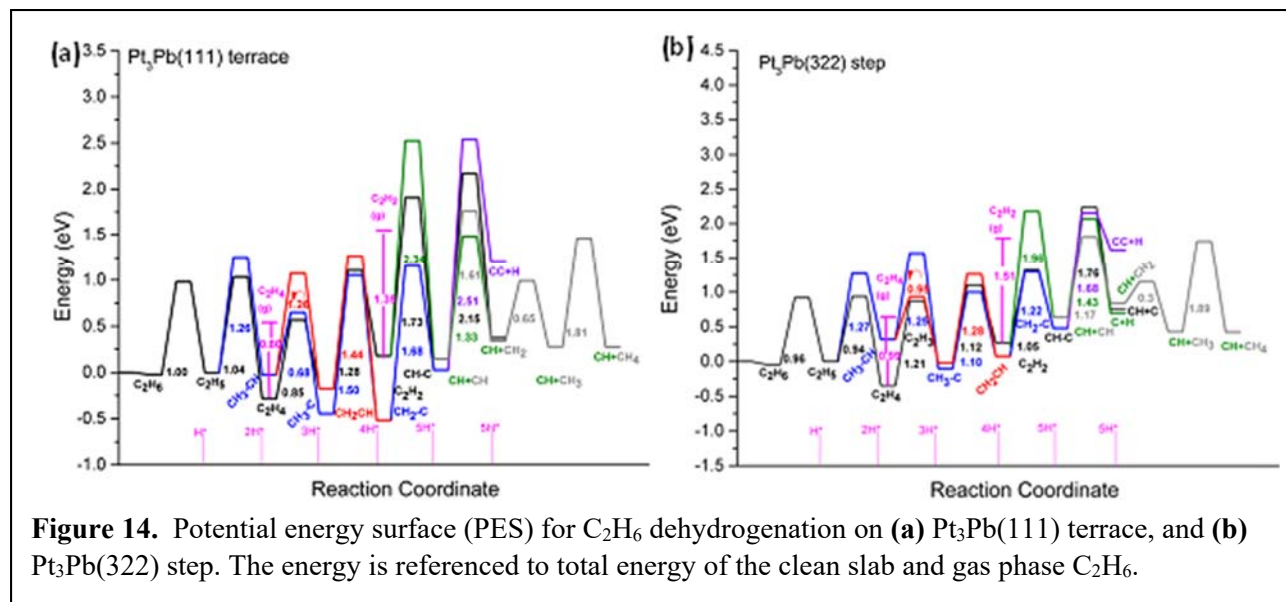**Figure 13.** TPR profiles of fresh Pt/SiO_2 and Pt-Sn(3:1)/SiO_2, dosed with C_2H_4 and ramped under H_2

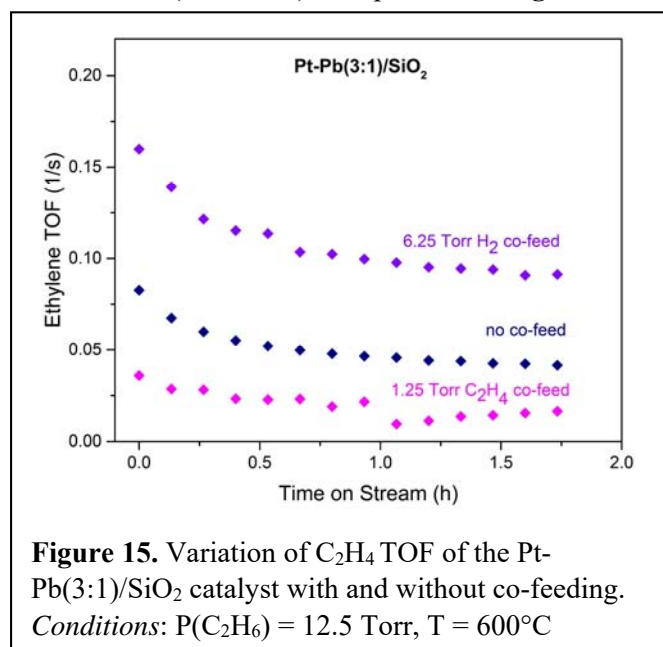be attributed to the decrease in the binding strength of the catalyst upon Sn addition, as predicted by DFT calculations.

G. Ethane dehydrogenation on Pt₃Pb and Pt₃Zn catalysts

We performed a set of DFT calculations on the other promising bimetallic systems that we identified earlier. In particular, C2H6 dehydrogenation was studied on $Pt_3Pb(111)$ terrace and $Pt_3Pb(322)$ step surfaces. Calculated potential energy surfaces (PES) for the two facets are shown in **Figure 14.** Comparison of the energetics showed that, for both facets, deep dehydrogenation and C-C bond breaking were *not* favored over dehydrogenation. Also, on $Pt_3Pb(111)$, C_2H_4 desorption was only 0.05 eV easier than dehydrogenation to form C_2H_3 (0.80 eV vs. 0.85 eV), whereas this difference was increased to 0.22 eV on the $Pt_3Pb(322)$ step surface (0.99 eV vs. 1.21 eV). Therefore, Pt_3Pb step surface is more likely to prefer desorbing C_2H_4 over its dehydrogenation. Consequently, reaction kinetics studies were performed on a Pt-Pb catalyst. Synthesis of the catalyst was done via sequential impregnation of Pt and Pb precursors on the silica support with a target atomic ratio of Pt-Pb 3:1. The Pt-Pb(3:1)/SiO_2 catalyst was then evaluated for its activity for C_2H_6 dehydrogenation at 600°C with 12.5 Torr C_2H_6/balance He feed. Reaction rate orders with respect to C_2H_6 and H_2, effect of C_2H_4 co-feeding on the

13

Figure 14. Potential energy surface (PES) for C_2H_6 dehydrogenation on **(a)** $Pt_3Pb(111)$ terrace, and **(b)** $Pt_3Pb(322)$ step. The energy is referenced to total energy of the clean slab and gas phase C_2H_6.

activity and apparent activation energy for the reaction were investigated. The behavior of the catalyst was similar to Pt-Sn(3:1)/SiO$_2$, as the rate order with respect to C_2H_6 was 0.91, increase in the H$_2$ co-feeding provided a monotonic increase in the reaction rate, resulting in a rate order calculated as 0.62, and apparent activation energy was found to be 25 kJ/mole. Similarly to the Pt-Sn catalyst, the effect of C_2H_4 co-feeding was investigated by introducing a lower dose of C_2H_4 flow (1.25 Torr pressure) over catalyst compared to the H$_2$ flow (6.25 Torr). As plotted in **Figure 15**, H$_2$ co-feeding of 6.25 Torr pressure provided an enhancement in the C_2H_4 TOF whereas 1.25 Torr C_2H_4 co-feeding yielded lower activity.

Figure 15. Variation of C_2H_4 TOF of the Pt-Pb(3:1)/SiO$_2$ catalyst with and without co-feeding. *Conditions*: P(C_2H_6) = 12.5 Torr, T = 600°C

Another promising bimetallic system predicted by our DFT work was the Pt$_3$Zn alloy. Similarly to the Pt$_3$Sn and Pt$_3$Pb systems, 4-layer slabs of the Pt$_3$Zn alloy were prepared to represent Pt$_3$Zn(111) terrace and Pt$_3$Zn(322) step surfaces. Prior to computations of complete ethane dehydrogenation reaction network, binding strengths of the reaction intermediates were computed and compared with that of Pt, Pt$_3$Sn and Pt$_3$Pb surfaces studied previously **(Figure 16)**. We found that, with the exception
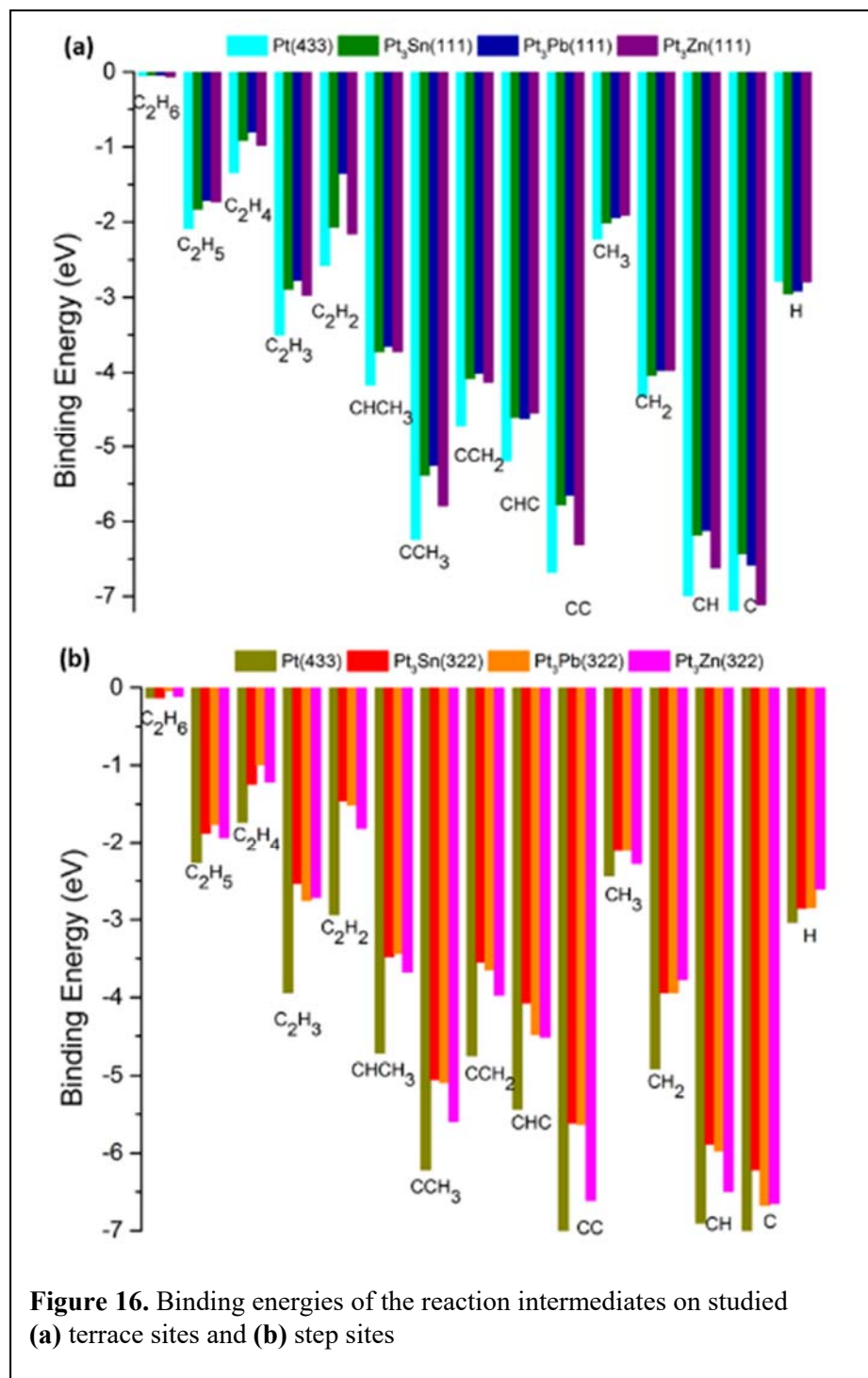
of H atom binding energy on the terrace, almost all the intermediate species were less strongly bound to the alloy surfaces. Particularly, stronger binding of CH and C species on pristine Pt compared to the alloy

14

surfaces, was in accordance with the predictions of the microkinetic model regarding nearly fully covered Pt surfaces under realistic reaction conditions. Furthermore, reduced binding strength would indicate lower probability of irreversible adsorption of coke precursors and deposits. The energetics of the entire C_2H_6 dehydrogenation network was then computed on the terrace and steps of Pt_3Zn surfaces. As plotted in **Figure 17,** PES suggest that, on $Pt_3Zn(111)$ terrace, C_2H_4 was m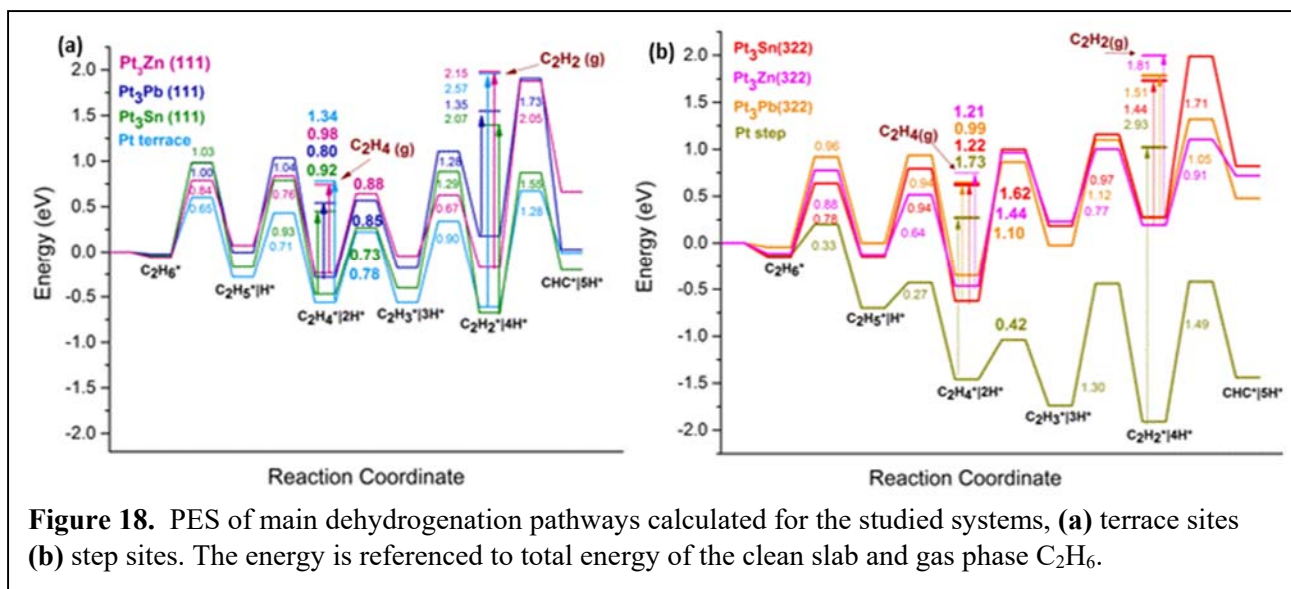ore likely to transform to vinyl instead of desorbing from the surface (0.88 eV vs. 0.98 eV), whereas on the $Pt_3Zn(322)$ step surface, C_2H_4 desorption was favored over further dehydrogenation (1.21 eV vs 1.43 eV).

Figure 16. Binding energies of the reaction intermediates on studied **(a)** terrace sites and **(b)** step sites

15

Figure 17. Potential energy surface (PES) for C_2H_6 dehydrogenation on **(a)** $Pt_3Zn(111)$ terrace, and **(b)** $Pt_3Zn(322)$ step. The energy is referenced to total energy of the clean slab and gas phase C_2H_6.
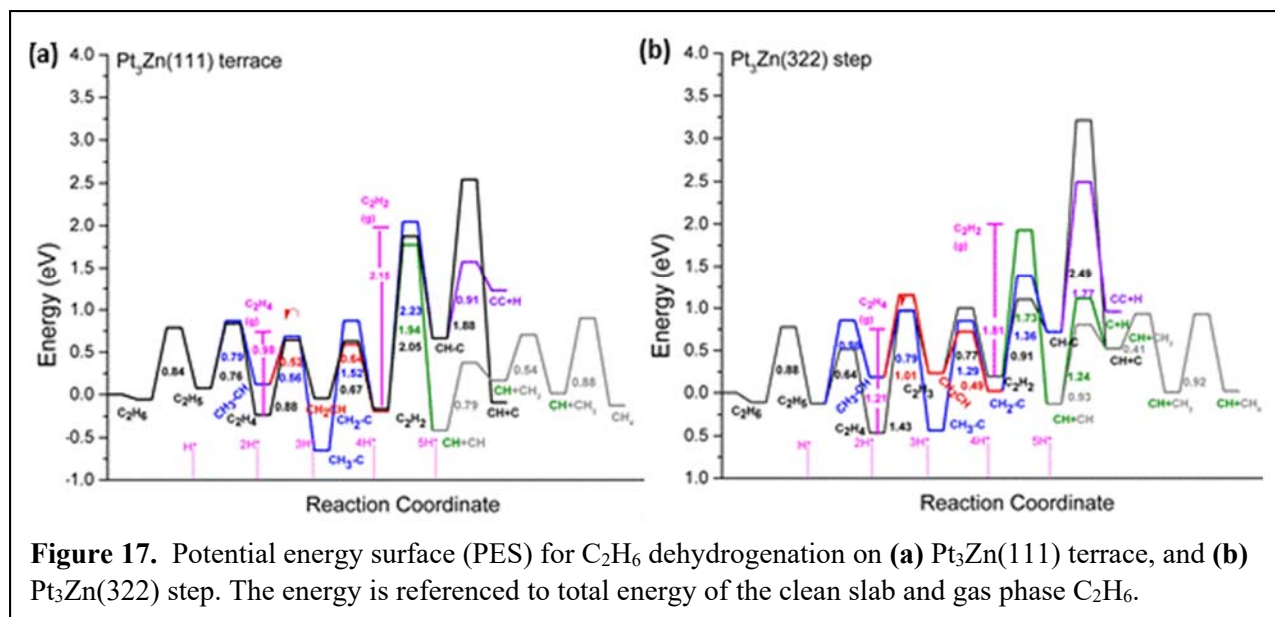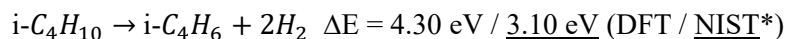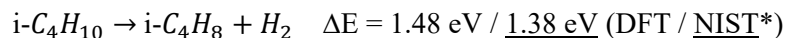
To make a brief comparison on the energetics of Pt based systems that we have studied so far, the main dehydrogenation path starting from C_2H_6 adsorption on the surface up to CH-C formation for each surface is plotted in **Figure 18** for both terrace and step sites. The key conclusion from this comparison is that on pristine Pt steps, deep dehydrogenation is favored, whereas the alloy step sites favor desorption of C_2H_4 over its dehydrogenation, rendering our studied Pt-alloy catalysts very promising, particularly for smaller nanoparticles, where the majority of the active sites could indeed be undercoordinated.
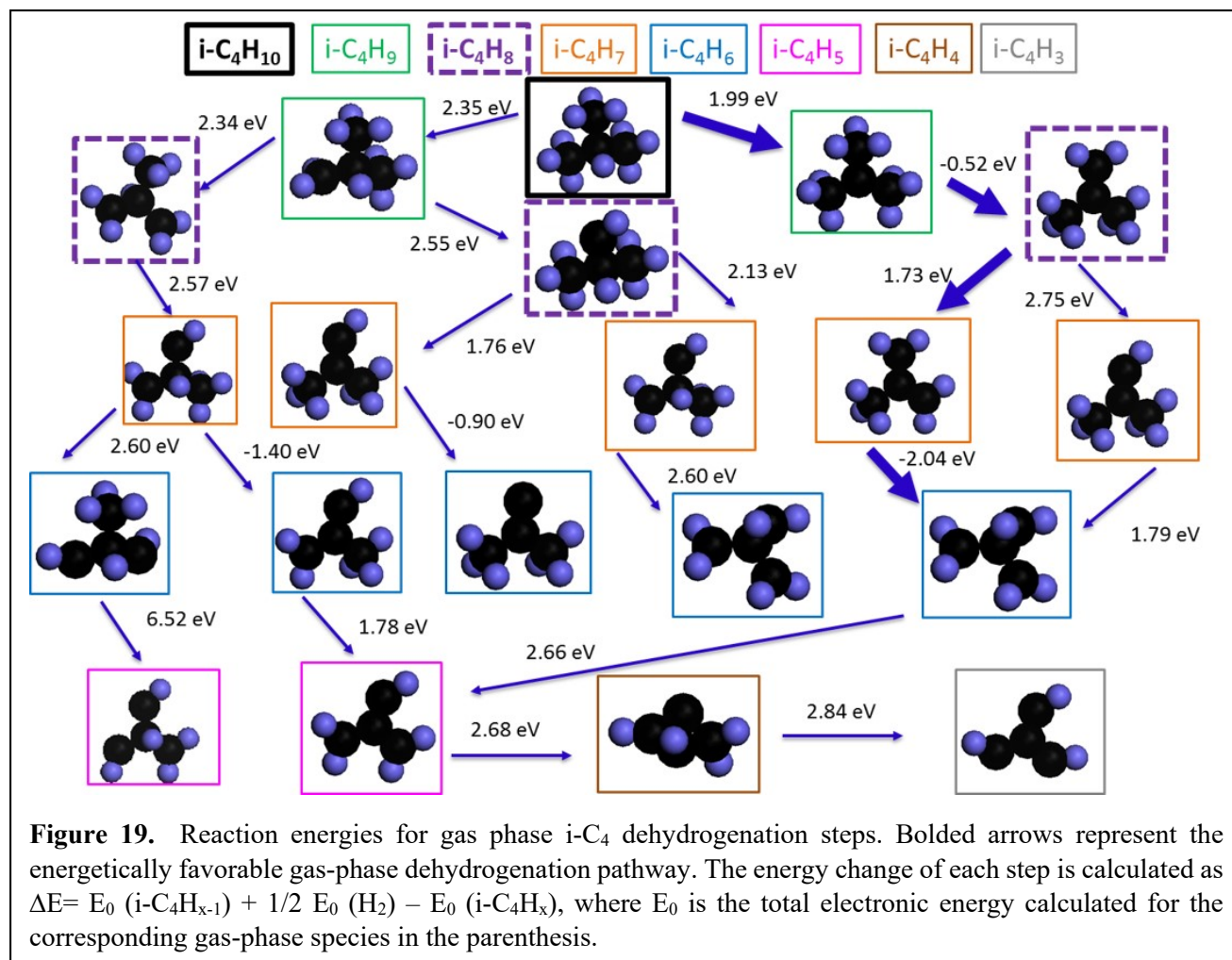

Figure 18. PES of main dehydrogenation pathways calculated for the studied systems, **(a)** terrace sites **(b)** step sites. The energy is referenced to total energy of the clean slab and gas phase C_2H_6.

16

I. Preliminary gas phase i-C$_4$ dehydrogenation calculations

To investigate the effect of fuel's molecular structure on catalyst activity and coke formation, isobutane (i-C$_4$) was selected as a probe molecule for further studies. Isobutane is the smallest branched alkane molecule that can undergo dehydrogenation, cracking and isomerization. The overall gas-phase reaction energies for two possible i-C$_4$H$_{10}$ dehydrogenation reactions follow:

$$i\text{-}C_4H_{10} \rightarrow i\text{-}C_4H_8 + H_2 \quad \Delta E = 1.48 \text{ eV} / \underline{1.38 \text{ eV}} \text{ (DFT / \underline{NIST}*)}$$

$$i\text{-}C_4H_{10} \rightarrow i\text{-}C_4H_6 + 2H_2 \quad \Delta E = 4.30 \text{ eV} / \underline{3.10 \text{ eV}} \text{ (DFT / \underline{NIST}*)}$$

*Experimentally determined heat of reaction at 25°C

Prior to the calculation of thermochemistry and activation barriers of the full dehydrogenation reaction network on Pt-based surfaces, gas phase energetics of i-C$_4$ species were calculated. **Figure 19** shows the energy changes associated with dehydrogenation of gas phase i-C$_4$ species with respect to gas phase isobutane (i-C$_4$H$_{10}$).

Figure 19. Reaction energies for gas phase i-C$_4$ dehydrogenation steps. Bolded arrows represent the energetically favorable gas-phase dehydrogenation pathway. The energy change of each step is calculated as $\Delta E = E_0 (i\text{-}C_4H_{x-1}) + 1/2 \, E_0 (H_2) - E_0 (i\text{-}C_4H_x)$, where E_0 is the total electronic energy calculated for the corresponding gas-phase species in the parenthesis.
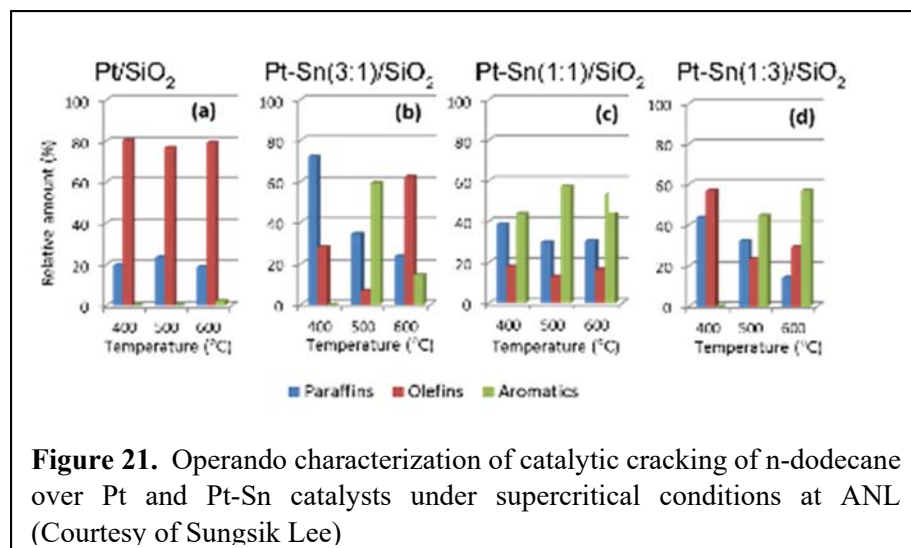
17

J. Sample preparation and endothermic evaluation at UTRC and ANL

To assess the usability of the studied catalysts in actual hypersonic flight conditions, a heat exchanger rig test was performed at United Technologies Research Center (UTRC). During the test, the catalyst was suspended in n-dodecane as the surrogate of jet fuel and endotherms for n-dodecane conversion promoted by catalytic dehydrogenation would be obtained as a function of temperature. The UW teamworked to identify a catalyst with high activity and good dispersion in n-dodecane that would minimize the tendency to plug the tube. Comparing different support materials, Cabosil and Davisil silica were selected as good candidates due to their slower sedimentation rate in dodecane, compared to γ-Al_2O_3 as the support. Thus, Pt-Sn(3:1)/Cabosil, and Pt-Sn(3:1)/Davisil catalysts were synthesized. To improve dispersion of the catalyst in dodecane, we increased the surface hydrophobicity through an esterification reaction with alcohols. Fresh catalysts were "cooked" with ethanol for 4 hours and then washed with hexane. "Cooked" catalysts had lower sedimentation rates compared to the non-cookedcatalysts without any loss in the catalytic activity. The Pt-Sn(3:1)/Cabosil catalyst had the best balance of C_2H_6 dehydrogenation activity and low sedimentation rate in dodecane. Approximately 12 g of Pt-Sn(3:1)/Cabosil catalyst esterified with ethanol was prepared and shipped to UTRC for evaluation. Endotherms obtained at UTRC are shown in
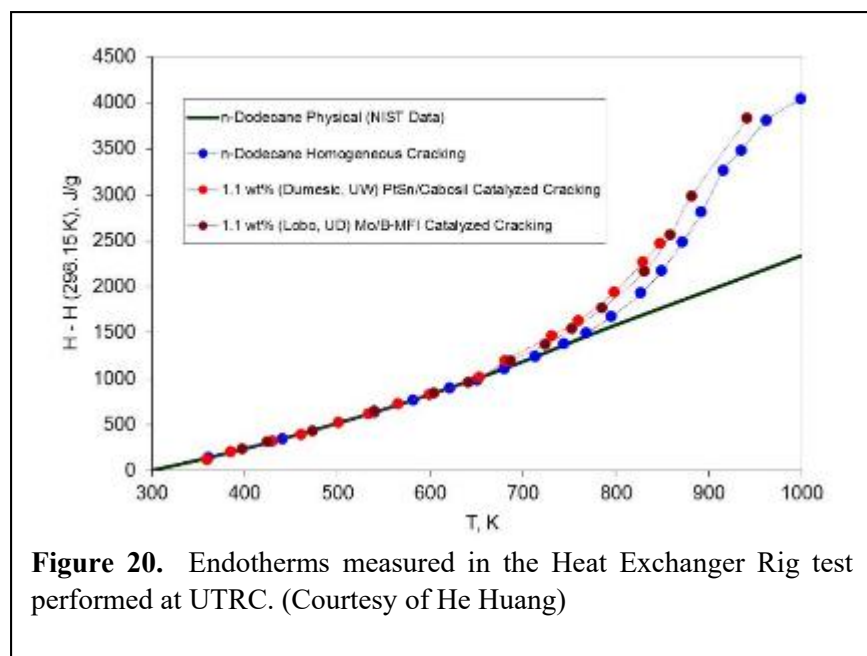
Figure 20. The UW-prepared Pt-Sn/Cabosil catalyst gave approximately 300 s^{-1} TOF of endothermic events to yield increased endotherms up to 310 J/g compared to homogeneous cracking of n-dodecane. Around 848 K, the tube was plugged possibly due to coke deposition.

Figure 20. Endotherms measured in the Heat Exchanger Rig test performed at UTRC. (Courtesy of He Huang)

18

Figure 21. Operando characterization of catalytic cracking of n-dodecane over Pt and Pt-Sn catalysts under supercritical conditions at ANL (Courtesy of Sungsik Lee)

As a part of another collaborative work, fresh and spent samples of Pt and Pt-Sn catalysts supported on γ-Al$_2$O$_3$ and SiO$_2$, together with bare support samples, were sent to ANL, where the Winans' Group performed *in situ/operando* SAXS and XANES studies. As shown in **Figure 21,** catalytic cracking of n-dodecane in the temperature range of 400-700°Cover the Pt and Pt-Sn catalysts, yielded a wide range of products, spanning paraffins, olefins and aromatics. One substantial result was the emergence of aromatic species on Pt-Sn(3:1)/SiO$_2$ after 500°C which could be affiliated with the coke formation triggering the tube blocking in the test at UTRC around 575°C.

List of publications:

1- **"Direct time-domain observation of attosecond final-state lifetimes in photoemission from solids"** Z. Tao, C. Chen, T. Szilvasi, M. Keller, M. Mavrikakis, H, Kapteyn and M. Murnane *Science* **353**, 62 (2016).

2- **"An adsorption study of CH$_4$ on ZSM-5, MOR, and ZSM-12 zeolites"** Y. Zhang, J. Yu, Y.Yeh, R. J. Gorte, S. Rangarajan, M. Mavrikakis *Journal of Physical Chemistry C* **119,** 28970 (2015).

3- **"Identification of O-rich structures on Platinum(111)-supported ultrathin iron oxide films"** L. R. Merte, Y. Bai, H. Zeuthen, G. Peng, L. Lammich, F. Besenbacher, M. Mavrikakis and S. Wendt *Surface Science* (2016).

4- **"Adsorption of small alkanes on ZSM-5 zeolites: Influence of Bronsted Sites"** Y. H. Yeh, R. J. Gorte, S. Rangarajan and M. Mavrikakis *Journal of Physical Chemistry C* **120**, 12132 (2016).

5- **"Ethane dehydrogenation on pristine and AlO$_x$ decorated Pt stepped surfaces"** G. Peng, M. Kumbhalkar, D. Gerceker, J. A. Dumesic, M. Mavrikakis (submitted).

6- **"Direct Visualization of Catalytically Active Sites at the FeO–Pt(111) Interface"**, W. Kudernatsch, G. Peng, H. Zeuthen, Y. Bai, L. R. Merte, L. Lammich, F. Besenbacher, M. Mavrikakis, and S. Wendt *ACS Nano* **9**, 7804 (2015).

7- **"Controlling the electronic structure of graphene using surface-adsorbate interactions"**, P. Matyba, A. Carr, C. Chen, D. L. Miller, G. Peng, S. Mathias, M. Mavrikakis, D. S. Dessau, M. W. Keller, H. C. Kapteyn, and M. Murnane *Physical Review B* **92**, 041407(R) (2015).

8- **"The nature of the Fe-graphene interface at the nanometer level"**, M. Cattelan, G. W. Peng, E. Cavaliere, L. Artiglia, A. Barinov, L. T. Roling, M. Favaro, I. Píš, S. Nappini, E. Magnano, F. Bondino, L. Gavioli, S. Agnoli, M. Mavrikakis and G. Granozzi, *Nanoscale* **7**, 2450 (2015).

9- **"Adsorbate Diffusion on Transition Metal Nanoparticles"**, G. Peng and M. Mavrikakis, *Nano Letters* **15**, 629 (2015).

19

10- **"Water Clustering on Nanostructured Iron Oxide Films"**, L. R. Merte, R. Bechstein, G. Peng, F. Rieboldt, C. A. Farberow, H. Zeuthen, J. Knudsen, E. Lægsgaard, S. Wendt, M. Mavrikakis, F. Besenbacher, *Nature Communications* **5**, 4193 (2014).

Students and postdocs supported by the project

Duygu Gerceker (PhD student)

Tibor Szilvasi (Postdoc)

Srinivas Rangarajan (Postdoc)

Guowen Peng (Postdoc)

Matthias Jorgensen (MS student)

Honors or other noteworthy events/activities that might be of interest

- **James A. Dumesic:**
- 2014 - Elected into the **National Academy of Sciences**
- 2014 - Thomson Reuters Highly Cited Researcher – 2014
- 2014 - Thomson Reuters 2014 The World's Most Influential Scientific Minds
- 2014 - Biofuels Digest: The Top 100 People in the Bioeconomy, 2013-14
- 2014 - Eastman Lectures, University of Virginia
- 2014 - Founders Lectures, University of California - Los Angeles
- 2015 - Fellow of the Royal Society of Chemistry
- 2015 - Alpha Chi Sigma Award of the American Institute of Chemical Engineers
-
- **Manos Mavrikakis:**
- Editor-in-Chief, *Surface Science*
- Chair, Department of Chemical & Biological Engineering, UW-Madison (7/15 -)
- Fellow of the American Vacuum Society (AVS); 2016
- Vilas Associate, University of Wisconsin – Madison (2016-2018)
- Vilas Distinguished Achievement Professor, University of Wisconsin – Madison (2015-2019).
- L. T. Fan Distinguished Lectureship, Chemical Engineering Department, Kansas State University (2015).
- R. H. Wilhelm Award in Chemical Reaction Engineering, AIChE (2014)
- Fellow of the American Association for the Advancement of Science (AAAS); 2014
- Byron Bird Award for Excellence in a Research Publication, College of Engineering, UW-Madison (2014)
- Kellett Mid-Career Faculty Researcher Award (UW-Madison, 2014)

PI Name: Sungsik Lee, Sungwon Lee and Randall E. Winans
Address: X-ray Science Division, Argonne National Laboratory, 9700 S. Cass Avenue
Argonne, IL 60439

Statement of objectives: The goal of the proposed studies is 1) to investigate the catalyst stability under high temperature and pressure conditions, 2) to identify sub-nm cluster assemblies for new catalytic materials with well-defined size and composition in the intriguing, but not yet explore the sub-nm size regime 3) monitor formation of coke and collect reaction products to evaluate reactivity and selectivity of the reaction ex-situ using GC-MS 4) ultimately understanding factors that affect activity and selectivity of catalysts suitable for endothermic fuel cooling of next generation hyper-sonic vehicles under supercritical conditions. Many of the physical and transport properties of an SCF are intermediate between those of a liquid and those of a gas, which provides high reaction rate for some reactions that are limited by diffusion in the liquid phase. These unique properties are not fully studied on nano or subnanosized metal nanoparticls in SCFs.

Methodology developed: In-situ synchrotron-based small angle X-ray scattering (SAXS) and X-ray Absorption Near Edge Structure (XANES) was applied to address catalyst stability under high temperature and pressure conditions. The powder catalysts were provided by the Dumesic and Mavrikakis Group at University of Wisconsin. n-dodecane, a good surrogate for jet fuels, is chosen for this study due to its higher molecular mass and lower hydrogen to carbon ratio which reflect the n-alkane content of jet fuels. SAXS and XANES measurements were carried out from 25 to 600 °C at a constant pressure of 750 psi. The monitoring and evaluation of catalyst cracking products (liquid) was carried out by using GC-MSD. In addition, the spent catalysts were characterized by ex-situ Raman spectroscopy to characterize the formation of carbonaceous deposits, coke, on the surface of the catalyst.

The long term goal of our research team is to be able to provide structural, chemical and mechanical information about the catalysts immobilized on the substrates. To enable analysis of these catalytic thin films under high temperature and pressure we designed and built a grazing incidence small angle X-ray scattering (GISAXS) cell (Figure 1). The key elements that ensure cell performance are: a) the choice of high grade chemically resistant Inconel alloy for cell's body components; b) incorporation of class 2a CVD single crystal diamonds as mechanically stable, low scattering background material for X-ray windows and c) sapphire windows mounted perpendicular to the X-ray beam for simultaneous monitoring of the changes in the fuel by incorporation with additional optical spectroscopy
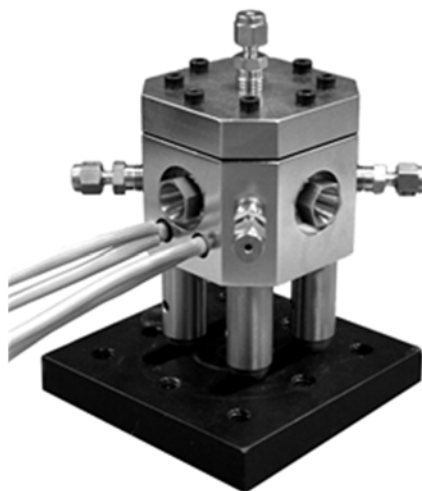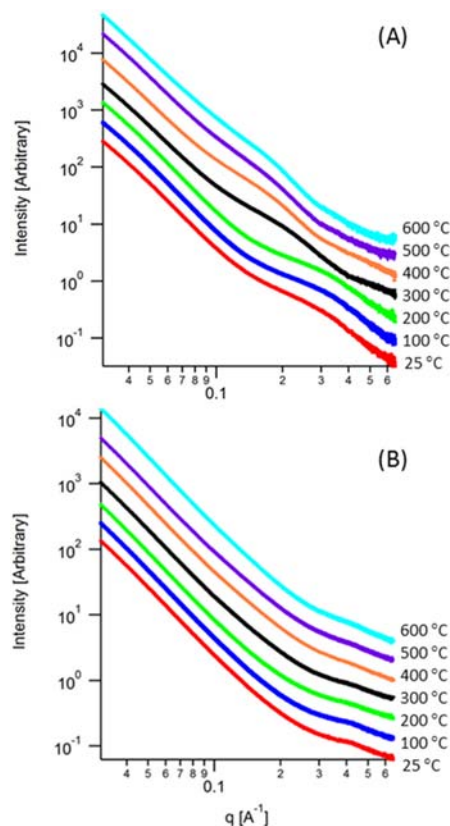

Figure 1. Grazing incidence small angle X-ray scattering(GISAXS) cell

Accomplishments:

Effect of Particle Size Upon Pt/SiO$_2$ Catalytic Cracking of n-Dodecane Under Supercritical Conditions: in situ SAXS and XANES Studies:

In this study, we used two different synthesis methods to prepare the Pt/SiO$_2$ catalysts: ion-exchange (IE) and incipient wetness impregnation (IWI). The properties of Pt catalysts and the catalytic performance were characterized by synchrotron-based small angle X-ray scattering (SAXS) and X-ray Absorption Near Edge Structure (XANES). The cracking of n-dodecane as an endothermic hydrocarbon fuel in the flow cell reactor was carried out under supercritical conditions. GC/MS (gas chromatography–mass spectrometry) was used to analyze the reaction products at various stages of the reaction. Figure 2 shows the background corrected SAXS scattering intensities of Pt/SiO$_2$ catalysts prepared by two different methods in the temperature range of 25 – 600 °C at 750 psi with n-dodecane. A broad scattering peak appears in the high q region (0.2<q<0.4, Å^{-1}) at an ambient temperature (red line), indicating the presence of nanoparticles as shown in Figure 2(A). This peak started to shift to the low q range as the temperature approached the supercritical state at 300 °C (black line). The shift in scattering peak to the lower q regime continued with an increasing temperature, indicating an increase in particle size and increased polydispersity as the temperature increased. On the contrary, a relatively small change in temperature of the scattering profiles was obtained with Pt/SiO$_2$ by the impregnation process as shown in Figure 2(B). The scattering peak appeared at q > 0.4(Å^{-1}) may indicate that the particle size is smaller than those by the ion-exchange process and is not affected by the reaction temperature. The size distribution profiles of the Pt/SiO$_2$ prepared ion-exchange and impregnation and corresponding

Figure 2. Background corrected in situ SAXS scattering profiles of Pt/SiO$_2$ catalysts prepared by (A) ion exchange and (B) impregnation method in the temperature range of 25 – 600 °C at 750 psi with n-dodecane

particle size values are illustrated in Figure 3. In the case of the Pt/SiO$_2$ prepared by ion-exchange shown in Figure 3(A), the particle size was 12 Å (diameter) at an ambient temperature but increased up to 21 Å as the temperature increased. Interestingly, there was a sudden increase in particle size obtained when the reaction condition approached the supercritical regime, near 300 °C. The size distribution profiles as shown in Figure 3(C) broadened as the temperature increased, including a distinctive peak broadening at 300 °C. This indicates that a dynamic size change occurred at this temperature. The average particle size of Pt/SiO$_2$ (IWI) did not change over the given reaction conditions; however, a slight increase in size distribution was observed, as shown in Figure 3(B) and 3(D). Jacobs and coworkers have reported that the preparation parameters affect the distributions of Pt particle size and location, which can influence the stability and the resulting performance of catalysts.[1] In addition, the estimated particle size is about 9 – 10 Å, which is comparably smaller than those from the ion-exchange method. This is in good agreement with the previous finding of Pt/ZSM-5 catalysts.[2]
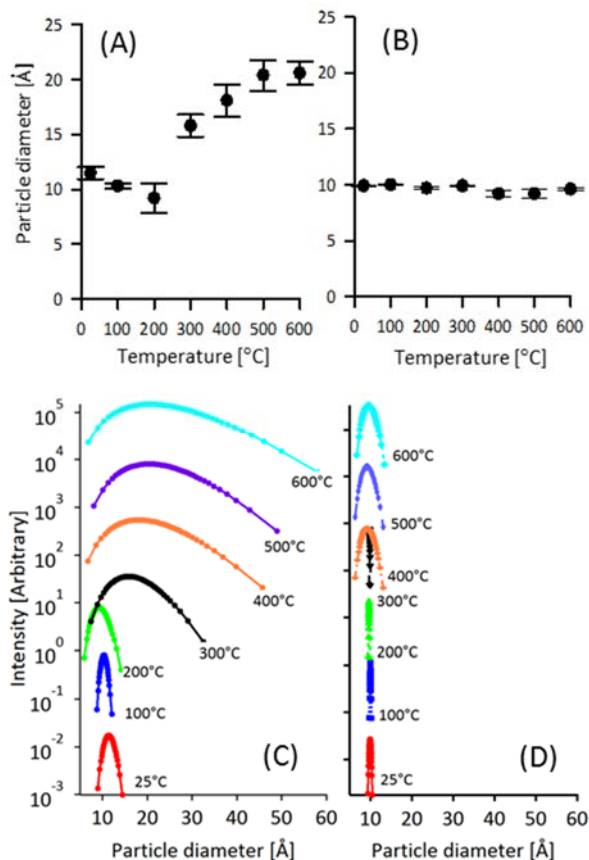
Figure 4 shows in situ XANES (Pt L3 edge) data of Pt/SiO$_2$ catalysts prepared by (A) ion exchange and (B) impregnation method under supercritical conditions with n-dodecane. At room temperature Pt catalysts show a high degree of oxidation, as indicated by the high binding energy shifts and the whiteline height, which was reduced significantly as the reaction temperature reached ~ 200 °C in both of the catalysts. As shown in Figure 4 (C) and (D) respectively, the height of the whiteline and the peak position change over the range of temperatures. The energy shift toward higher energy has been previously reported and interpreted as a change in morphology to a planar structure, and a shift to lower energy as the particle forms a spherical shape.[3,4] This indicates that the size and morphology of platinum nanoparticles dynamically change over the reaction temperature, which also alters the electronic state of Pt nanoparticles which influences the reactivity and selectivity. Also, it is worth noting that there is a difference in transition temperature between impregnation (at 200 °C) and ion exchange (at 300 °C). As shown in the SAXS results in Figure 2 and Figure 3, there are significant changes in particle size of Pt/SiO$_2$ catalysts prepared by Ion exchange over the temperatures 100 ~ 400 °C, which may correspond to the change in XANES feature in comparison with Pt/SiO$_2$ catalysts prepared by impregnation.

Figure 3. Variation of particle size of Pt/SiO$_2$ catalysts processed by (A) ion exchange and (B) impregnation method under supercritical condition with n-dodecane. The corresponding size distribution profiles of Pt/SiO$_2$ catalysts processed by (C) ion exchange and (D) impregnation method.

The catalytic performance of each catalyst was determined by using GC/MS analysis. The liquid products collected for each reaction temperature were identified and quasi-quantitatively determined by calculating the total ion chromatogram (TIC) area ratio. The resulting conversion yields were listed in Table 1. In the case of the catalysts prepared by ion exchange (IE), over 13 % of cracking was observed at

Table 1. Reaction conversion (%) and product selectivities of Pt/SiO$_2$ catalysts processed by ion exchange (IE) and impregnation (IWI) method under supercritical condition with n-dodecane.

Conversion (%)*	Temperature (°C)		
	400	500	600
Pt/SiO$_2$ (IE)	13.4	15.2	15.8
Pt/SiO$_2$ (IWI)	5.8	20.0	22.3

Selectivity (%)		Pt/SiO$_2$ (IE)			Pt/SiO$_2$ (IWI)		
	Temperature (°C)	400	500	600	400	500	600
	Paraffins	100	100	88	52	46	19
	Olefins	-**	-	2	24	42	78
	Aromatics	-	-	10	24	12	3

400 °C and showed slightly increased conversion yields as the temperature increased. A comparably low conversion yield was obtained with the Pt/SiO$_2$ (IWI) sample at 400 °C, however, cracking increased with increasing conversion with ca. 22 % of yields at 600 °C, showing the higher yield compared to that of Pt/SiO$_2$(IE) at a high temperature. Overall, the cracking of n-dodecane shows the relatively high yields obtained by employing the Pt/SiO$_2$(IE) catalysts at 400 °C, while the impregnation method is favorable at high temperatures (>500 °C). It was reported previously that the reactivity of supported Pt catalysts is strongly dependent on the size of Pt particles under an atmospheric pressure.[5] The current findings under realistic conditions, however, are not in agreement with the particle size effects previously observed. For example, the higher conversion rate was obtained by Pt/SiO$_2$(IE) at 400 °C, with larger Pt catalysts compared to that of Pt/SiO$_2$(IWI). Rather, the morphology and the electronic state changes of Pt catalysts, as shown in Figure 4, might be critical to the catalytic reactivity.[6] The effect of properties of catalysts on the reaction product distribution was determined by calculating the product selectivity. In liquid products of n-dodecane decomposition, alkanes, alkenes and aromatic compounds were detected as shown in Figure 5. The selectivity was calculated by the relative amount (%) of liquid products, which was categorized with paraffin, olefin and aromatic compounds as a precursor of coke. Primary products with Pt/SiO$_2$(IE) are paraffins with relatively small amount of olefins and aromatic compounds. In the case of Pt/SiO$_2$(IWI), olefins are dominant at a high temperature while paraffins are favorable products at 400 °C. Since it is known that the reaction of olefins on Pt is faster than that of paraffins,[7] the resulting selectivity differences might suggest (1) the effect of morphology of catalysts or (2) the presence of additional hydrogenation reaction, but further studies will be needed to address this issue. Overall, the presented results provide a remarkable contribution toward the dynamic changes of nanoscale catalysts in realistic reaction environment, and could provide a unique practical insight into the better design of catalysts.
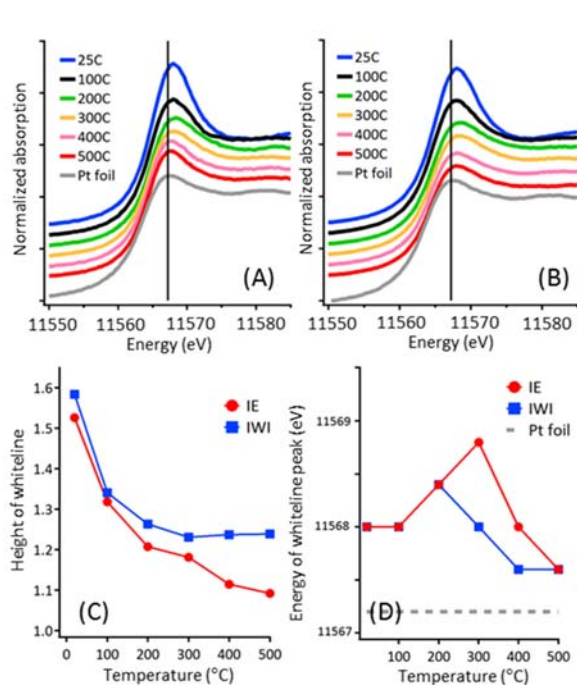

Figure 4. *in-situ* XANES(Pt L3) data of Pt/SiO$_2$ catalysts prepared by (A) ion exchange and (B) impregnation method under given reaction conditions with n-dodecane (C) height of whiteline and (D) the peak position of whiteline change over the range of temperatures
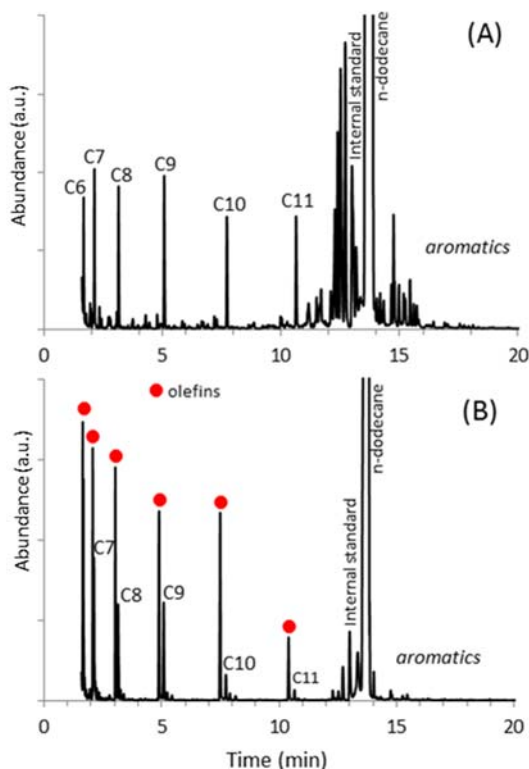
Figure 5. Representative GC-MS total ion chromatograms of collected liquid products of Pt/SiO$_2$ catalysts processed by (A) ion exchange and (B) impregnation method at 600 °C with n-dodecane under supercritical condition. C6-C11 indicate linear saturated hydrocarbons.

Operando characterization of catalytic cracking of n-dodecane over Pt-Sn bimetallic catalysts under supercritical condition; effect of Sn:

The objective of this project is to study the effect of Sn loading amount on Pt-Sn/SiO$_2$ bimetallic catalysts for the catalytic cracking of hydrocarbon fuels under supercritical condition. The properties of Pt-Sn catalysts and the catalytic performance was characterized by synchrotron-based small angle X-ray scattering (SAXS) and X-ray Absorption Near Edge Structure (XANES). As a model fuel, n-dodecane was chosen since it has been often used one of major components of petroleum-derived jet fuels. The cracking n-dodecane as an endothermic hydrocarbon fuel in flow cell reactor was carried out under supercritical condition. GC/MSD (Gas chromatography–mass spectrometry detector) was used to analyze the cracking products (liquid) collected at various status of the reaction. Catalytic performance and reaction selectivity were determined by analyzing the product distribution quantitatively. Raman spectroscopy was employed to analyze the spent catalysts with the focus on coke precursor species. SAXS scattering intensities of four different Pt-Sn/SiO$_2$ bimetallic catalysts in the temperature range of 25 – 600 °C at 750 psi with n-dodecane. The corresponding particle size (mean diameter, Å) and the size distribution profiles are illustrated in Figure 6. Without Sn (Pt$_1$Sn$_0$, Figure 6(A)), the particle size was 11.9± 0.9 Å at 25 °C but increased up to ca. 23.5±0.7 Å when reaction temperature reached over the critical condition (T$_c$=385 °C). However, the addition of Sn to Pt supported catalysts shows the significant
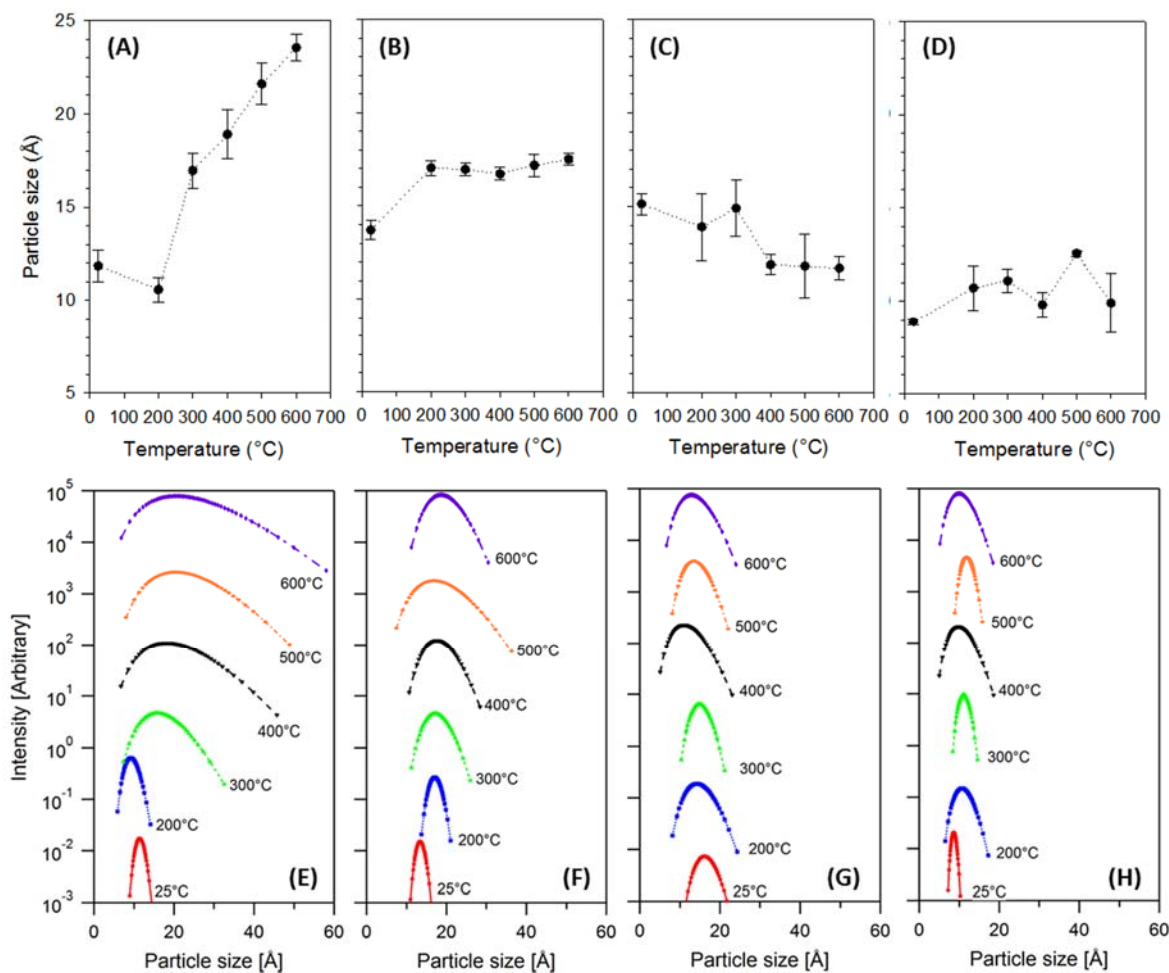

Figure 6. Particle mean diameter (A) –(D) and distribution (E)- (H)of Pt-Sn/SiO$_2$ catalysts in the temperature range of 25-600 °C at 750 psi with n-dodecane. (A),(E) Pt$_1$Sn$_0$; (B),(F) Pt$_3$Sn$_1$; (C),(G) Pt$_1$Sn$_1$; (D),(H) Pt$_1$Sn$_3$.

effect on their stability over the cracking process. The initial particle diameters (at 25 °C) of Pt_3Sn_1, Pt_1Sn_1, and Pt_1Sn_3 catalyst were 13.7±0.5, 15.1±0.6, and 8.9±0.2 Å, respectively. The particle size of each catalysts, after the temperature reached over the supercritical condition (at 600 °C), were merely changed to 17.5±0.3, 11.7±0.6, and 9.9±1.6 Å, respectively. There was the sudden increase on particle size of Pt_1Sn_3 catalyst when the reaction condition reaches at supercritical regime, over 500 °C. Overall, the size and the variation upon temperature increase were tent to be decreased as the amount of Sn was increased, clearly showing the increased stability under supercritical condition. The size distribution profiles in Figure 6 (E-H) emphasize the effect of Sn on the Pt catalyst. Without Sn promotion, the size distribution of monometallic Pt_1Sn_0 catalyst has dramatically increased as temperature increased, as shown in Figure 6(E). The addition of Sn increases its stability, showing that the variation on size distribution of Pt_1Sn_3, the highest amount of Sn among the prepared catalyst, are clearly reduced as temperature increases, as compared to those of Pt_1Sn_0 catalyst. For the better understanding of the

**Figure 7.** XANES spectrum of Pt-Sn/SiO_2 catalysts (Pt-L_3 edge)

interplay between morphology and catalytic reaction under supercritical environment, in situ XANES characterization has also exploited to measure the electronic states above the Fermi level localized on Pt element. The influence of the Pt-Sn local environment on catalytic performance was carried out by in-situ XANES characterization. Data shows that oxidation state of Pt nano particles at given temperature in a presence of n-dodecane is highly affective to the presence of Sn showed in Figure 7. Initially, Pt deposited at all support types is partially oxidized. The degree of oxidation and final electronic state are strongly related with amount of Sn added in the catalysts, which indicates the electronic state of Pt can be controlled by addition of Sn. While the ability to control the features of the bimetallic catalysts has been exploited to extensive studies, the structural and compositional changes under endothermic reaction condition are still a subject of debate. Zhu and coworkers have reported that the preparation method affects the distributions of Pt-Sn particle size and location, which can influence the stability and the resulting performance of catalysts.[8] The effect of Sn loading on the dehydrogenation of alkane has revealed the increased stability and olefin selectivity due to the increased Pt metal dispersion with Sn.9 However, to our best knowledge, many works has been focused on the basic electronic or structural properties of catalysts, while none of the studies address the characteristics of Pt-Sn catalysts under realistic reaction condition. Therefore, in a practical point of view, our finding is the first attempt to provide the physical properties of Pt-Sn bimetallic catalysts in the realistic environment.

The catalytic performance of each prepared catalysts was determined by quantitatively analyzing the cracking products by means of GC-MSD. In order to understand the cracking activity, the liquid products collected each reaction states were identified and determined by calculating the total ion chromatogram (TIC) area ratio. Figure 8 shows n-dodecane conversion yield (%) with respect to the cracking temperature on Pt-Sn bimetallic catalysts with different Sn amount. The monometallic Pt_1Sn_0 catalyst showed the increased conversion as temperature increases, while the comparably low conversion yield (ca. 22 %) has been determined during the supercritical condition. In bimetallic catalysts, the initial conversions (at 200 °C) of Pt_3Sn_1, Pt_1Sn_1, and Pt_1Sn_3 are 4.9, 7.8, and 2.0 %, respectively. The conversion
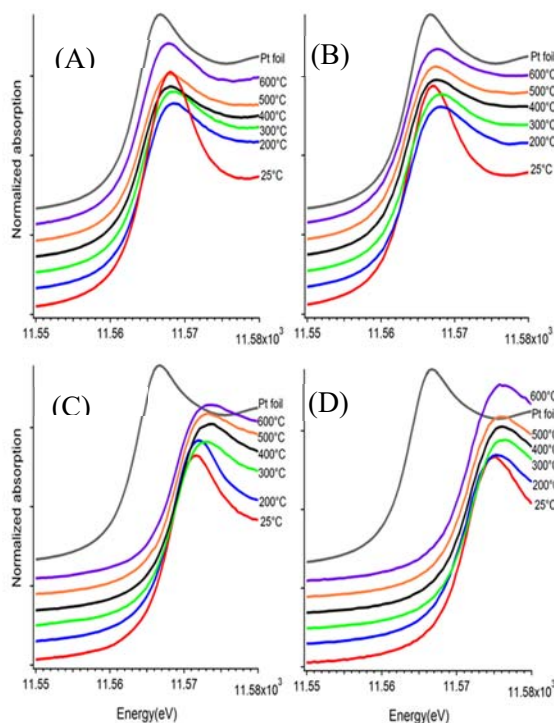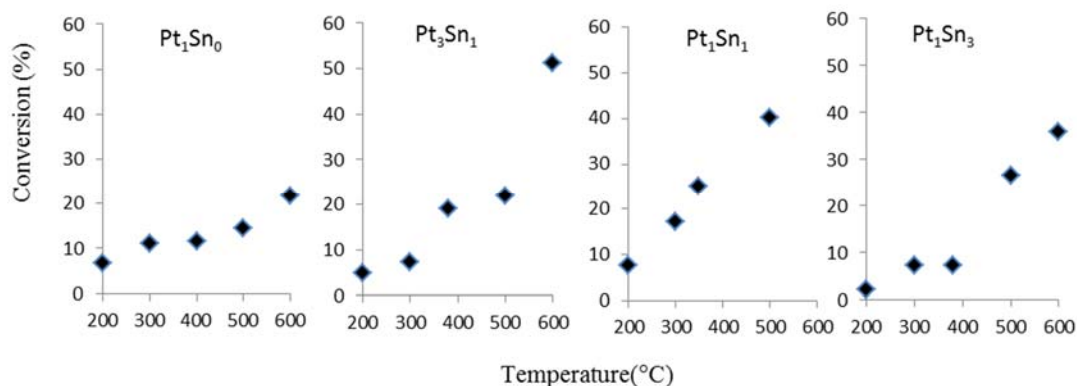
Figure 8. the conversion (%) of n-dodecane with Pt-Sn/SiO$_2$ catalysts

yields at supercritical status (at 500 – 600 °C), were dramatically increased to 51.2, 40.1 and 35.9 %, respectively. It is clear that the adding Sn promotes the cracking reaction of n-dodecane. Pt$_3$Sn$_1$ catalyst showed the highest conversion yield while the least among the prepared catalysts was Pt$_1$Sn$_3$ as 35.9 % which is well agreed with the recent findings with propane catalytic dehydrogenation.[9]

The selectivity of cracking reaction was also determined by means of the relative yields of paraffin, olefin, and aromatic compounds in liquid products collected at the supercritical status. In Figure 9, the olefin compounds were dominant with monometallic Pt$_1$Sn$_0$ catalyst, indicating the high olefin selectivity. In bimetallic catalysts, the high aromatic selectivity was observed as increased Sn amount. The high olefin selectivity was shown with Pt$_3$Sn$_1$, the least amount Sn catalyst, in Fig. 9(b). However, with increased Sn amount, the aromatic selectivity tends to be increased in Pt$_1$Sn$_1$ and Pt$_1$Sn$_3$ catalysts, as shown in Fig. 9(c-d). It is known that Sn could reduce the coke formation due to the modification of electronic nature of Pt atom.[10] Therefore, our finding suggests the amount of Sn should be optimized as well as the reaction temperature to prevent the formation of coke precursors but further studies on the coke formation such as Total organic carbon (TOC) analysis of coke will be needed to address this issue.
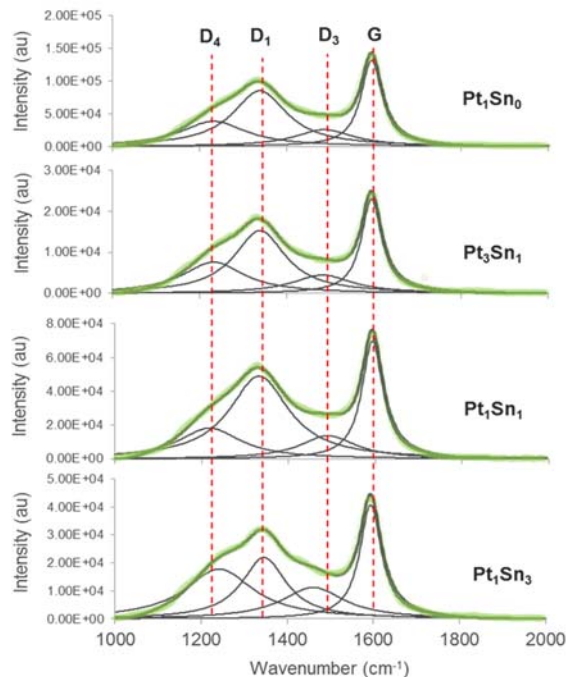
Major drawback of catalytic cracking is the deactivation of metal catalysts which is mainly caused by the build-up of carbonaceous deposits, or coke.[11] To get more precise insight of this phenomenon, Raman spectroscopy was employed to analyze the coke formed over the spent catalysts used this study.[12] Figure 10 shows the Raman spectra of coke formed over the spent Pt-Sn bimetallic
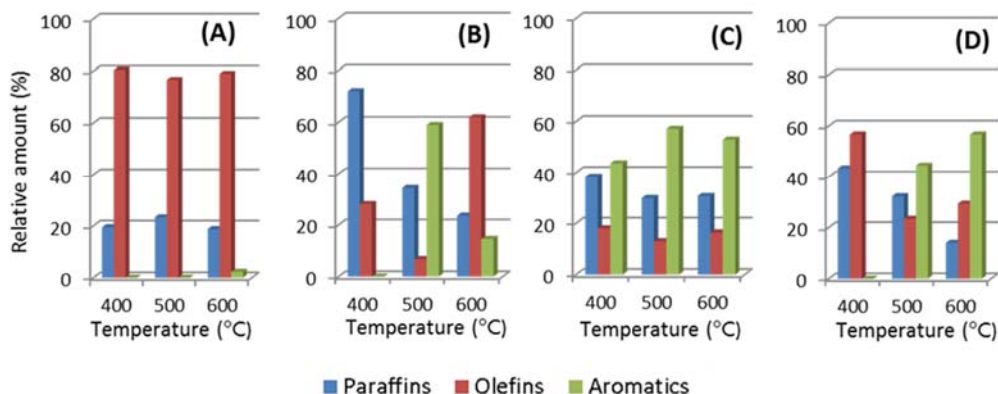
Figure 9. Catalytic selectivity of Pt-Sn/SiO$_2$ catalysts in the temperature range of 25 – 700 °C at 750 psi with n-dodecane; (A) Pt$_1$Sn$_0$ (B) Pt$_3$Sn$_1$ (C) Pt$_1$Sn$_1$ (D) Pt$_1$Sn$_3$

catalysts (green circles). In bimetallic Pt-Sn catalysts, two distinguishable Raman bands were characterized at around 1340 and 1595 cm^{-1}, identified as ring stretches of disordered (D_1 band) and ordered graphite lattice (G band), respectively.[10] The G band at 1595 cm^{-1} indicates the small graphitic crystallites formation since the perfect graphite crystals are measured at 1575 cm^{-1}. It is well known that in Raman spectra there are 4-5 bands are overlapped in carbonaceous materials. Finally, the deconvoluted Raman spectra of spent catalysts shows a combination of four fitted Raman bands shown in Figure 10. The additional two bands, D_3 (ca. 1500 cm^{-1}) and D_4 (ca. 1200 cm^{-1}) are correspond to amorphous carbon and disordered graphitic lattice (A_{1g} symmetry), respectively. There are no significant shifts observed in the position of G band, while D_1 bands shift upon the increased Sn amount. The reason of the apparent shift of the D_1 Raman band is currently under investigation. The intensity ratios D-to-G were also calculated and listed in Table 2. The relative intensity of D_1/G was observed to drop when the amount of Sn

Figure 10. Deconvoluted Raman spectra of spent Pt-Sn/SiO$_2$ catalysts

increases, while D_3/G and D_4/G intensity ratios showed the opposite trend. The previous studies have showed that the decreasing ID_1/IG value indicated the increasing degree of graphitization.[10] In our study, the increased amount of Sn may interfere the formation of disordered graphite lattice (i.e., graphene edges), thus shows the increased graphitization of carbonaceous materials over the catalyst surface.

In this work, the Pt-Sn/SiO$_2$ catalysts with different ratio of Pt and Sn were synthesized by simultaneous impregnation of Pt and Sn precursors. The influences of different Pt and Sn ratio on the catalyst structure and catalytic performance have been investigated. The high catalytic activity for the n-dodecane cracking has been achieved on Pt$_3$Sn$_1$/SiO$_2$ with n-dodecane conversion 51%. In the Pt-Sn/SiO$_2$ catalyst, the stability of Pt NPs increases with the increasing of Sn loading, which influences the catalytic performance for catalytic cracking at high temperature. The Pt species show more oxidative state with Sn addition. This change is unfavorable for the catalytic performance. Therefore, the catalytic performance for n-dodecane cracking shows no improvement when the loading amount of Pt beyond 50 %. The loading of Pt and Sn with an appropriate amount is important for balancing the stability of catalyst and the catalytic performance

Table 2. Raman band positions and band intensity ratios of Pt-Sn/SiO$_2$ catalysts

Catalysts	Sn amount (%)	G band (cm^{-1})	D1 band (cm^{-1})	I_{D1}/I_G	I_{D3}/I_G	I_{D4}/I_G
Pt$_1$Sn$_0$	0	1594	1338	0.64	0.19	0.29
Pt$_3$Sn$_1$	25	1595	1339	0.67	0.19	0.33
Pt$_1$Sn$_1$	50	1593	1333	0.70	0.20	0.26
Pt$_1$Sn$_3$	75	1593	1346	0.54	0.28	0.44

Archival publications, in print, in press, and submitted.

1. Effect of Particle Size Upon Pt/SiO$_2$ Catalytic Cracking of n-Dodecane Under Supercritical Conditions: in situ SAXS and XANES Studies, Chem.Cat.Chem. Comm., 2016, in revision.
2. Inherent Size Effects on XANES of Nanometer Metal Clusters: Size-Selected Platinum Clusters on Silica, J. Am. Chem. Soc., submitted
3. Operando characterization of catalytic cracking of n-dodecane over Pt-Sn bimetallic catalysts under supercritical condition; effect of Sn, in preparation.
4. In-situ/operando SAXS and ASAXS characterization upon Pt/Al$_2$O$_3$ catalytic cracking of n-Dodecane at supercritical condition; the influence of Mg, in preparation.

People supported by the grant.
Sungwon Lee
Kamila Wiaderek
Discoveries, inventions, and patent disclosures

References
(1) Jacobs, G.; Alvarez, W. E.; Resasco, D. E. *Applied Catalysis A: General* **2001**, *206*, 267.
(2) Xian, X.; Liu, G.; Zhang, X.; Wang, L.; Mi, Z. *Chemical Engineering Science* **2010**, *65*, 5588.
(3) Behafarid, F.; Ono, L. K.; Mostafa, S.; Croy, J. R.; Shafai, G.; Hong, S.; Rahman, T. S.; Bare, S. R.; Roldan Cuenya, B. *Physical Chemistry Chemical Physics* **2012**, *14*, 11766.
(4) Ankudinov, A. L.; Rehr, J. J.; Low, J. J.; Bare, S. R. *The Journal of Chemical Physics* **2002**, *116*, 1911.
(5) Santhosh Kumar, M.; Chen, D.; Walmsley, J. C.; Holmen, A. *Catal. Commun.* **2008**, *9*, 747.
(6) Balint, I.; Miyazaki, A.; Aika, K.-i. *Chem. Commun.* **2002**, 1044.
(7) Cortright, R. D.; Bergene, E.; Levin, P.; Natal-Santiago, M.; Dumesic, J. A. In *Studies in Surface Science and Catalysis*; Joe W. Hightower, W. N. D. E. I., Alexis, T. B., Eds.; Elsevier: 1996; Vol. Volume 101, p 1185.
(8) Zhu, H.; Anjum, D. H.; Wang, Q.; Abou-Hamad, E.; Emsley, L.; Dong, H.; Laveille, P.; Li, L.; Samal, A. K.; Basset, J.-M. *Journal of Catalysis* **2014**, *320*, 52.
(9) Lee, M.-H.; Nagaraja, B. M.; Lee, K. Y.; Jung, K.-D. *Catalysis Today* **2014**, *232*, 53.
(10) Sattler, J. J. H. B.; Beale, A. M.; Weckhuysen, B. M. *Physical Chemistry Chemical Physics* **2013**, *15*, 12095.
(11) McGregor, J.; Huang, Z.; Parrott, E. P. J.; Zeitler, J. A.; Nguyen, K. L.; Rawson, J. M.; Carley, A.; Hansen, T. W.; Tessonnier, J.-P.; Su, D. S.; Teschner, D.; Vass, E. M.; Knop-Gericke, A.; Schlögl, R.; Gladden, L. F. *Journal of Catalysis* **2010**, *269*, 329.
(12) Han, Z.; Li, S.; Jiang, F.; Wang, T.; Ma, X.; Gong, J. *Nanoscale* **2014**, *6*, 10000.

PI Name: Richard N. Zare

Address: Department of Chemistry, Stanford University, 333 Campus Drive, Stanford, CA 94305-4401

Statement of objectives: Development of ambient ionization techniques to study catalyst and fuel interactions for the purpose of achieving endothermic cooling.

Methodology developed: Nanotip ambient ionization mass spectrometry and desorption ionization mass spectrometry for electrochemical reactions.

Accomplishments:

1. **Monitoring Catalytic Processes on Electrode Surfaces in Real-Time**

Past efforts have been placed on the development and implementation of a new desorption electrospray ionization (DESI) based electrochemistry (EC) coupled mass spectrometry (MS) ionization method for in situ monitoring of electrochemical reactions. These efforts led to the "waterwheel" electrode (see Figure 1) where a platinum metal was placed around a Teflon disc, which was affixed to a stainless steel shaft. This disc is rotated by a stepper motor. A counter electrode and reference electrode are immersed in a reservoir containing electrolyte solution. The platinum ring is dipped in the electrolyte solution and the ring is contacted with a piece of copper, allowing for a completed three-electrode circuit. A DESI source is then directed at the platinum ring working electrode where the spray contains the analyte of interest. A potential is applied to the platinum working electrode to study the electrochemical process
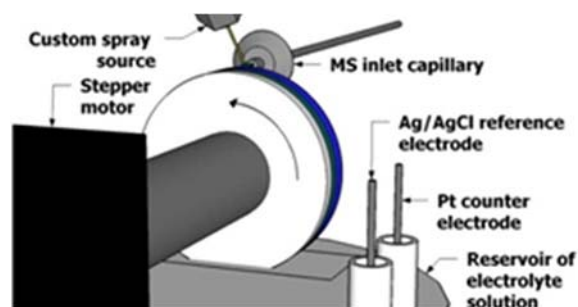

Figure 1. The waterwheel electrode setup used for DESI- ECMS analysis.

in question. Systems that have been studied and published in peer-reviewed journals by way of funding from the AFOSR include the electrooxidation of xanthine to uric acid,[1] the electrooxidation of N,N-dimethylaniline (DMA),[2] and the two-electron oxidation of two secondary amines to form nitrenium ions.[3] The studies involving DMA were particularly helpful in elucidating the half-life times of the transient species in solution. This fleeting intermediate was analyzed by DESI-ECMS during the electrochemical oxidation of DMA to the DMA radical cation. A very large second-order rate constant for the dimerization of the DMA radical cation, measured by the Bard lab using SECM[4] infers that the electrogenerated DMA radical cation in solution is short-lived. The second-order kinetics also implies that the reaction is concentration dependent such that the half-life time of the DMA radical cation in solution is smaller at higher concentrations. To this end we set out to determine the shortest half-life time of the DMA radical cation that the waterwheel was able to observe within the operating procedures for the LTQ Orbitrap XL hybrid mass spectrometer. Data clearly show that DESI-ECMS is capable of observing the transient electrochemically generated DMA radical cation intermediate (see Figure 2) with half-life times on the order of microseconds (see Table 1), 4-5 orders of magnitude faster than for previously reported electrochemical mass spectrometric techniques. We believe this to be a very powerful technique that can strengthen our understanding of many different systems.
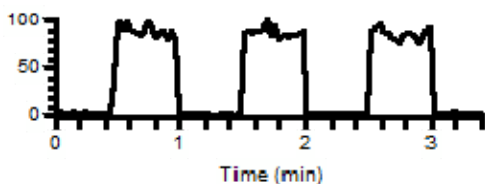
Figure 2. The extracted ion chromatogram for the DMA radical cation as a function of when the oxidation potential was applied to the working electrode.

DMA concentration in spray (mM)	Calculated half-life time (μs)
0.024	170
0.047	85
0.094	42
0.24	17
4.7	0.85

Table 1. The initial concentrations of DMA and the calculated half-life times in solution of the DMA radical cation, assuming full conversion.

References:

(1)   Brown, T. A.; Chen, H.; Zare, R. N. J. Am. Chem. Soc. 2015, 137 (23), 7274.
(2)   Brown, T. A.; Chen, H.; Zare, R. N. Angew. Chem. Int. Ed. 2015, 54 (38), 11183.
(3)   Brown, T. A.; Hosseini-Nassab, N.; Chen, H.; Zare, R. N. Chem. Sci. 2015, 7 (1), 329.
(4)   Cao, F.; Kim, J.; Bard, A. J. J. Am. Chem. Soc. 2014, 136 (52), 18163.

2. Nanotip Ambient Ionization Mass Spectrometry (NAIMS)

Previous efforts were made in collaboration with Dr. Steve Chambreau of AFRL to study the activation of the ionic liquid 2hydroxyethylhydrazinium nitrate (HEHN) at the surface of S-405 granules at elevated temperatures using DESI-MS to draw correlations between our observations and data acquired from the Advanced Light Source (ALS) at the Lawrence Berkeley National Lab. With DESI being a relatively soft ionization technique, we determined that a new ionization technique was needed to analyze HEHN to better compare with the data from ALS. To that end, we applied NAIMS to the system in question.[5] NAIMS is a harder ionization technique where a tungsten nanotip is held at a high potential that is held close over the conducting sample of interest. The high potential difference held at the narrow tip induces a localized plasma over the sample, which then desorbs and ionizes the sample. The result is

ions that are drawn into the mass spectrometer for analysis. See Fig. 3.
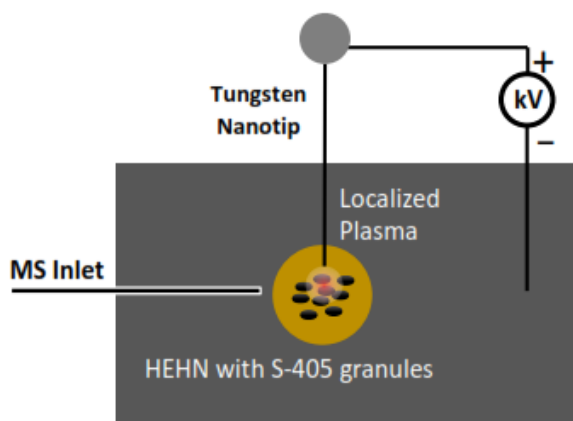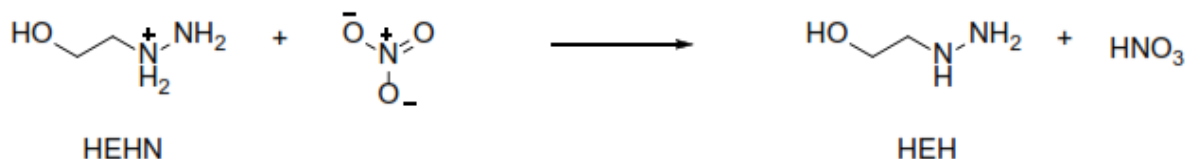

Figure 3. Schematic of the NAIMS experimental setup analyzing HEHN reacting on S-405 granules.

The proposed thermal decomposition of HEHN is the deprotonation of the ionic liquid to form hydroxyethylhydrazine (HEH, Scheme 1). However, the catalytic decomposition of HEHN is not well

Scheme 1: Thermal decomposition of HEHN to HEH.

understood. The products formed from high temperature catalyst surface indicate recombination reactions forming higher masses than the ionic liquid precursor (Figure 4). This trend led to a proposed mechanism in which the HEHN can dimerize with subsequent rearrangements to form various heterocycles (Scheme 2). Studies are ongoing utilizing this new ionization technique to elucidate the catalytic role of the S-405 in the degradation of HEHN at elevated temperatures.
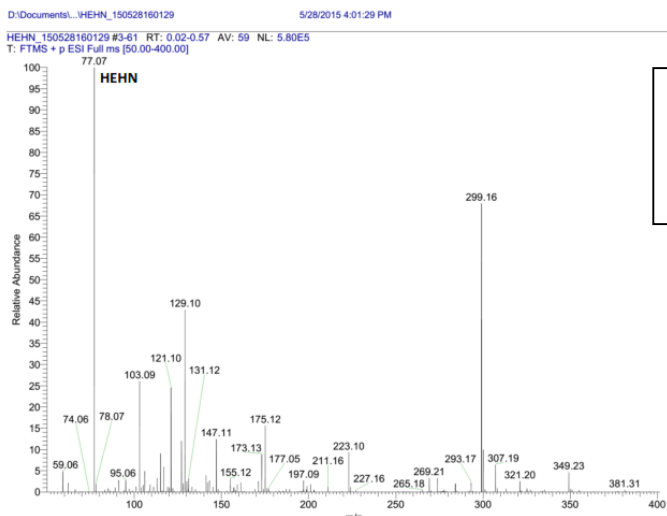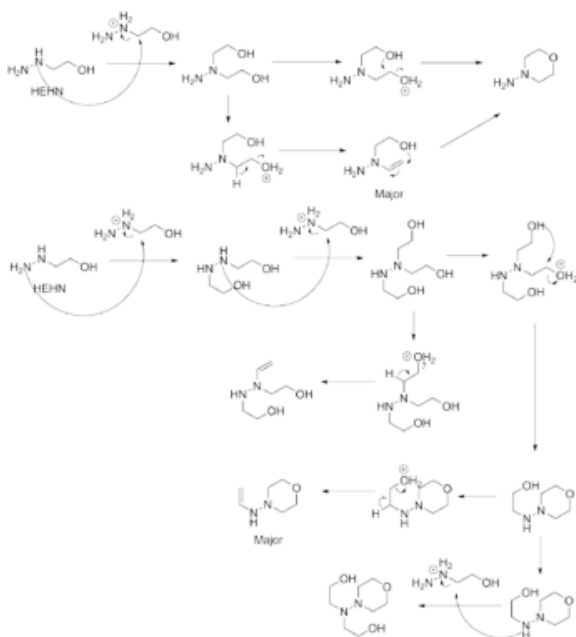

Figure 4. High temperature NAIMS analysis of HEHN on S-405 granules using an LTQ Orbitrap XL mass spectrometer.

Scheme 2. Proposed high temperature recombination pathways of HEHN on S-405 granules based upon NAIMS experiments.

References:

(5) Zhenpeng Zhou, Jae Kyoo Lee, Samuel C. Kim, and Richard N. Zare, "Nanotip Ambient Ionization Mass Spectrometry," *Anal. Chem*. **88**, 5542-5548 (2016).

3. **Study of Chemical Reactions in Droplets**

Because this sub-contract permitted us to acquire a high-resolution mass spectrometer, this instrumentation permitted many studies on reactions in microdroplets. What follows is a listing of other publications supported by this sub-contract:

(6) Jae Kyoo Lee, Samuel Kim, Hong Gil Nam, and Richard N. Zare "Microdroplet fusion mass spectrometry for fast reaction kinetics" Proc. Natl. Acad. Sci. (USA) 112, 3898–3903 (2015).

(7) Cornelia L. Boeser, Jeffrey C. Holder, Buck L. H. Taylor, K. N. Houk, Brian M. Stoltz and Richard N. Zare, "Mechanistic Analysis of an Asymmetric Palladium- Catalyzed Conjugate Addition of Arylboronic Acids to ß- substituted Cyclic Enones," Chem. Sci. 6, 1917–1922 (2015).

(8) Jie Jiang, Hong Zhang, Ming Li, Maria T. Dulay, Andrew J. Ingram, Na Li, Hong You, Richard N. Zare, "Droplet Spray Ionization from a Glass Microscope Slide: Real-Time Monitoring of Ethylene Polymerization, " Anal. Chem. 87, 8057–8062 (2015).

(9) S. Banerjee and R. N. Zare, "Syntheses of Isoquinoline and Quinoline in Charged Microdroplets," Angew. Chem. Int. Ed. 54, 14795 –14799 (2015).

(10) Andrew J. Ingram, Cornelia Boeser, and Richard N. Zare, "Going Beyond Electrospray: Mass Spectrometric Studies of Chemical Reactions in and on Liquids," Chem. Sci. 7, 39-55 (2016).

(11) Andrew J. Ingram, Katherine L. Walker, Richard N. Zare, and Robert M. Waymouth , "Catalytic Role of Multinuclear Palladium-Oxygen Intermediates in Aerobic Oxidation Followed by Hydrogen Peroxide Disproportionation," J. Am. Chem. Soc.137, 13632 – 13656 (2015).

(12) Ryan Baxter, Yong Liang, Xin Hong, Timothy A. Brown, Richard N. Zare, K. N. Houk, Phil S. Baran, and Donna G. Blackmond, "Mechanistic Insights into Two- Phase Radical C- H Arylations," ACS Central Science 1, 456-462 (2015).

(13) J. Brannon Gary, Cooper Citek, Timothy A. Brown, Richard N. Zare, Erik C. Wasinger, and T. Daniel P. Stack, "Direct Copper(III) Formation from O2 and Copper(I) with Histamine Ligation, J. Am. Chem. Soc. (in press).

Figure 2. Droplet chemistry. The upper panel shows the setup for
fused droplets; the lower panel shows the setup for electrospray ionization .

Andrew J. Ingram, Katherine L. Walker, Richard N. Zare, and Robert M. Waymouth, "Catalytic Role of Multinuclear Palladium-Oxygen Intermediates in Aerobic Oxidation Followed by Hydrogen Peroxide Disproportionation," J. Am. Chem. Soc.137, 13632 – 13656 (2015).

Andrew J. Ingram, Cornelia Boeser, and Richard N. Zare, "Going Beyond Electrospray: Mass Spectrometric Studies of Chemical Reactions in and On Liquids," Chem. Sci. 7, 39–55 (2016).

The last article is a review that shows how droplet chemistry might be applied to learn about organic and inorganic reactions in general. The most exciting results of the other articles have been (1) the identification of previously unobserved intermediates and (2) the significant acceleration by factors of one thousand or more (!) of chemical reactions in droplets. Future work is planned to continue these droplet chemistry studies.

Archival publications, in print, in press, and submitted.

Please see the references above. All but reference (4) was supported by this sub-contract.

People supported by the grant.

Richard N. Zare
Sam Kim
Qinghao Wu
Tim Brown

Discoveries, inventions, and patent disclosures.

None.

1.

Report Type

Final Report

Primary Contact Email
Contact email if there is a problem with the report.

anderson@chem.utah.edu

Primary Contact Phone Number
Contact phone number if there is a problem with the report

8015857289

Organization / Institution name

University of Utah

Grant/Contract Title
The full title of the funded effort.

Catalyst and Fuel Interactions to Optimize Endothermic Cooling

Grant/Contract Number
AFOSR assigned control number. It must begin with "FA9550" or "F49620" or "FA2386".

FA9550-12-1-0481

Principal Investigator Name
The full name of the principal investigator on the grant or contract.

Scott Anderson

Program Officer
The AFOSR Program Officer currently assigned to the award

Michael R. Berman

Reporting Period Start Date

09/30/2012

Reporting Period End Date

05/31/2016

Abstract

This report summarizes the main findings of an AFOSR Basic Research Initiative project in the area of endothermic fuels catalysis. The focus was on developing improved catalysts to enhance and control endothermic fuel reactions, to enhance cooling capacity for aircraft. In addition there was substantial basic mechanistic work, aimed at understanding processes responsible for catalytic activity for the reactions of interest, and for deactivation and coking of the catalysts. Finally, there was significant methods development in the areas of theory, catalyst synthesis and characterization, and methods for catalytic reaction analysis.

Distribution Statement
This is block 12 on the SF298 form.

Distribution A - Approved for Public Release

Explanation for Distribution Statement
If this is not approved for public release, please provide a short explanation. E.g., contains proprietary information.

SF298 Form

DISTRIBUTION A: Distribution approved for public release.

Please attach your **SF298** form. A blank SF298 can be found **here**. Please do not password protect or secure the PDF The maximum file size for an SF298 is 50MB.

sf0298.pdf

Upload the Report Document. File must be a PDF. Please do not password protect or secure the PDF . The maximum file size for the Report Document is 50MB.

Final report with SF298 cover page.pdf

Upload a Report Document, if any. The maximum file size for the Report Document is 50MB.

Archival Publications (published) during reporting period:

51 total - see lists at end of each report chapter

New discoveries, inventions, or patent disclosures:

Do you have any discoveries, inventions, or patent disclosures to report for this period?

Yes

Please describe and include any notable dates

Patent issued, April 26 2016

Do you plan to pursue a claim for personal or organizational intellectual property?

No

Changes in research objectives (if any):

None

Change in AFOSR Program Officer, if any:

None

Extensions granted or milestones slipped, if any:

6 month no-cost extension granted to allow work to be brought to a conclusion

AFOSR LRIR Number

LRIR Title

Reporting Period

Laboratory Task Manager

Program Officer

Research Objectives

Technical Summary

Funding Summary by Cost Category (by FY, $K)

	Starting FY	FY+1	FY+2
Salary			
Equipment/Facilities			
Supplies			
Total			

Report Document

Report Document - Text Analysis

Report Document - Text Analysis

Appendix Documents

2. Thank You

E-mail user

Aug 30, 2016 20:08:47 Success: Email Sent to: anderson@chem.utah.edu